2010-01-08

Thermal Robotic Arm Controlled Spraying via Robotic Arm and Vision System

Dermot Breen

Technological University Dublin

Recommended Citation

Breen, D. (2010) *Thermal Robotic Arm Controlled Spraying via Robotic Arm and Vision System.* Doctoral Thesis. Technological University Dublin. doi:10.21427/D7N605

Thermal Robotic Arm Controlled Spraying via Robotic Arm and Vision System

by

Dermot Breen

School of Electrical Engineering Systems

Dublin Institute of Technology

Ireland.

A Thesis submitted for the Degree of Doctor of Philosophy

Supervised by Dr. David Kennedy and Professor Eugene Coyle

8th January 2010

Abstract

The Tribology Surface Engineering industry is a worldwide multi billion euro industry with significant health and safety risks. The thermal spraying sector of this industry employs the technique of applying molten surface coating material to a substrate via a thermal spray process which is implemented either by manual spraying or pre-programmed robotic systems. The development of autonomous robotic systems for thermal spraying surface coating would significantly improve production and profitability over pre-programmed systems and improve health and safety over manual spraying. The aim of this research was to investigate and develop through software simulation, physical modelling and testing the development of robotic subsystems that are required to provide autonomous robotic control for the thermal spraying process. Computer based modelling programs were developed to investigate the control strategy identified for the thermal spaying process. The algorithms included fifth order polynomial trajectories and the complete dynamic model where gravitational, inertia, centrifugal and coriolis torques are considered. Tests provide detail of the load torques that must be driven by the robot electric actuator for various structural changes to the thermal spraying robot and for variations in trajectory boundary conditions during thermal spraying. The non-linear and coupled forward and inverse kinematic equations of a five axis articulated robot with continuous rotation joints were developed and tested via computer based modelling and miniature physical robot modelling. Both the computer based modelling and physical model confirmed the closed form kinematic solutions. A solution to running cables through the continuous rotation joints for power and data is present which uses polytetrafloraethylene (PTFE) electroless nickel. This material was identified during the literature review of surface coating materials. It has excellent wear, friction and conductivity properties. Physical tests on a slip ring and brushes test rig using electroless nickel are presented which confirm the viability of using PTFE electroless nickel as a slip ring. Measurement of the substrate during thermal spraying so as to autonomously control the thermal spaying robot is a significant challenge. This research presents solutions for the measurement of the substrate using a low cost camera system and lasers in a single wavelength environment. Tests were carried out which resulted in the removal of a butane flame obscuring a test piece requiring measurement from the camera image so that substrate measurements can be made using image processing and analysis techniques such as canny edge detection and centroid measurements. Test results for the low cost vision system provide depth measure errors of ±0.6 % and structural measurements such as area and perimeter in the range -5% to -7.5%. These results confirm the efficacy of this novel flame removal technique.

Declaration

I certify that this thesis which I now submit for examination for the award of Degree of Doctor of Philosophy, is entirely my own work and has not been taken from the work of others, save and to the extent that such work has been cited and acknowledged within the text of my work.

This thesis was prepared according to the regulations for postgraduate study by research of the Dublin Institute of Technology and has not been submitted in whole or in part for an award in any other Institute or University.

The work reported on in this thesis conforms to the principles and requirements of the Institutes guidelines for ethics in research.

The Institute has permission to keep, to lend or to copy this thesis in whole or in part, on the condition that any such use of the material of the thesis be duly acknowledged.

Signature________________________________ Date_________________
Candidate

Acknowledgements

I would like to thank my supervisors Dr. David Kennedy and Dr. Eugene Coyle for their help and support in this research. I wish to acknowledge thanks to my Head of Department Mr. Michael Farrell for his support. Finally but not least I would like to thank my wife Marie and children Tom and Margaret as without their support and encouragement this research would not be possible.

Table of Contents

List of Figures

List of Tables

CHAPTER 1

INTRODUCTION

1.1 Research Aims and Objectives

Thermal spraying of surface coatings relies on manual spraying and or automatic control robotic systems. The manual spraying approach has significant health and safety risks and quality may not be as high as an automatic control robotic system. An automatic robotic system however requires considerable preplanning and prior knowledge of the product being coated.

The aim of this research is to review the broad range of robotic sub-systems associated with thermal spraying robotics and following this review identify areas that could be developed and tested so as to move from an automatic control robotic system to an autonomous control robotic system. Autonomous in the sense that preplanning and pre-programming are significantly reduced.

Following identification of the areas for further development leads to a number of research objectives and they are

- Develop ideas and solutions in each of the areas identified for further development
- Develop and test mathematical models where necessary
- Develop and test simulation (program) models where necessary
- Develop and test physical models where necessary

1.2 Robot History and Market Size

Ctesibius of Alexandria (285 - 222 BC) can be considered to be the first inventor of a robot for two reasons. He invented musical organs and water clocks with movable figures (Shelton, 2003) and he carried out experiments and wrote the first treatises on compressed air (NationMaster, 2005). For this he is sometimes referred to as the father of pneumatics. This was many years before the term robot was used. The Czech playwright Karel Capek coined the term robot which is derived from the Slav robota meaning executive labour in his play Rossum’s Universal Robots in 1921 (Sciavicco, 2004). It was a further forty years in 1961 before the first industrial robot was installed on an automobile production line in New Jersey by General Motors. One of the first electrically powered and computer controlled robot arms called the Stanford arm was designed by Victor Scheinman in 1969 while working as a mechanical engineering student in the Stanford Artificial Intelligence Lab (Stanford, 2007). This robot arm was the precursor to modern industrial robotic systems.

The International Federation of Robotics produces statistics for robots worldwide. Table 1-1 is an extract from their executive summary detailing the existing and estimated operational stock of industrial robots for 2007, 2008 and 2011 (IFR, 2008).

Country	**2007**	**2008**	**2011**
America	165,328	176,500	204,200
Asia/Australia	498,786	512,600	589,900
Europe	328,568	345,200	389,300
Africa	1,323	1,600	2,800
Totals	994,005	1,035,900	1,185,900

Table 1-1 Industrial Robots Operational Stock

These figures are based on the assumption of a 12 year service life. The operational stock of industrial robots is somewhat surprising in that there are just over 1 million operational industrial robots worldwide, a relatively low number. This suggests there is significant scope for the development of low cost advanced robotic systems in a broad range of industries. Although the predominant user of industrial robots is the motor and automotive industry, there has been a 6% increase in the metal product industry. In 2007 the supply of advanced multipurpose robots shows a significant increase in the articulated robot manipulator which increased by 12 % to 66% of the installed base. All other types such as Cartesian, Cylindrical and SCARA were down.

1.3 Industrial Robot Manipulator Design

The Japanese Industrial Robot Association (JIRA), the Robotics Institute of America (RIA) and the Association Francaise de Robotique (AFR) all classify robots by robot complexity, however JIRA provide the widest range of classes, defining six in all. Class 6 of the JIRA classifications are intelligent robots i.e. robots that understand their environment and can react to unexpected changes in the environment (Niku, 2001). This research is on an autonomous thermal spraying robot manipulator placing it in class 6 of JIRA classifications.

The design of an autonomous robotic system which can be used for the control of a powder thermal spraying oxyacetylene torch tip in three dimensional space requires detailed consideration of a range of robot design issues listed in Table 1-2.

- Thermal spraying surface coating specification,
- the task and autonomous trajectory planning,
- the robot forward and inverse kinematics (non linear),
- the robot dynamics (non linear),
- the central control system technology and
- the sensor technology.

Table 1-2 Robot Design Issues

Robot design covers a very broad range of subjects and this was one of the key reasons for pursuing robotics research. The interconnection between the robot design issues listed are shown in Figure 1-1.

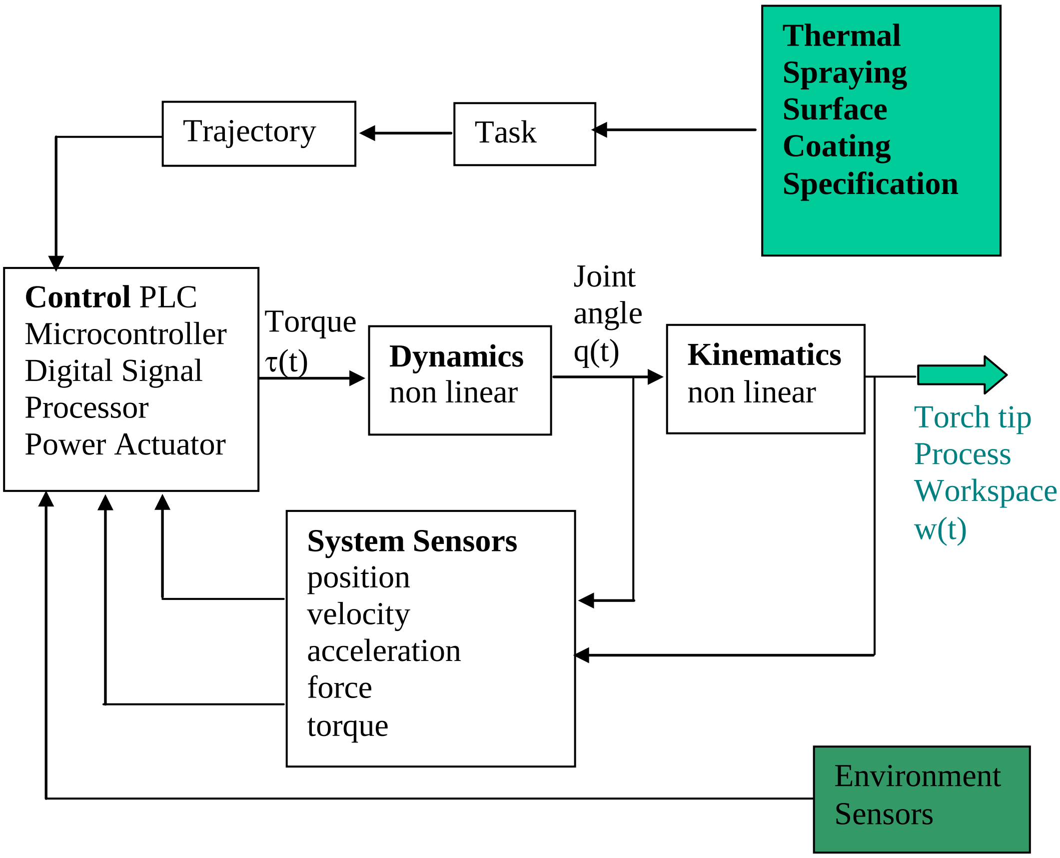

Figure 1-1 Robot Design Schematic

1.3.1 Thermal Spraying Surface Coating Specification

The thermal spraying surface coating specification details the thermal spraying requirements and therefore a particular project. This specification will be provided to a human operator to conduct the thermal spraying or will be used to pre-program a robotic system. The difficulty with pre programmed systems is that any changes however minor require reprogramming which can introduce significant delays and effect profitability. A human operator can sometimes be more efficient depending on the required changes. Developing an autonomous system which minimises pre programming and increases quality can increase production times and productivity.

1.3.2 Task and Autonomous Trajectory Planning

In an automatic system (pre programmed) the process specification is used to develop the robot manipulators task and trajectory planning. This is the movement of the torch tip in 3D space over specified periods of time thus conducting the appropriate thermal spraying. Trajectory planning is an important area of design as speed of spraying is directly related to the trajectory plan. Maximising speed to carry out appropriate spray levels are needed; however the robot manipulator must be able to produce the necessary velocities and accelerations to comply with efficient spray speeds. In an autonomous system, the requirement for this research, the trajectory plan must be generated in real-time during the thermal spraying process without any initial knowledge of the products shape or orientation. A minimal amount of pre-programming may be required such as spray heights and times for particular surface coating material.

1.3.3 Robot Forward and Inverse Kinematics (non linear)

The relationship between the torch tip in world coordinates is related to the robots actuator joints which may be either prismatic (linear) or revolute is provided via the robots forward and inverse kinematics equations. These equations are robot manipulator specific and highly non linear.

1.3.4 Robot Dynamics (non linear)

The movement of a robot manipulator in 3D via force and torque is modelled via the robots dynamic model which is also highly non linear. For a robot manipulator with revolute joints the load torques are; inertial, centrifugal, coriolis, gravitational and frictional. The robot actuators must provide the necessary torque to drive the robot load at the required velocities and acceleration.

1.3.5 Central Control System Technology

The central control system where the pre programmed or autonomous routines are run and fed to the actuator power may be Programmable Logic Controllers (PLC’s), Computers or for small systems microcontroller/digital signal controllers.

1.3.6 Sensor Technology

To develop an autonomous thermal spraying system which can react to changes in the product specification, a significant use of robot and environment sensor technology is required. The program routines are also more complex as the system must respond to changing sensor data and update the robot task and trajectory plan in a deterministic time frame.

1.4 Chapters

Chapter 2 deals with thermal spraying. Thermal spraying is the application of surface coatings via a thermal spray to a substrate to improve the substrates characteristics. The global market for thermal sprayed coatings is of considerable size. There are fundamentally four thermal spraying technologies, flame, arc, plasma and high velocity oxy-fuel spraying systems.

To design an autonomous thermal spraying robot manipulator it is necessary to understand the thermal spraying process. The fundamental objective of a thermal spraying robot arm is to move the torch tip a fixed distance across the substrate to be coated with the added requirement that the torch tip remains perpendicular to the substrate being sprayed and within a specified workspace. Figure 1-2 shows the thermal spray tip a fixed distance from the substrate surface and at right angles to the surface.

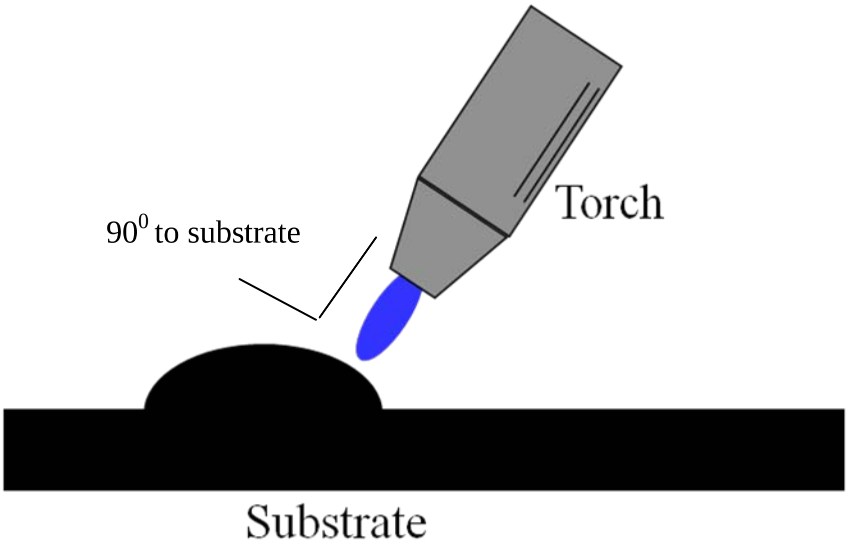

Figure 1-2 Torch Perpendicular to Curved Substrate

Chapter 3 Robot actuators, trajectory planning, and dynamics details the issues surrounding robot dynamics, the type of electric actuators available and trajectory planning for smooth operation.

To control the movement of a robot manipulator it is necessary to have details of the trajectory the robot must take for a particular application. The movement of the robot structure along a particular trajectory is achieved in a significant number of industrial applications via geared electric motor actuators. The sizing of such devices requires knowledge about the robots dynamics. The level of detail depends on the particular application and the velocities and accelerations necessary for a particular operation.

Chapter 4 Robot Kinematics details the kinematic solution for a manipulator with continuous rotation waist, shoulder and elbow revolute joints. This chapter also details a solution to delivering power and data across the continuous rotation joints.

The reason for this form of robot manipulator is that work space analysis suggests maximum workspace for a particular robotic structure can be achieved if there are no joint rotation limits i.e. if they can rotate a full $360^{0.}$ It was therefore decided to develop a closed form solution to the forward and inverse kinematics of a 5 axis articulated robot manipulator with continuous rotation joints for the waist, shoulder and elbow joints.

Chapter 5 Substrate orientation and measurement details techniques and test results that may be used for the control of a thermal spraying robot manipulator.

The location and measurement of the substrate to be sprayed and the location and orientation of the thermal spraying torch are important issues for the autonomous control of a thermal spraying robotic manipulator. There are many object and depth measurement techniques; however few operate in the difficult optical environment of high temperature thermal spraying. This is an important area for the development of autonomous control. If the robot manipulator can rely on sensor data which is generated in real-time and providing information about the product shape and location prior knowledge of the product becomes unnecessary. The robot control system can servo the thermal spraying torch to the correct orientation and distance from the product for coating.

Chapter 6 Thermal spraying vision system details a novel system and test results of optical filtering combined with image processing and analysis techniques. The most significant difficulty in automating the thermal spraying process with robotics is the interference with traditional sensors and in particular vision systems from the harsh thermal spraying optical environment. Most vision systems simply saturate when viewing a high temperature scene unless very expensive equipment is employed. This is another important area of development for autonomous thermal spraying control. Combining depth measurement and vision systems provide the bases for autonomous robot control of thermal spraying.

1.5 Publications

The majority of the research and work described in this thesis has been presented at peer reviewed conferences in the United Kingdom, Spain, Ireland and France. The papers are listed under Publications.

CHAPTER 2

THERMAL SPRAYING

2.1 Introduction

Thermal spraying is the application of surface coating material to various substrates via a thermal spray. Dr Max Schoop invented this technique in the early 1900’s when he projected molten material from a spray gun which used oxygen and acetylene as the heat source and compressed air as the propellant (Stokes, 2008).

The number of coating materials has grown substantially since the early 1900’s and it is the aerospace industry that has traditionally been the largest customer of thermal spray products. However the range of surface coating materials is expanding as are the industries using the technology. Other industries that routinely use this technology include power generation, petrochemical, automotive, marine, biomedical and electronics to provide improved wear resistance, corrosion resistance and thermal characteristics, to name just a few (Philip, et al., 1999).

Thermal spraying is an attractive surface coating technique due to the fact that it offers a wide and expanding choice of coating materials and processes that have a reduced impact on the environment in comparison to conventional surface coating techniques (Philip, et al., 1999). This reduced impact on the environment is due to a reduction of resources required and production of minimal noxious waste. There are however Health and Safety risks, which must be managed, associated with thermal spraying such as noise, heat, explosion and ultra violet light.

The Handbook of Thermal Spray Technology (Davis, 2005) lists 34 industrial sectors that rely on thermal spray processes and coatings. All but 9 rely on the oxy-fuel thermal spraying process, which is the technology of choice for this research. These industries use thermal spray coatings because they offer substrate improvements such as wear, corrosion and heat resistance.

The Surface Engineering Committee of the Institute of Materials 2000 report (Committee, 2000) estimated UK market potential of thermally sprayed coatings at £480 million. Broken down as shown in Table 2-1.

Aerospace	£150 million
Automotive	£30 million
General industry	£100 million
Corrosion protection	£200 million

Table 2-1 Potential Value of Thermally Sprayed Coatings

The UK market for all surface engineering products was estimated for 2010 based on 2005 values in this same report as £21.3 billion.

There are many benefits to industry from coating substrate materials. The benefits accrue from a wide choice of coatings being available which improve the characteristics of particular materials over uncoated materials. Benefits such as improved wear characteristics which will reduce maintenance and replacement costs (Philip, et al., 1999). Corrosion resistant coatings will again reduce maintenance and replacement costs. Very small wear 0.1 mm – 0.2 mm can render a product unserviceable, however surface coating the product can make it serviceable again (Kennedy).

The depth of coating can be very important and thermal spraying can provide relatively thick coating at high deposition rates. The coating process is therefore quite efficient. Because the coating is mechanically bonded to the substrate, excellent adhesion is achieved between the coating material and the substrate.

In many cases components thermally sprayed with appropriate coatings can have superior qualities over new components such as extended lifespan. Thermal spraying can be applied manually or automatically. One objective of this research is to review the design issues of an autonomous robot arm for thermal spraying and to develop key elements of those design issues. The growth of the thermal spray technology sector will require continued advances in process control equipment such as robotics and real time sensors (P.I.Corke, 1994).

2.2 Thermal Spraying Systems

Thermal spraying is a generic term for a range of thermal spraying technologies which are broken down into two main areas; flame and electrical (Hermanek, 2005). Thermal spraying is a process whereby a coating material, metal (alloy), polymer or ceramic in the powder or wire rod state is melted in a flame or electrical arc/plasma and sprayed towards the substrate material to be coated. The coating material then mechanically bonds to the substrate during cooling. Thermal Spraying systems are characterised using factors such as particle velocity, porosity, deposition rate etc. Table 2-2 compares these and other characteristics of thermal spraying systems (AirProducts, 2009 et. al.).

Process	**Particle Velocity (m/s)**	**Adhesion (MPa)**	**Oxide Content (%)**	**Porosity (%)**	**Deposition Rate (kg/hr)**	**Typical Deposit Thickness (mm)**
Flame	40	< 8	10-15	10 -15	1 - 10	0.2 – 10
Arc	100	10 - 30	10 - 20	5 -10	6 - 60	0.2 – 10
Plasma	200 -300	20 - 70	1 - 3	1 – 8	1 - 5	0.2 – 2
HVOF	600 – 800	>70	1 - 2	1 - 2	1 – 5	0.5 – 2

Table 2-2 Thermal Spraying Characteristics

Flame spraying uses oxygen and acetylene or propane as the heat source producing temperatures in the range of 3000 ^{0}C and an aspirating gas of argon or nitrogen. Some systems don’t require an aspirating gas to expel the powder.

Wear and corrosion resistance are the main applications for flame spraying and Table 2-3 provides a list of applications and coating materials used in flame spraying (AirProducts, 2009 et. al.).

Application	**Coating Material**
Corrosion resistance	Aluminium (resistance to acidic corrosion) Zinc (resistance to alkaline corrosion)
Corrosion, wear and cavitation resistance	Self fluxing alloys with nickel/cobolt base and boron/silicon for fluxing

Table 2-3 Flame Spraying Applications

From Table 2-2 it is evident flame spraying has low particle velocity, medium deposition rate but high deposit thickness.

Electrical systems use an electric current to provide the heat source and these are used in the arc and plasma spraying systems. In the arc system a direct current (d.c.)

electric arc is produced between the tips of the wire rod coating material. Compressed gas is used to atomise the molten material and eject it towards the substrate material.

Arc spraying temperatures are in the region of 6000 ^{0}C and with higher particle velocities produce better deposition rates and lower porosity than flame spraying. Table 2-4 provides a list of applications and coating materials used in arc spraying (AirProducts, 2009 et. al.).

Application	**Coating Material**
Corrosion resistance	Aluminium (resistance to acidic corrosion) Zinc (resistance to alkaline corrosion)
Electromagnetic Interference (EMI) Shielding	Copper, Zinc, Aluminium
Reclamation of bearing	Steel, Bronze

Table 2-4 Arc Spraying Applications

Plasma spraying systems use a d.c current to produce an ionised gas (plasma) which is the heat source for the powder fed coating material. This system produces high temperatures 1200^{0} – 16000^{0}C and particle velocities. Deposition rates are significantly lower than arc spraying as is deposit thickness. However plasma spraying provides high quality coatings. Application examples are shown in Table 2-5 (AirProducts, 2009 et. al.).

Application	**Coating Material**
Fretting wear resistance	Tungsten carbide/cobolt
Wear resistance	Alumina/ Chromium oxide ceramic
Thermal Barrier	Zirconia
Friction	Molybdenum

Table 2-5 Plasma Spraying Applications

High velocity oxy fuel (HVOF) systems have the combustion process internally in the system which produces high velocity and pressure spraying. Flame speed can reach 2km/s with particle velocities of 600-800ms. Table 2-6 lists applications of HVOF systems (AirProducts, 2009 et. al.).

Application	**Coating Material**
Fretting wear resistance	Tungsten carbide-cobolt
Wear resistance	Cobolt alloys
High Temp. Oxidation/corrosion resistance	Nickel chromium
Prosthesis	Biocompatible Hydroxylapatite

Table 2-6 HVOF Spraying Applications

From the literature review it can be concluded that powder flame spraying will be the system of choice for our research. This is based on the powder flame spraying features listed in Table 2-7.

- Powder thermal flame spraying using an oxy-acetylene torch is the lowest cost system.
- The energy and complexity used is lower than any of the other system thus reducing Health and Safety issues for research
- Although powder thermal flame spraying is the oldest technology the applications benefiting from powder thermal spraying are relevant as much today as they have been in the past.

Table 2-7 Powder Flame Spraying Features

From the comparison of thermal spraying characteristics as shown in Table 2-2 we can see that the flame spraying process has two key weaknesses. These are high porosity and low deposition rates.

The spray angle of the torch directly affects porosity, oxide content and adhesion and therefore product quality. The torch should remain perpendicular to the substrate or at least within ±5 degrees (USArmyCorpofEngineers, 1999). Any slight miss alignment of the thermal spray with the substrate will introduce an increase in porosity therefore the use of an autonomous robotic system with real-time feedback control to maintain torch prependicularity with the substrate will improve product quality.

Flame spraying has low deposition rates in comparison to other thermal spraying techniques. Therefore if overall production speed can be increased by automating the flame spraying process then with its lower capital costs the original flame spraying technology can continue to compete.

A key objective of this research was the identification of technology and techniques for reducing production time and increasing quality and safety of the powder thermal spraying process.

2.3 Powder Thermal Spraying Process

This research specifies powder thermal spraying technology. It is the oldest thermal spraying process. However it is a process that is still used extensively today because of the range of coating material available and the lower energies required which reduce the health and safety risks. There are still serious health and safety risks associated with this flame spraying technology such as noise, heat, explosion and ultra violet light. To obtain an understanding of the powder thermal spraying process manual thermal spraying was conducted as shown in Figure 2-1.

Figure 2-1 Thermal Spraying

Initially the substrate was preheated using only the oxyacetylene flame. Once heated the coating powder was turned on and the torch moved closer to the substrate where a layer of coating powder was applied to the substrate. The powder was then turned off and the torch lowered further towards the substrate to wet-out or fuse the coating powder to the substrate. This process requires highly skilled and experienced manual operators. However manual spraying is tedious and can result in poor quality results (Kutay, et al.). Robotic systems can produce consistently superior results.

A vast majority of components are sprayed manually and the development of an autonomous robot arm to carry out the thermal spraying process could reduce costs and Health and Safety risks. Autonomous in this instance refers to the process of thermal spraying objects with predetermined coating materials but of various unknown shapes in unknown orientations. Figure 2-2 shows a schematic of a powder thermal spraying system.

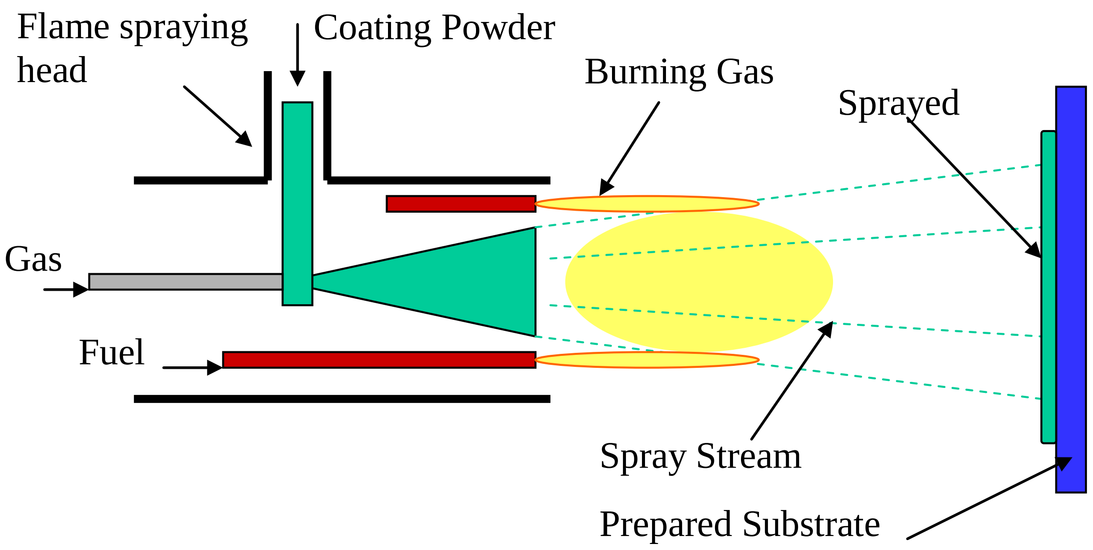

Figure 2-2 Powder Flame Spraying

Fuel is supplied to the nozzle which is ignited in the correct proportion to produce a flame. Powder coating material is fed into the nozzle where an aspirating gas expels the powder into the flame. Not all systems require an aspirating gas. The coating material melts in the flame which is directed at the substrate material to be coated.

The molten material bombards the substrate and upon cooling the coating material mechanically bonds to the substrate. Product Quality such as porosity, oxide content and adhesion are affected by spray angle. Good quality spraying is provided by a spray angle of $90^0 \pm 5^0$ (USArmyCorpofEngineers, 1999).

The coating process must occur in a very precise manor to ensure a quality deposit. Following surface preparation, there can be up to three main stages in applying a metallic coating to a substrate and the location of the torch for each stage is an important design and control parameter. These include pre-heating the substrate, spraying the substrate with the coating material and finally fusing the coating to the substrate. Clearly the length of time taken for each stage is another design and control parameter. A key aspect of this research is the consideration of the control of the torch tip position with respect to the substrate.

Spray distance directly affects quality such as porosity, oxide content and adhesion (USArmyCorpofEngineers, 1999) therefore correct spray distance must be maintained. A consequence of maintaining correct spray distance is that the spray must move parallel to the substrate surface which is a difficult activity for manual spraying. Transducers to provide automatic control of spray distance is a feature of this research. Spray distances vary depending on the process. An example of spray distances for the three stages described above is shown in Figure 2-3. These are typical distance ranges used during thermal spraying of various surface coatings based on Castolin Eutectic (Castolin) general procedure guidelines.

The pre-heat height is between 100 mm and 200 mm from the substrate, the coating material spray height is between 50 mm and 100 mm from the substrate and finally the wet out height or fusing height is up to 10 mm from the substrate.

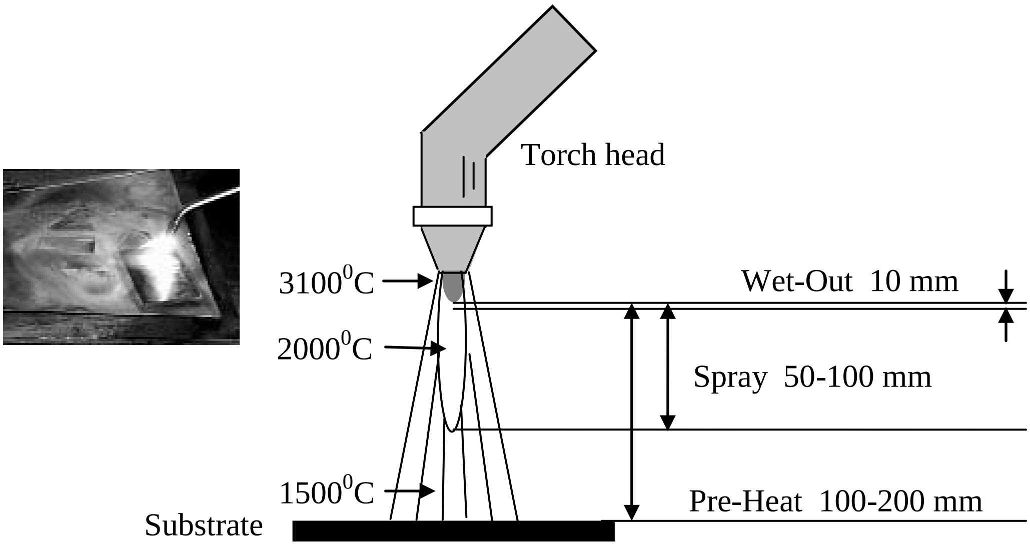

Figure 2-3 Torch Spray Locations

The control of these heights can be pre-programmed with a prior knowledge of the product shape and location using open loop control or by pre-programmed closed loop control. This research develops ideas for closed loop autonomous control of the thermal spraying robot arm which can identify products of arbitrary shape and in arbitrary orientations, thus reducing significantly setup costs. Examples of some of the types of thermal spraying torches available for power and polymer coatings are shown in Figure 2-4 and Figure 2-5.

Figure 2-4 Powder Fed Torch

Figure 2-5 Polymer Fed Torch

CHAPTER 3

ROBOT ACTUATORS, TRAJECTORY PLANNING AND DYNAMICS DESIGN

3.1 Introduction

The control of robot links is achieved using joint actuators. There are fundamentally three types of robot actuators, hydraulic, pneumatic and electric motor. Table 3-1 is an extract from Niku of the key advantages and disadvantages (Niku, 2001) of these actuators.

Hydraulic	**Electric motor**	**Pneumatic**
Advantages: Good for large robots and heavy payloads Can work in a wide range of speeds Self lubricating	Advantages: Good for all sizes of robots Good for high precision robots High power conversion efficiency	Advantages: Inexpensive and simple Good for on off applications
Disadvantages: Viscosity of oil changes with temperature Very susceptible to dirt and other foreign material in oil. Low power conversion efficiency	Disadvantages: Needs gears Needs break Backlash and elasticity	Disadvantages: Low power to weight ratio Fluid compressibility errors

Table 3-1 Robot Actuators

The hydraulic actuators are suitable for large heavy payload robots and are susceptible to dirt; therefore they are not suitable for thermal spraying robots. Pneumatic actuators are low power and have fluid compressibility therefore they are not suitable for thermal spraying robots. The electric motor advantages outweigh their disadvantages for a thermal spraying robot. Reviewing commercially available articulated robot manipulators (ABB, 2009) (FANUC, 2008) (Mitsubshi, 2008) which use electric motors, electric motor actuators were chosen for this research.

Figure 3-1 shows a three axis articulated robot manipulator whose joints are driven by rotary electric motors and gearboxes.

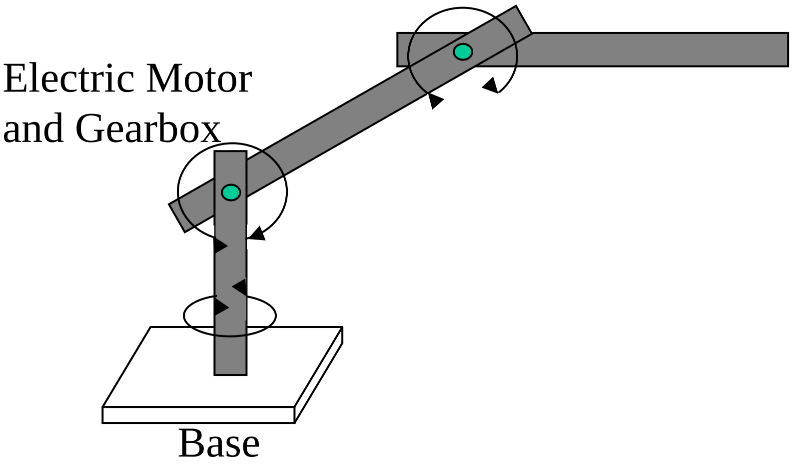

Figure 3-1 Robot Manipulator

Common types of electric motors for robot applications are the stepper motor permanent magnet d.c motor and the brushless motor (a.c. polyphase). Electric motors are high speed low torque devices. Torque can be increased with an associated reduction in speed by using gears. In some high speed applications direct drive motors are used.

The following sections review a range of electric actuators and drive technology for robot applications with a view to specifying the actuator for this research. The main source material for this review is (Rizzoni, 2000), (Hughes, 1990), (Niku, 2001), (Jones, 2008) and (Microchip Technology Inc., 2003).

3.1.1 Stepper Motor

Stepper motors are ideal for open loop position control as precise angular position can be achieved from a known home position by providing pulses to the phase windings of the stepper motor via power electronic devices such as Metal Oxide Semiconductor Field Effect Transistors (MOSFETS). Stepper motors are available in a range of torque values, typically from 1 µNm to 40 Nm. The step pulses can be generated by specially designed chips or microcontrollers. With the microcontroller/digital signal controller system monitoring the pulses motor position can be monitored.

There are basically three types of stepper motor; the variable reluctance stepping motor, the permanent magnet rotor stepping motor, and the hybrid stepping motor. A permanent magnet stepping motor type uses a magnetic rotor and the hybrid stepping motor has a multi-toothed rotor. The hybrid stepping motor is a combination of variable reluctance and permanent magnet stepping motors. Figure 3-2 shows the construction of a variable reluctance motor with three phase coils.

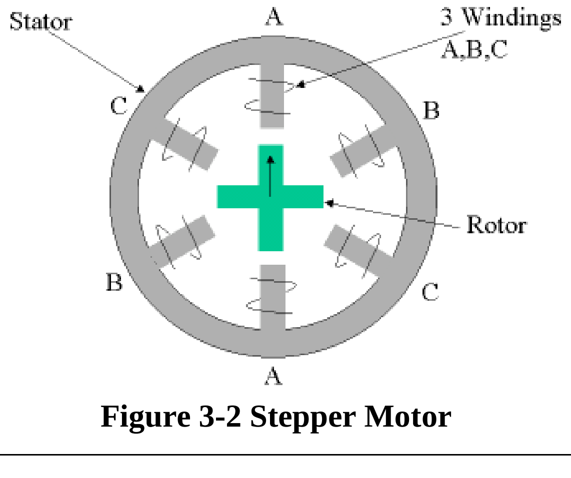

Figure 3-2 Stepper Motor

Rotation of the rotor can be achieved by sequentially applying power to each coil in turn thus providing direct digital control via power transistors or MOSFETS. The rate at which coil pulses are applied, their sequence and the voltage applied provide motor speed, direction and torque control. The control signals can be generated and applied to the power MOSFETS using specialist translator chips such as the LD297 (STMicroelectronics, 2001) or programming a Microchip^{TM} Digital Signal Controller (Microchp Technology Inc., 2009).

Figure 3-3 shows a typical static torque / angle curve for such a motor.

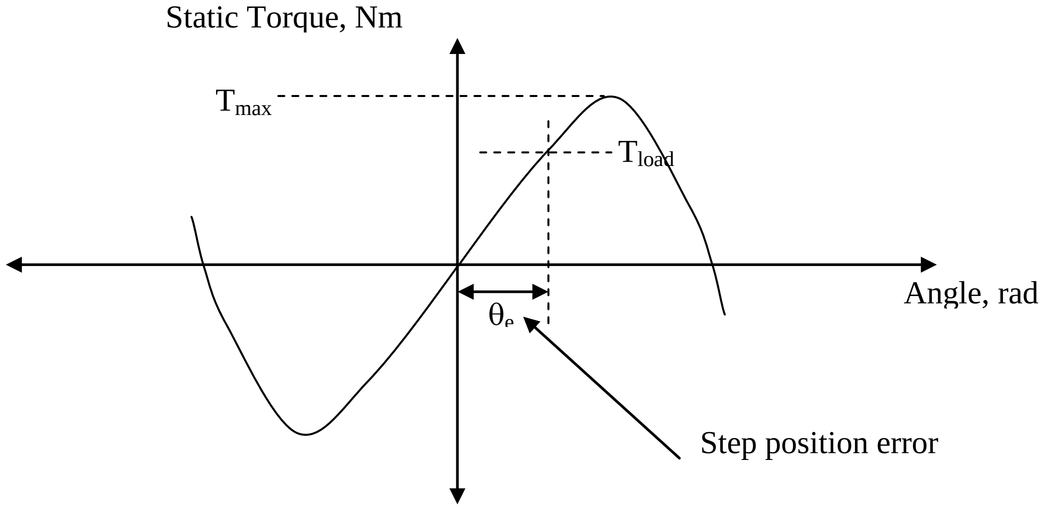

Figure 3-3 Stepper Motor Static Torque Characteristic

Step position error is also shown in Figure 3-3. Stepper motors with very small step angles, as small as 1.8^0 are available. With gearing and or micro-stepping, this step angle can be further reduced. Micro stepping is the control process of applying variable power levels to two phases of a stepper motor simultaneously.

One feature of the stepper motor, which is both an advantage and disadvantage, is that when power is applied to the motor the motor is in a locked position. This is an advantage from a safety point of view as the robot arm cannot start driving if power is accidentally applied to one of the coils e.g. if a power transistor short circuited. This feature also works in reverse i.e. with no power applied there is no holding torque thus a raised arm would fall until it hit the ground or table this is why electric motors in robot applications require a break. Permanent magnet dc motors start driving a robot arm as soon a power is applied which could possibly cause an accident. It may be possible to use a worm gear in some low load / speed applications. The worm gear is fitted to the motor shaft and a cog fitted to a robot arm shown in Figure 3-4.

This would prevent the arm from moving while the electric motor is not powered. The worm gear can however drive the robot arm in both directions when the motor is operating. However this introduces additional friction in the system and is not generally recommended. A break is the preferred method of holding arm position during static control. No further analysis of this type of motor is warranted as stepping motors are more for open loop small robot applications.

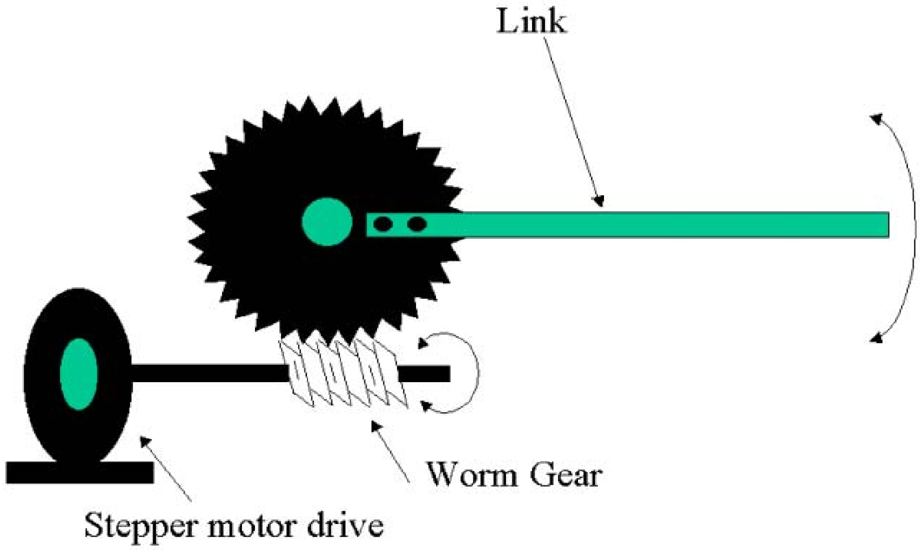

Figure 3-4 Worm Gearing

3.1.2 Permanent Magnet d.c. Motor

The permanent magnet dc motor consists of a permanent magnet of ferromagnetic ceramics or rare earth magnets on the stator. Examples of rare earth magnets are Neodymium (Nd), Samarium Cobolt (SmCo), and the alloy of Neodymium Ferrite and Boron (NdFeB). Research is continuing to find new magnetic materials with even higher flux densities per volume thus reducing further motor sizes. The d.c. supply is fed to the rotor (armature) via a commutator.

A key design issue of a permanent magnet d.c. motor is the torque - speed - voltage characteristics and power ratings of a motor. At steady state the equivalent circuit for the permanent magnet d.c. motor is shown in Figure 3-5.

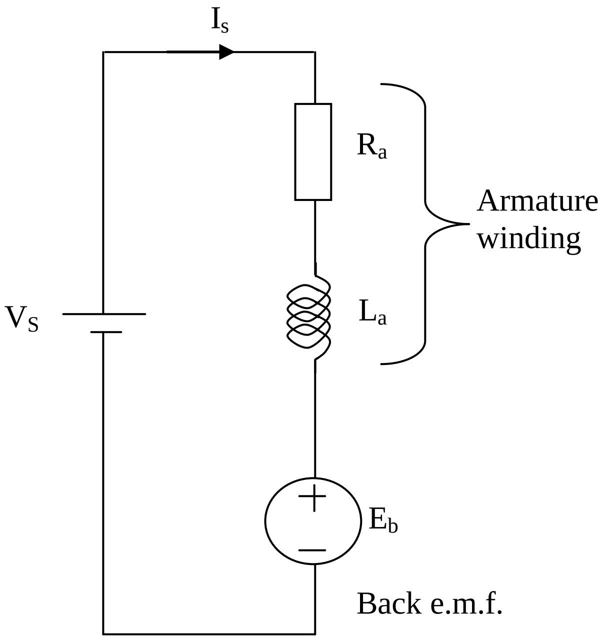

Figure 3-5 Permanent Magnet d.c. Motor Equivalent Circuit

This circuit produces the steady state voltage and power equations given in Equation (3-1) and (3-2).

$V_s = I_sR_a + k_{aPM}\,\omega_m \qquad (\,V\,)$ **(3-1)**

$V_sI_s = I_s^2R_a + I_sk_{aPM}\omega_m \qquad (\,W\,)$ **(3-2)**

where :

- V_s is the d.c. supply voltage (V)
- I_s is the supply current (A)
- k_{aPM} is the armature constant (V/r/s)
- V_sI is electrical input power (W),
- $I_s^2R_a$ is copper losses (W),
- $I_sk_{aPM}\omega_m$ is mechanical output power in (W)

Using the torque equation $T = k_{TPM}.I_s$ (Nm) and rearranging produces the torque and speed equations given in Equations (3-3) and (3-4)

$$T = \frac{V_s}{R_a}k_{TPM} - \frac{\omega_m}{R_a}k_{aPM}K_{TPM} \quad (Nm)$$ **(3-3)**

$$\omega_m = \frac{V_s}{k_{aPM}} - \frac{TR_a}{k_{aPM}k_{TPM}} \quad (rad\,/\,s)$$ **(3-4)**

where:

- T is motor torque (N-m)
- V_s is supply voltage (average if PWM supply) (V)
- R_a is armature resistance (Ω)
- K_{TPM} is torque constant (Nm/A)
- ω_m is motor speed (rad/s)
- K_{aPM} is back e.m.f. constant (V/rad/s or V/1000/min)

These equations produce the torque speed voltage characteristics of a permanent magnet d.c. motor which are shown in Figure 3-6.

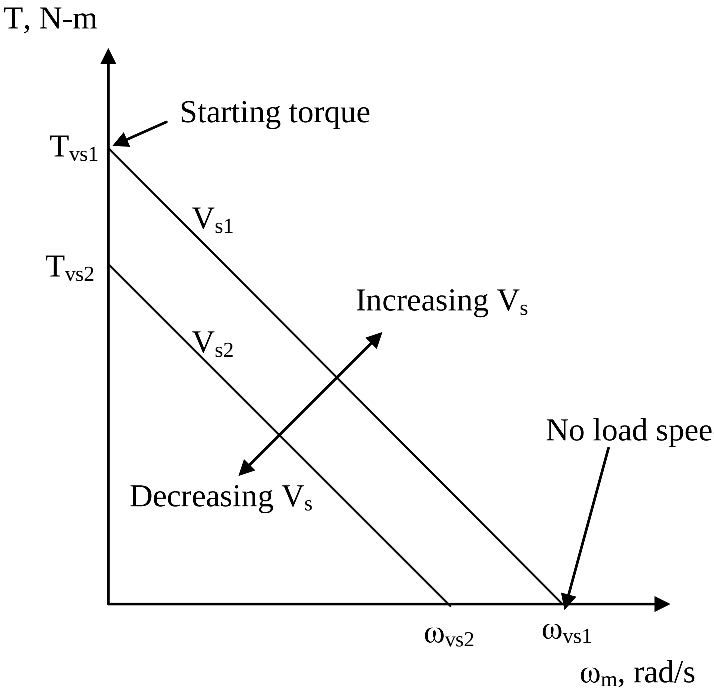

Figure 3-6 Permanent Magnet d.c. Motor Torque Speed Voltage Characteristics

This supply voltage, torque-speed characteristic makes the permanent magnet d.c motor ideal for robot servo motor applications. The permanent magnet d.c. motor is converted to a servomotor by the application of speed and position transducers to the motor. Power ratings range from a few watts to a few kilowatts.

From these characteristics it is clear motor speed is controlled by varying the d.c. supply voltage and direction is controlled by changing the d.c. supply polarity. The angular position of the motor shaft is determined using a position transducer such as an absolute encoder mounted on the motor shaft. This provides a position feedback control signal which can be differentiated to provide velocity. Tachometers may be used for direct speed measurement.

The drive technology associated with speed and direction control is relatively straight forward. Speed can be controlled using Pulse Width Modulation (PWM) of the supply voltage via power electronics such as power transistors or MOSFETS. A PWM signal is shown in Figure 3-7

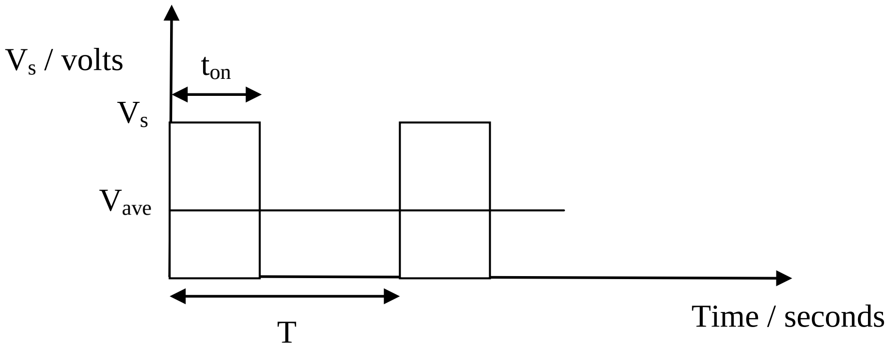

Figure 3-7 PWM Signal

The average supply voltage V_{ave} is given in Equaton (3-5).

$$ — \qquad (V) \tag{3-5} $$

where:

- V_{ave} is the average d.c voltage (V)
- V_s is the supply voltage (V)
- t_{on} is the on period (s)
- T is the Pulse Width Modulation Period (s) ,
- PWM frequency $f = 1/T$ Hz.

The production of the PWM signal is achieved using Programmable Logic Controllers or Microcontrollers/Digital Signal Controllers. Direction can be achieved using a H-Bridge.

The modified H-bridge shown in Figure 3-8 (Newton, 2002) provides individual MOSFET direction control and pulse width modulation speed control of a permanent magnet d.c. motor using MOSFETS for power and npn transistors for logic control. The modification to the H-bridge provides for control of motors at voltages higher than the control logic voltages. Opto-isolators could be provided on the inputs if necessary.

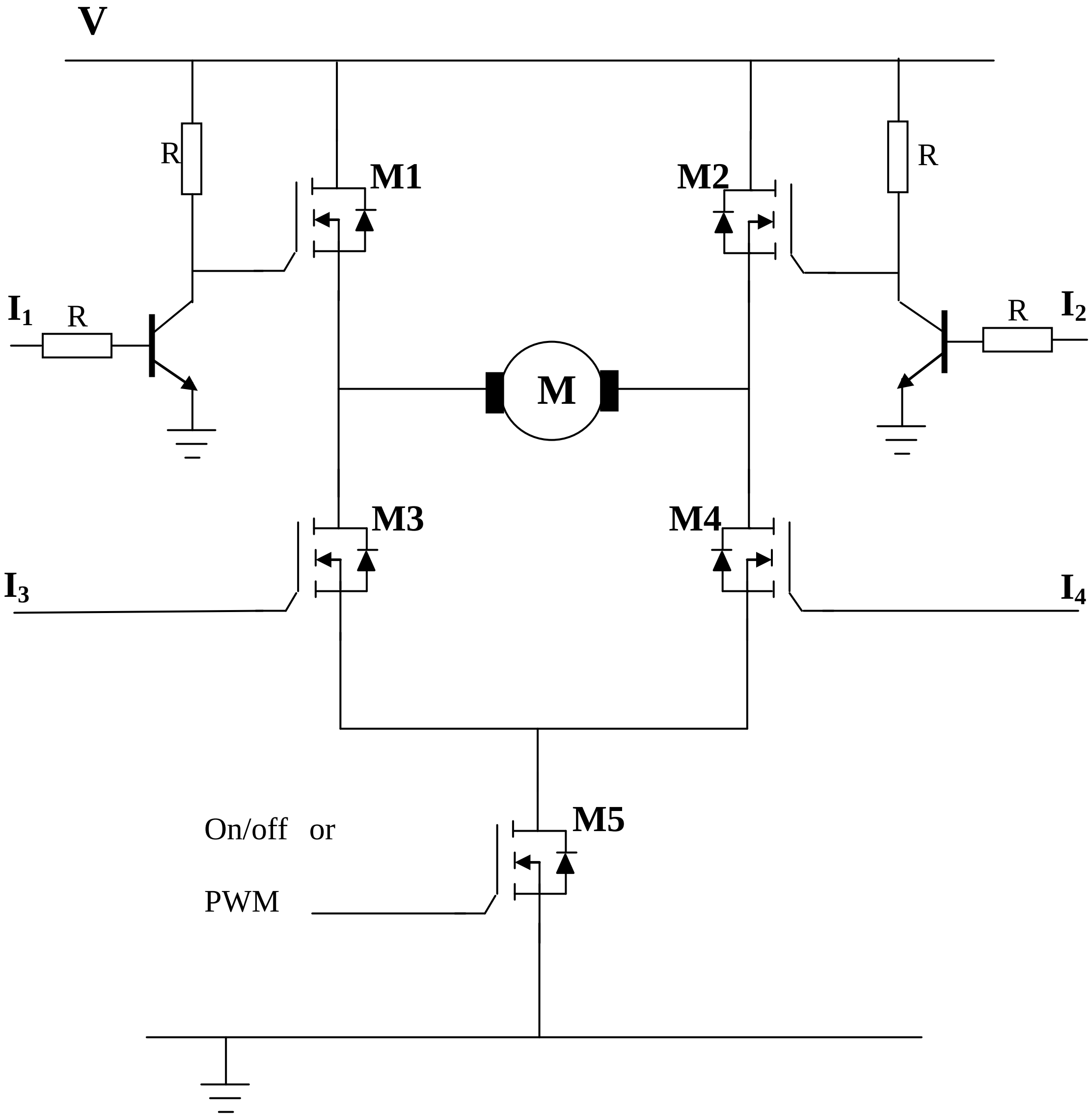

Figure 3-8 H-Bridge

The logic for direction control is shown in Table 3-2 assuming the PWM MOSFET is on. Prevention of the illegal condition shown in Table 3-2 must be provided by the logic controller and overload protection.

Inputs				
I_1	**I_2**	**I_3**	**I_4**	**Motor condition**
0	0	0	0	motor off
1	0	0	1	M1 and M4 on (forward)
0	1	1	0	M2 and M3 on (reverse)
1	1	1	1	illegal condition short circuits

Table 3-2 H-Bridge Logic

Figure 3-9 is a block diagram showing the control elements of a permanent magnet d.c. motor position servomotor. The controller compares the position set point to the motors position .The controller produces the necessary direction and speed control signals to actuate the motor to the desired position.

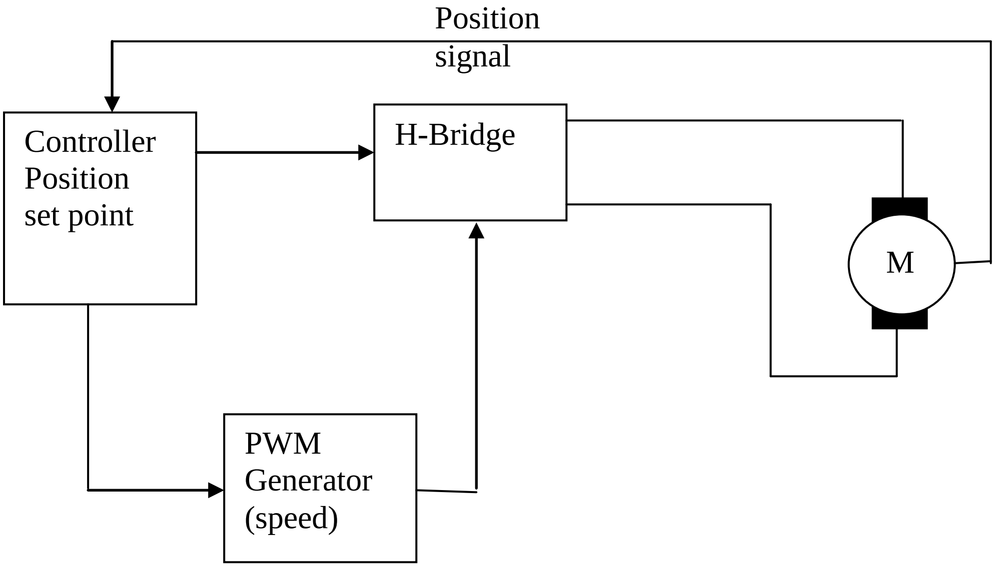

Figure 3-9 Permanent Magnet d.c. Motor Position Servomotor

PMDC motors have been popular for many years because of the ease of control characteristics; however they have problems in particular the need for mechanical commutation and high rotor inertia. The development of reduced cost in advanced power electronics and digital signal controller technology have facilitated a new breed of motor with similar characteristics namely the brushless motor sometimes referred to as d.c brushless motor or a.c. brushless motor depending on whether they are trapezoidal or sinusoidal in construction and inverter type.

The characteristics of the PMDC motor makes them suitable for the thermal spraying robot arm application. However the advancement of brushless motors in the last few years has probably numbered the days PMDC motors will be used for industrial robot applications. In fact the price differential between permanent magnet and brushless motors is now as low as 10% (Robinson, 2006).

3.1.3 Brushless Motor

Brushless (BL) motors are synchronous polyphase a.c. motors which can be used as servomotors when used in conjunction with speed and position transducers such as tachometers or absolute encoders. The brushless motor has similar linear torque speed characteristics as the permanent magnet d.c. motor. Brushless motors have advantages over PMDC motors such as better torque speed characteristics, high dynamic response, high efficiently, noiseless and long life however they are more expensive and require more complex control systems. Brushless motors are supplied with a d.c. voltage source and require a d.c. to a.c. inverter. The rotor consists of a permanent magnet of ferromagnetic ceramics or rare earth magnets. The stator (armature) consists of polyphase windings usually three which generate a rotating magnetic field and therefore a torque on the permanent magnet rotor. The stator windings can be connected in three-phase star or delta formation. The windings are wound in one of two winding variations trapezoidal and sinusoidal giving rise to the brushless motor trapezoidal or sinusoidal type which require different d.c. to a.c. inverters. The trapezoidal windings type produce a trapezoidal back e.m.f. and are usually controlled by a six step inverter supplying switched d.c. voltages and currents to the windings whereas the sinusoidal windings type produces sinusoidal backs e.m.f.'s and require a more complex sinusoidal a.c. inverter. The sinusoidal version has the advantage of producing a smoother torque output but at extra cost due to the more complex inverter.

A disadvantage with PMDC motors is that commutation, conversion of the d.c. supply to a.c. and distribution to the windings, is done via brushes were as commutation of brushless motors is achieved electronically with associated improvement in losses and maintenance. The correct sequence for electronic commutation is achieved by monitoring the rotors position using either low cost hall effect sensors or for more accurate position measurement using absolute position encoders. Some brushless motors don't use sensors but monitor the back e.m.f. to determine rotor position. These are known as sensor less brushless motors.

A major advantage of the brushless motor is constant torque speed control is easily achieved by varying the d.c. supply voltage as they have a linear torque speed characteristic like the PMDC motor. Direction control is easily achieved by switching two phases in the three phase motor which is done by the logic control systems in the inverter.

The brushless motors steady state voltage and torque equations are given in (3-6) and (3-7) for a brushless motor of the trapezoidal type fed from a six step inverter i.e. two phases are energised at each commutation step. Note two back e.m.f.'s are produced as there are two phases energised at any one time step.

$$V = 2K_{aBL}\omega_m + R_w I^2 \qquad \textbf{(3-6)}$$

$$T = K_{TBL} I_{rms} \qquad \textbf{(3-7)}$$

where:

- V is the supply volage (V)
- K_{aBL} is the back e.m.f. constant
- ω_m is the motor speed (rad/s)
- I is the supply current (A)
- R_w is the winding resistance (phase to phase)

A typical constant torque speed curve for a brushless motor is shown in Figure 3-10. The constant torque is achieved by varying the supply voltage.

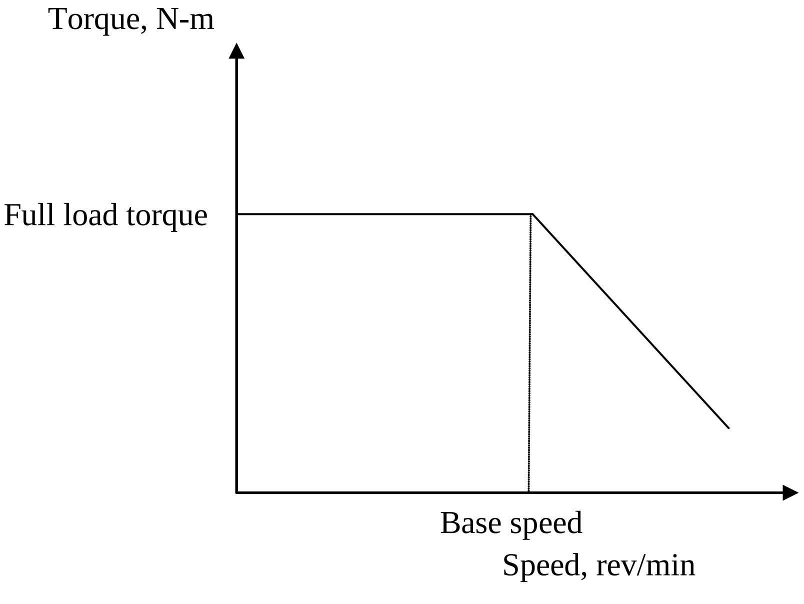

Figure 3-10 Brushless Motor Torque

Comparisons between the permanent magnet and brushless motors are shown in Table 3-3.

Feature	**Permanent magnet**	**Brushless**
Commutation	Brushes	Electronics
Efficiency	Moderate	High
Rotor inertia	Higher	Lower
Speed	Lower	Higher
Cost	Lower	Higher
Control	Simple and inexpensive	Complex and expensive

Table 3-3 Comparison of Permanent Magnet and Brushless Motors

The table clearly shows that the Brushless motor has many advantages over permanent magnet types such as high efficiency and lower rotor inertia. With falling costs and improved inverter technology they are becoming the motor of choice in many control applications.

A Block diagram of a 3 phase brushless motor and inverter drive system is shown in Figure 3-11. Small 3 phase brushless d.c motors can be supplied from single phase supplies. To convert this brushless motor to a servomotor speed and position transducer signals would be used to control the d.c. link and switching sequence. Sometimes the rotor position transducers in the rotor can be used or position servo control

.

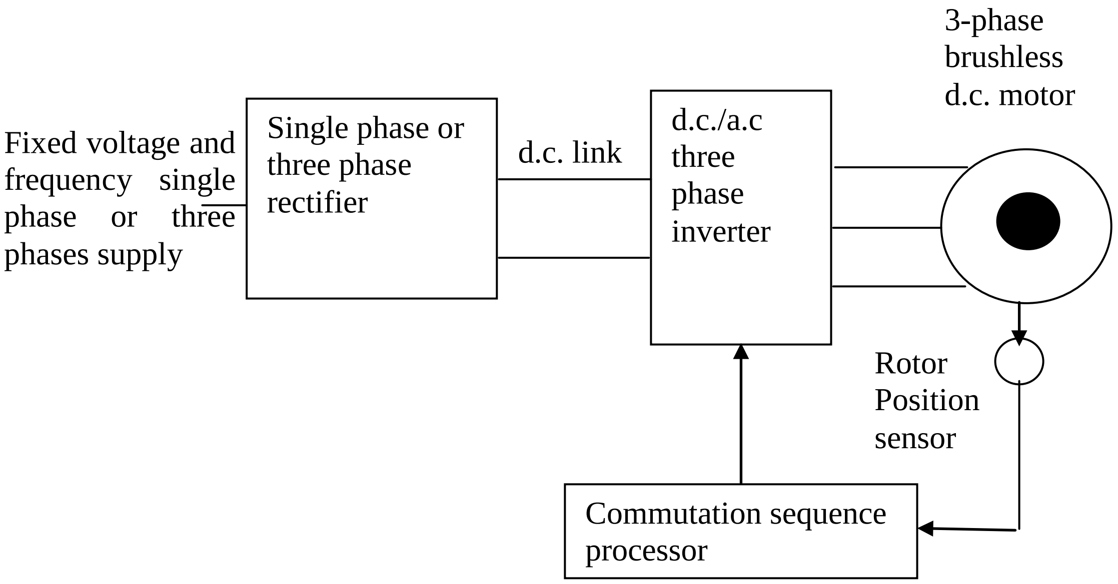

Figure 3-11 Brushless Motor and Inverter

The single phase or three phase supply is first rectified to provide a d.c. supply of appropriate power rating. This d.c can be varied via a controlled rectifier or PWM if necessary. The d.c supply is fed to a d.c. to a.c. inverter which supplies the three phase brushless motor. The commutation process is controlled by the commutation sequence processor based on information from the position sensors, hall-effect or absolute encoder. Each commutation sequence energises one phase with positive current (current entering a winding) , one phase with negative current (current leaving a winding) and the third phase is de-energised based on the position of the rotor. Ideally the stators magnetic field and the rotors magnetic field should be 90^0 out of phase with each other for maximum torque, however in a trapezoidal version the commutation switching occurs between 60 and 120 degrees. A six step d.c – a.c. inverter power stage drive circuit using MOSFETS for a 3-phase star connected brushless motor is shown in Figure 3-12 and the commutation switching sequence is shown in Table 3-4. The phase current commutation sequence graphs of a six step inverter drive are shown in Figure 3-13.

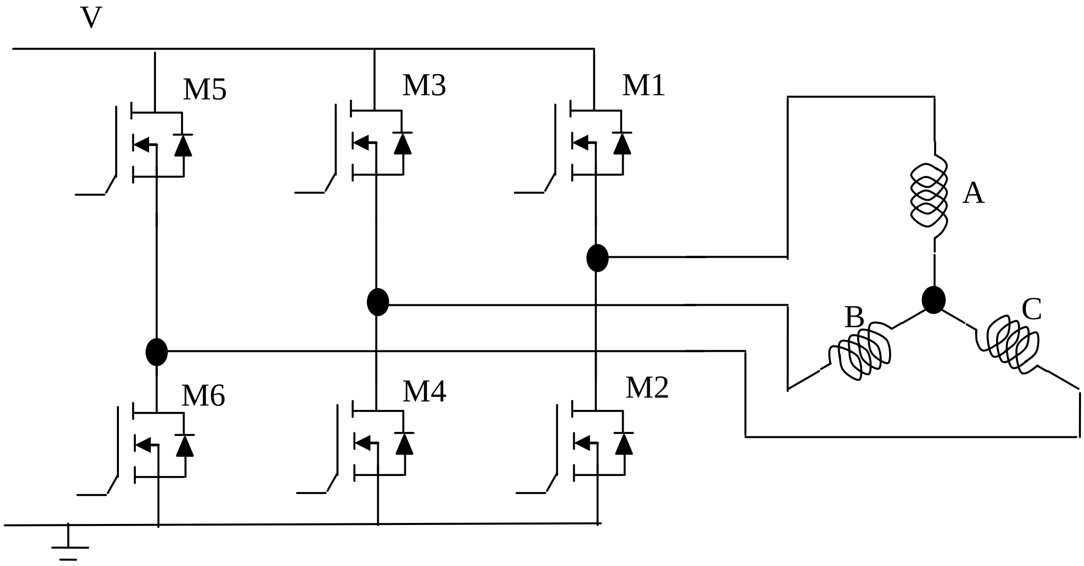

Figure 3-12 Six Step Inverter

Step1	A – B	M1 – M4 on
Step 2	A – C	M1 – M6 on
Step 3	B – C	M3 - M6 on
Step 4	B – A	M3 – M2 on
Step 5	C – A	M5 – M2 on
Step 6	C – B	M5 – M4 on

Table 3-4 Commutation Sequence

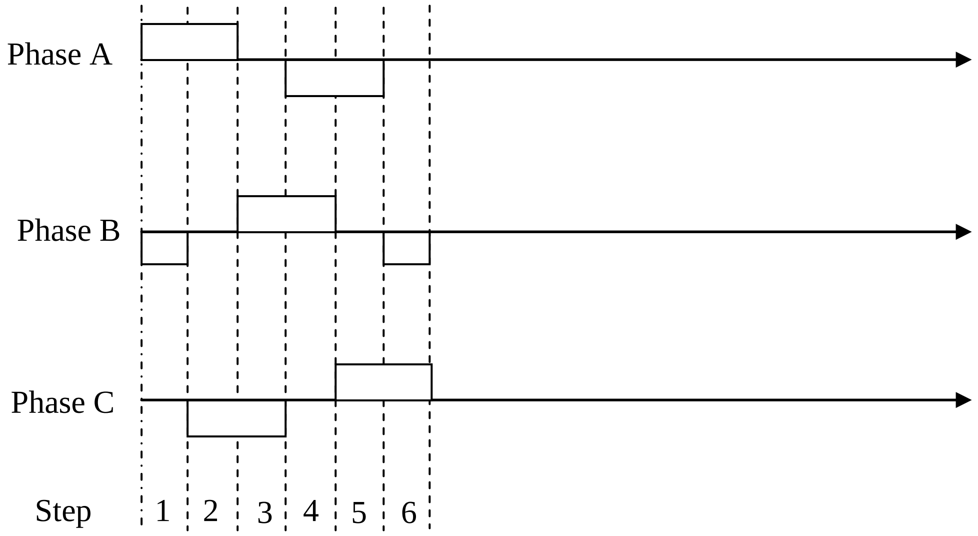

Figure 3-13 Phase Current Commutation Graphs

Power ratings for brushless motors range from a few watts up to 100 kW (Hughes, 1990). This makes them ideal for larger robot manipulator applications as is confirmed by a review of commercially available robot manipulators.

Following this review of electric actuators the brushless motor (trapezoidal type) with associated speed and position transducers will be the actuator of choice for the thermal spraying robot because of its torque speed characteristic and relatively straight forward control electronics and cost.

Although not required for this research there is current research ongoing on sensorless brushless motor control which would be an interesting area for future research. One such paper on this subject is by (Bonfe, et al., 2008).

3.1.4 Megatorque^{TM} Motor

There are high speed applications which require direct dive motors. One such motor worth mentioning in this research is the Megatorque^{TM} motor. This is a direct drive motor, which eliminates some of the problems associated with gearing such as backlash, elasticity, cost and maintenance. Advantages of the Megatorque motor according to the manufacturer (NKS, 2009) are listed in Table 3-5.

- 120 Nm torque at a speed of 3 rps
- Repeatability of +/- 2.1 sec
- Brushless structure and permanently lubricated heavy-duty bearings for maintenance-free operation
- Hollow core structure allowing wires or pipes to run inside the motor

Table 3-5 Megatorque Motor Characteristics

No further analysis of this type of motor is warranted as the thermal spraying robot arm is not a high speed application a feature of direct drive systems. Direct drive systems also require significantly more complex control strategies as the complete systems dynamic model must be taken into account. This is however an interesting area for further research. One such paper on this subject is by (Dianqi. L, 2007).

3.1.5 Harmonic Drive

Apart from standard gearing of electric motors there are specialist gearing systems one of which is the harmonic drive. This is a special gear mechanism with specific advantages for use in robot actuator joints. They operate on the principle that an elliptical central gear engages and turns a cylindrical outer gear. The elliptical gear normally has one or two fewer teeth therefore every full turn or half turn of the elliptical gear rotates the outer cylindrical gear by only one or two teeth depending on teeth ratio.

This mechanism has a number of advantages according to the manufacturer Harmonic Drive^{TM} (Harmonic-Drive, 2009) which are listed in Table 3-6.

- Position accuracy of less than one minute of arc
- Repeatability within a few seconds of arc.
- High output torque
- Practically zero backlash
- Central hollow shaft for passing cables through gearing (this does not however provide continuous rotation

Table 3-6 Harmonic Drive Characteristics

The accuracies needed in thermal spraying do not necessarily warrant this type of gearing and therefore no further research into this type of specialist gearing is necessary.

3.1 Trajectory Planning

3.1.1 5th Order Trajectory Polynomials

Actuators must move the robot arm in particular trajectories either based on a pre-programmed routine or in response to sensory control input. A path for the robot arm is a set of positions in either tool space or joint space and a trajectory is movement over this path in a particular time profile.

To ensure smooth position, velocity and acceleration trajectories a fifth order polynomial may be used as shown in Equation (3-8) (Niku, 2001).

$$\theta(t) = a_0 + a_1 t + a_2 t^2 + a_3 t^3 + a_4 t^4 + a_5 t^5 \qquad \textbf{(3-8)}$$

The fifth order position polynomial is differentiable twice giving continuous trajectory functions in time for velocity and acceleration shown in Equations (3-9) and (3-10).

$$\dot{\theta}(t) = a_1 + 2a_2 t + 3a_3 t^2 + 4a_4 t^3 + 5a_5 t^4 \qquad \textbf{(3-9)}$$

$$\ddot{\theta}(t) = 2a_2 + 6a_3 t + 12a_4 t^2 + 20a_5 t^3 \qquad \textbf{(3-10)}$$

These equations can be solved for the unknown coefficients based on boundary conditions for initial and final time, position, velocity and acceleration and inverse matrix mathematics.

Figure 3-14 shows the velocity change with and without a polynomial trajectory. The dashed line shows an instant change in velocity from zero to a fixed velocity causing an abrupt change in acceleration something the actuators are unlikely to achieve. The solid line indicates a smooth change in velocity via a polynomial over a small time frame.

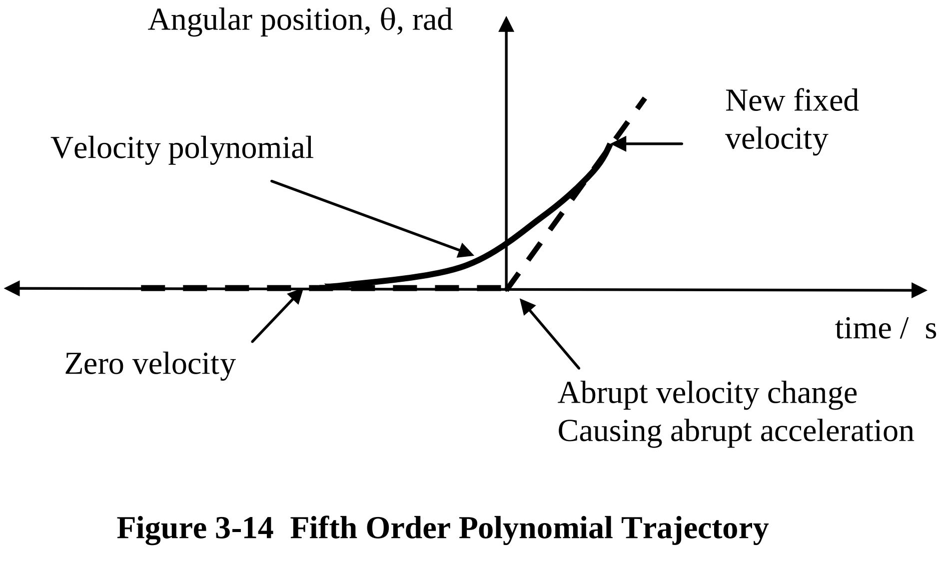

Figure 3-14 Fifth Order Polynomial Trajectory

3.1.2 Trajectory Planning Algorithm

A Matlab^{TM} program was developed named `trajectory.m` to investigate the effect of various boundary conditions expected for a robot manipulator during a thermal spraying process. Figure 3-15 shows the trajectory planning algorithm developed. The complete trajectory planning Matlab^{TM} program listing is provided in Appendix A.

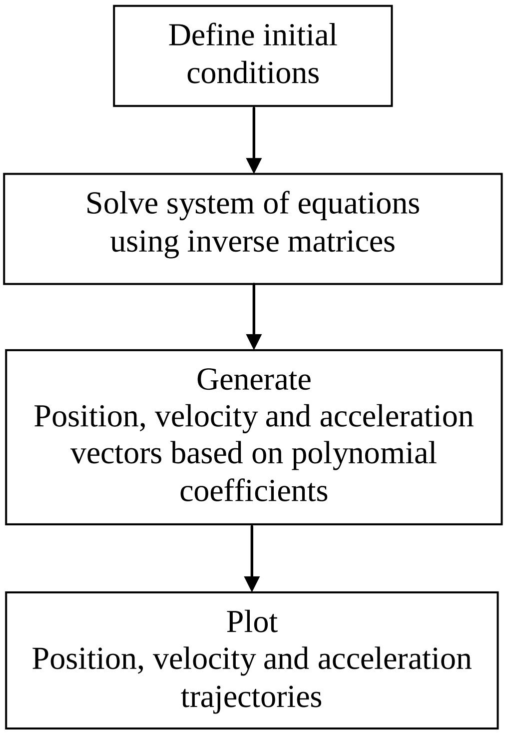

Figure 3-15 Trajectory Planning Algorithm

The thermal spraying process is relatively slow and requires short start stop movements. This suggests a set of initial conditions shown in Table 3-7 for each robot joint.

Initial position	0 - 2π	(radians)
Final position	0 - 2π	(radians)
Initial velocity	0	(rad/s)
Final velocity	0	(rad/s)
Initial acceleration	0	(rad/s^2)
Final acceleration	0	(rad/s^2)

Table 3-7 Trajectory Planning Boundary Conditions

Running the trajectory planning Matlab™ program with these initial conditions and an initial joint position of 0.4 radians and a final joint position of 0.6 radians over a 2 second time frame generates the following solution for the 5th order polynomial coefficients. Coefficients = [0.4, 0, 0, 0.25, -0.1875, 0.0375].

Using these coefficients in the joint position, velocity and acceleration trajectory polynomials generates the solution plots shown in Figure 3-16 on a single axis. Individual plots for position, velocity and acceleration are shown in Figure 3-17. This program may be used in the design process so at to investigate and compare to specifications joint velocity and acceleration for various trajectories. The trajectory results shown in Figure 3-16 confirm the smooth trajectory for position, velocity and acceleration of the joint based on the boundary conditions provided.

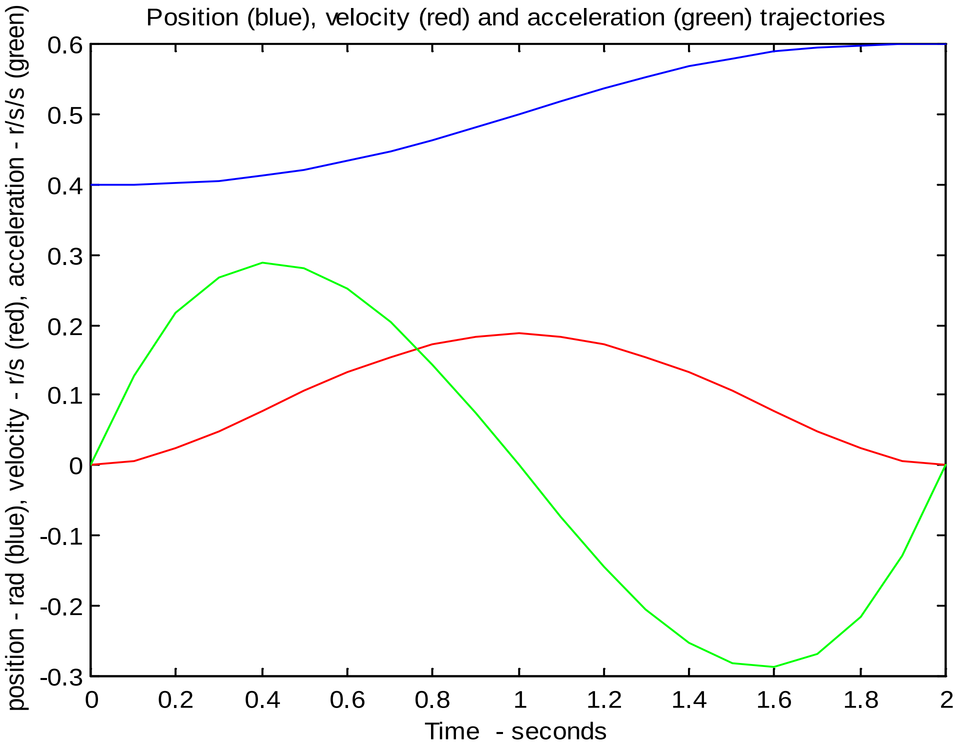

Figure 3-16 Position, Velocity, Acceleration Trajectories

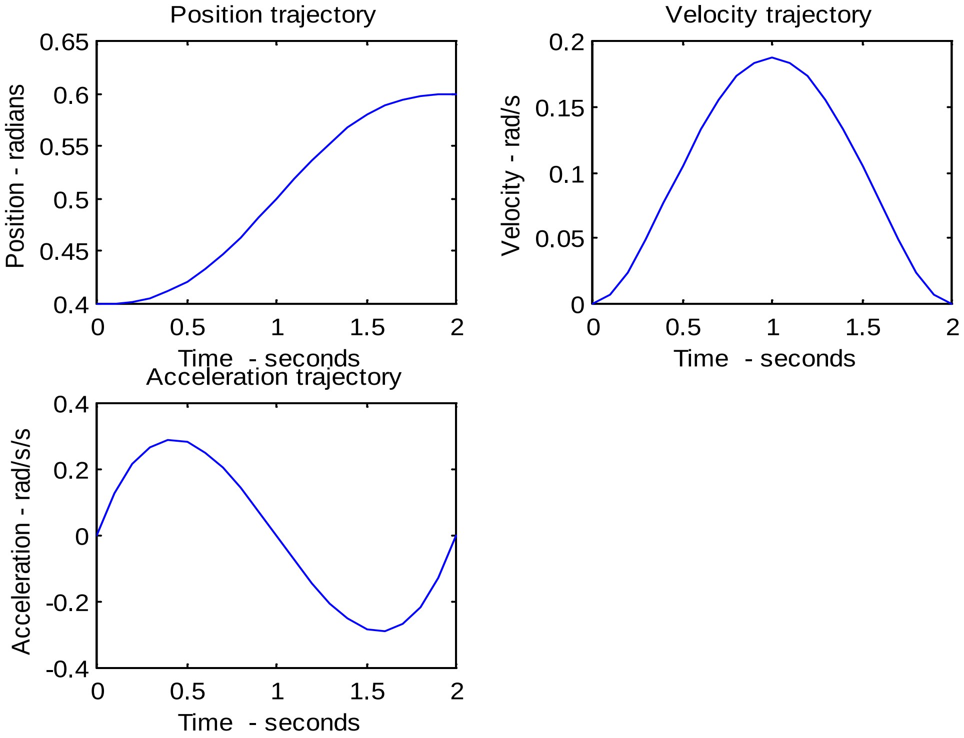

Figure 3-17 Separate position, velocity and acceleration trajectories

3.1.3 Generation of Boundary Conditions

The generation of boundary conditions is one of the fundamental time consuming pro-programming activities for a robotic system. To implement autonomous control of a thermal spraying robot manipulator will require the automatic generation of trajectories and therefore boundary conditions. The movement of the thermal spraying process is relatively slow with short start stop activity, therefore the initial and final velocity and acceleration boundary conditions will be 0 r/s and 0 r/s^2 respectively.

The initial and final positions however will be specific to the product being sprayed and therefore will have to be generated in a deterministic way based on sensory inputs so as to implement an autonomous thermal spraying robotic system. The path time will likely be a fixed quantity as small sections will be sprayed at a time.

Torch position and orientation is normally a real world co-ordinate and the input command from which actuator joint position, velocity and acceleration trajectories are required. However to convert from real world coordinates to joint space coordinates can be achieved using the robots inverse kinematic equations the subject of Chapter 4.

The generation of boundary conditions is therefore a relatively straight forward process. If transducers are used to monitor join velocity and acceleration trajectories these signals may be used to maximise process speed and maintain them within maximum joint velocity and acceleration specifications.

Trajectory planning may be used to investigate robotic system design such as the actuator load torques in particular the maximum possible inertial acceleration torques. The gravitational torques can also be analysed based on the arms angular position. system dynamics is the subject of section 3.2 .

The investigation of trajectory planning has resulted in a relatively straight forward solution to determining thermal spraying robots joints angular positions without causing discontinuities in velocity or acceleration. The autonomous generation of trajectories is also a relatively straight forward process given sensor information on real world torch tip start and stop positions. Therefore further investigation in this area is unnecessary for this research.

3.2 Robot Dynamics

3.2.1 General Robot Dynamic Model

The control of robot manipulators may be achieved by considering the robots dynamics and developing control laws to manage those equations. However the dynamic equations of a robot manipulator are particularly complex when we are considering articulated robot manipulators because they are non-linear and highly coupled. The general dynamic model of a robot manipulator is a second order differential equation with highly non-linear and coupled parameter matrix coefficients. The matrix form of the dynamic model (Schilling, 1990) of a multi joint robot manipulator is given in Equation (3-11).

$$\begin{gathered} for\ i = 1 : N\ (number\ of\ actuators) \\ \sum_{j=1}^{N} D(i,j)\ddot{\theta}_j + \sum_{j=1}^{N} C_{cent}(i,j)\dot{\theta}_j^2 + \sum_{j=1}^{N}\sum_{k=j+1}^{N} C_{cor.}(i,j,k)\dot{\theta}_j\dot{\theta}_k + h_i + b\dot{\theta}_i = \tau_i \end{gathered} \qquad \textbf{(3-11)}$$

where:

- $D(i,j)$ is an inertia tensor matrix term,
- $C_{cent}(i,j)$ is a centrifugal matrix term,
- $C_{cor}(i,j,k)$ is a coriolis matrix term,
- h_i is a gravity term,
- b is a viscous friction term and,
- τ_i is the load torque term.

This equation is significant from the point of view of the complexity of the control scheme required for a particular application. However in the case where actuators are fitted with high reduction gear ratios or processes which require limited velocity and acceleration performance then many of the torque terms in this dynamic model can be considered as a disturbance where standard control algorithms may be used (Sciavicco, 2004).

3.2.2 Thermal Spaying Robot Dynamics

The research considered the five axis robot manipulator shown in Figure 3-18 and two key process requirements high speed processing and low speed processing.

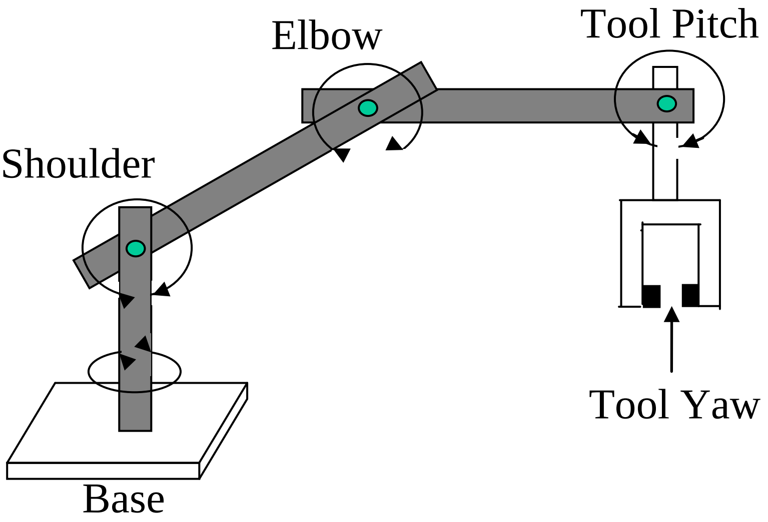

Figure 3-18 Dynamic Model Robot

High speed processing can be achieved by using low reduction gear ratios or direct drive actuators such as the Megatorque^{TM} motor and moving actuators concurrently. If we were to move the shoulder and elbow joints simultaneously this would require complete consideration of all the torque loads defined in the dynamic model, the base joint does not have a gravitational load. If a high speed robot manipulator was commanded to move the shoulder and elbow joints simultaneously the shoulder joint actuator would have to react to the load torques listed in Table 3-8.

- Inertial torques due to shoulder and elbow actuators accelerating.
- Centrifugal torques due to the elbow joint velocities
- Coriolis torques due to shoulder and elbow cross velocity terms.
- Shoulder joint gravitational torque due to robot arm position.
- Shoulder joint viscous frictional torque

Table 3-8 Load Torques

Low speed processing allows us to include high reduction gear ratio gearboxes and moving the robot links individually. Moving the links individually removes the inertial torques due to the other joints and the centrifugal and coriolis torques. Including a high reduction gear ratio gearbox with ratio N reduces the gravitational load torque by factor of N and the inertial load torque by a factor of N^2. The viscous frictional torque is also reduced by a factor of N^2 although the friction terms are usually neglected in analysis.

A robot manipulator conducting thermal spraying requires relatively low speed spraying thus reducing many of the torque loads in the full dynamic model. Thermal spraying robot control can be achieved using Joint Space Control. The dynamic model of the thermal spraying robot manipulator can be written as shown in Equation (3-12) (Sciavicco, 2004). This equation excludes static friction and end-effector forces as the thermal spraying torch does not make surface contact.

$$D(\theta)\ddot{\theta} + C(\theta,\dot{\theta})\dot{\theta} + h(\theta) + b(\dot{\theta}) = \tau \qquad \textbf{(3-12)}$$

where terms have been defined in Equation (3-11)

Equation (3-12) can be rewritten providing a motor toque dynamic model as shown in Equation (3-13)

$$\tau_m = \overline{D}(\theta)N^{-2}\ddot{\theta}_m + \Delta D(\theta)N^{-2}\ddot{\theta}_m + C(\theta,\dot{\theta})N^{-2}\dot{\theta}_m + h(\theta)N^{-1} + b_m(\dot{\theta})\,N^{-2} \qquad \textbf{(3-13)}$$

when an N reduction ratio gearbox is used

where:

- is the inertia tensor constant matrix term,
- *ΔD(θ)* is the inertia tensor configuration- dependent term,
- N is the gearbox reduction ratio
- is a centrifugal and coriolis matrix term,
- h(*θ*) is a configuration dependent gravity term,
- $_m$) is a motor viscous friction term,
- τ_m is the motor torque term.

This model is a combination of a linear decoupled system and a non linear coupled system which can be considered as a disturbance, *d*. This split of the dynamic model is show in Equation (3-14)

$$\tau_m = \overline{D}(\theta)N^{-2}\ddot{\theta}_m + b_m(\dot{\theta})\dot{\theta} + d$$

$$where\ d = \Delta D(\theta)N^{-2}\ddot{\theta}_m + C(\theta,\dot{\theta})N^{-2}\dot{\theta}_m + h(\theta)N^{-1}\ and \qquad \textbf{(3-14)}$$

$$b_m(\dot{\theta}) = b(\dot{\theta})N^{-2}$$

A block diagram for the linear decoupled model with disturbance is shown in Figure 3-19.

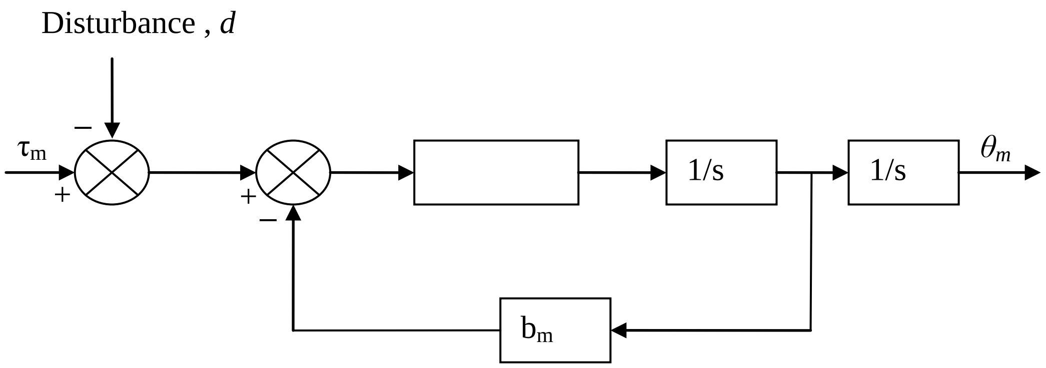

Figure 3-19 Linear Decoupled Model

3.2.3 Dynamic Model Analysis

To investigate the effects of dynamic modelling the dynamic model for a two axis planar robot manipulator was considered. This type of robot arm has only two degrees of freedom in a single plane. This may seem limiting however it constitutes the fundamental structure of the thermal spraying anthropomorphic articulated robot manipulator. The dynamic equations for this two link structure include all the torques in the dynamic model. By adding a waist axis produces the standard articulated structure. The two-axis planar robot arm is shown in Figure 3-20.

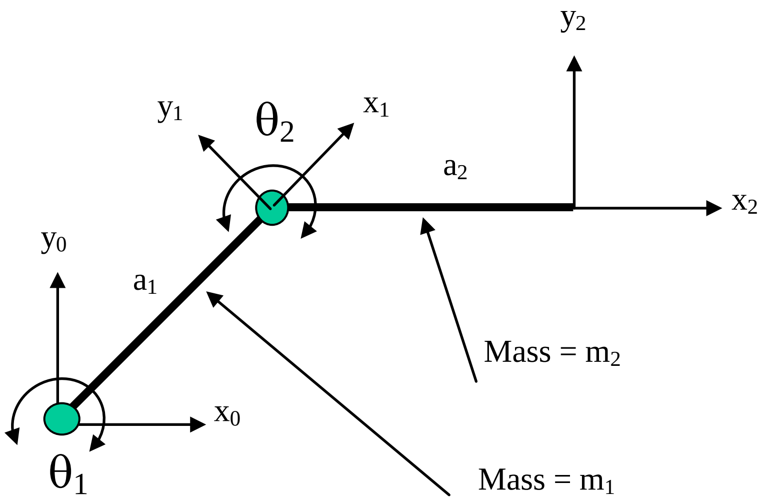

Figure 3-20 Two Axis Planer Arm

A two-axis planar robot arm driven by an electric actuator with an N ratio gearbox with links of mass m_1 and m_2 and lengths a_1 and a_2 has a set of dynamic equations of motion for each actuator (Schilling, 1990) shown in Equations (3-15) and (3-16). Viscous friction has been neglected. The equations from Schilling have been modified to include an N reduction ratio gear which can be set to one for direct drive analysis.

$$\tau_1 = \frac{D_{11}\ddot{\theta}_1}{N^2} + \frac{D_{12}\ddot{\theta}_2}{N^2} - \frac{m_2 a_1 a_2 Sin\theta_2 (\dot{\theta}_1\dot{\theta}_2 + \frac{\dot{\theta}_2^2}{2})}{N^2} + \frac{h_1}{N} \tag{3-15}$$

$$\tau_2 = \frac{D_{21}\ddot{\theta}_1}{N^2} + \frac{D_{22}\ddot{\theta}_2}{N^2} + \frac{m_2 a_1 a_2 Sin\theta_2 (\dot{\theta}_1^2)}{2N^2} + \frac{h_2}{N} \tag{3-16}$$

where :

$$D_{11} = (\frac{m_1}{3} + m_2)a_1^2 + m_2 a_1 a_2 Cos\theta_2 + m_2 a_2^2$$

$$D_{12} = D_{21} = \frac{m_2 a_1 a_2 Cos\theta_2}{2} + \frac{m_2 a_2^2}{3}$$

$$D_{22} = \frac{m_2 a_2^2}{3}$$

$$h_1 \ = g_0\left[\left(\frac{m_1}{2} + m_2\right)a_1 Cos\theta_1 + \frac{m_2 a_2 Cos(\theta_1 + \theta_2)}{2}\right]$$

$$h_2 \ = go\left(\frac{m_2 a_2 Cos(\theta_1 + \theta_2)}{2}\right)$$

A Matlab^{TM} program was developed named `dynamics.m` to investigate the affect of various trajectories, link lengths, link masses and reduction ratio gearboxes have on the load torques seen by the electric motor. The `trajectory.m` program was modified into a Matlab^{TM} function and to provide trajectory plots in a single window. This function is embedded in the `dynamics.m` program. Figure 3-21 shows the dynamics algorithm developed. The complete Matlab^{TM} program listing for the trajectory function and dynamics program is provided in Appendix B.

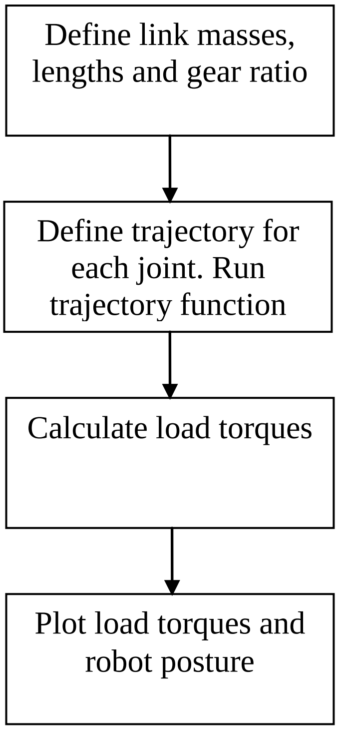

Figure 3-21 Dynamics Algorithm

For comparison purposes the dynamics program is run twice using the normalised parameters shown in Table 3-9. Once in direct drive mode i.e. gearbox ratio = 1 and once with a 10:1 gearbox ratio. The trajectory and torque curves produced for the direct drive mode are shown in Figure 3-22, Figure 3-23, Figure 3-24 Figure 3-25. Robot arm final posture is shown in Figure 3-26. Total and separate load torques using a 10:1 gearbox are shown in Figure 3-27 and Figure 3-28.

Link/joint one	length	1 m
	mass	1 kg
	initial time	0 s
	final time	1 s
	initial position	0 r
	final position	1 r
	initial velocity	0 r/s
	final velocity	0 r/s
	initial acceleration	0 r/s/s
	final acceleration	0 r/s/s
	gearbox reduction ratio	1 and 10:1
Link/joint two	length	1 m
	mass	1 kg
	initial time	0 s
	final time	1 s
	initial position	0 r
	final position	1 r
	initial velocity	0 r/s
	final velocity	0 r/s
	initial acceleration	0 r/s/s
	final acceleration	0 r/s/s
	gearbox reduction ratio	1 and 10:1

Table 3-9 Two Axis Parameters

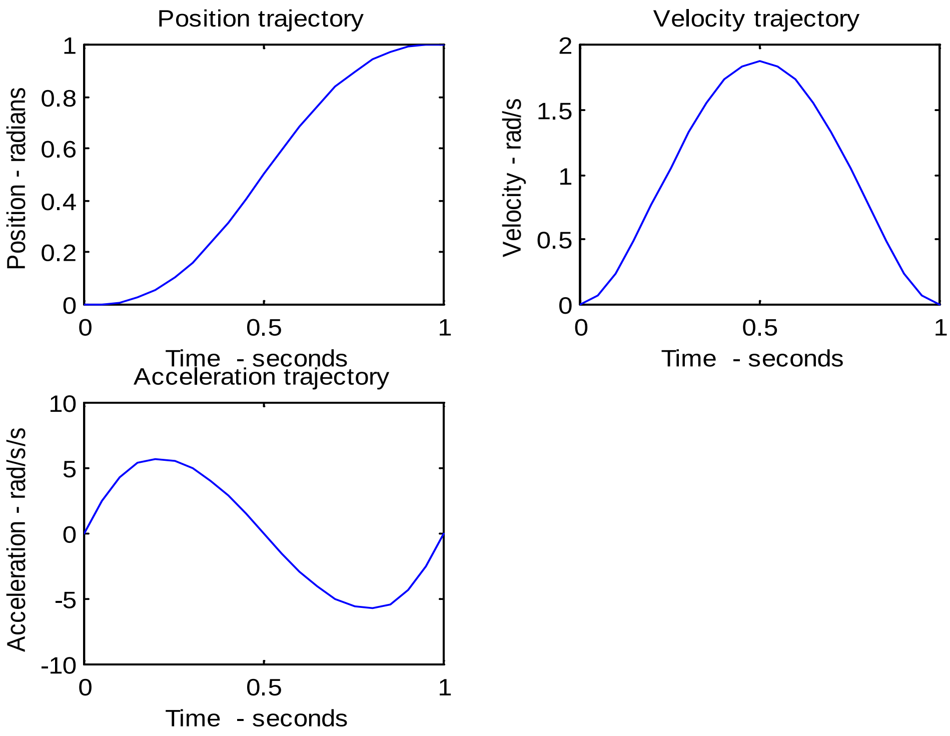

Figure 3-22 Position Velocity and Acceleration Joint One

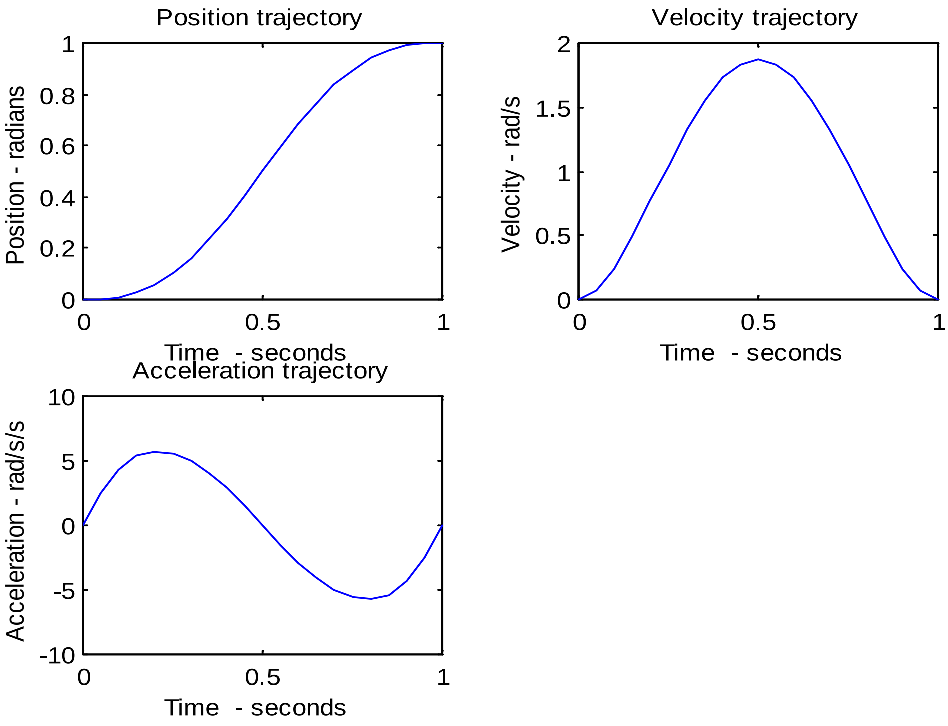

Figure 3-23 Position, Velocity and Acceleration Joint Two

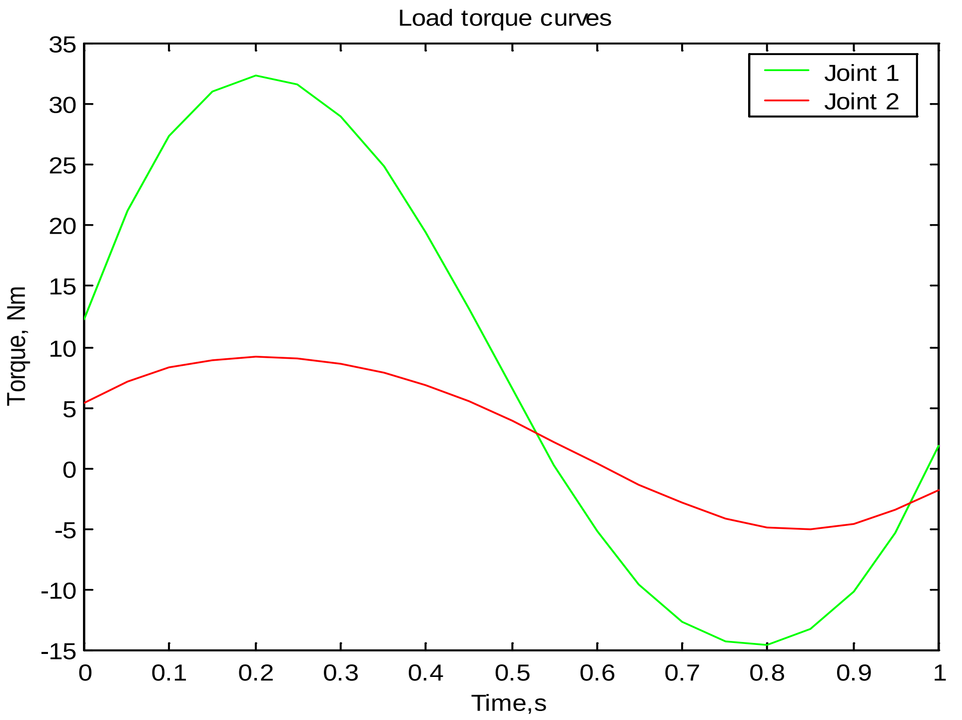

Figure 3-24 Total Load Torque Curves Direct Drive

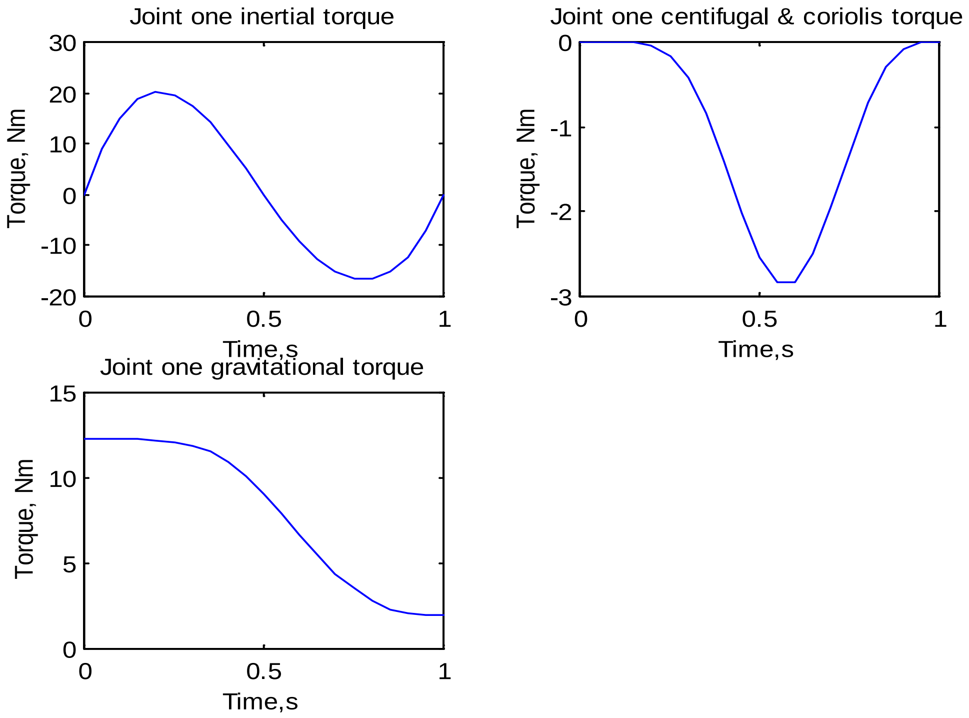

Figure 3-25 Separate Load Torques for Joint One Direct Drive

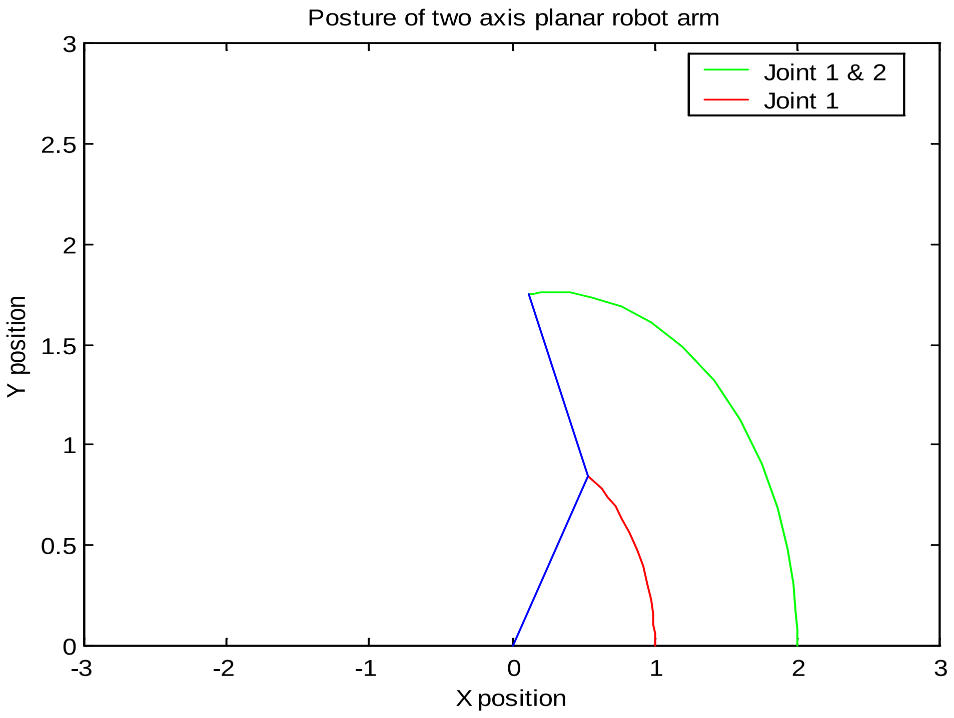

Figure 3-26 Two Axis Planer Arm Final Posture

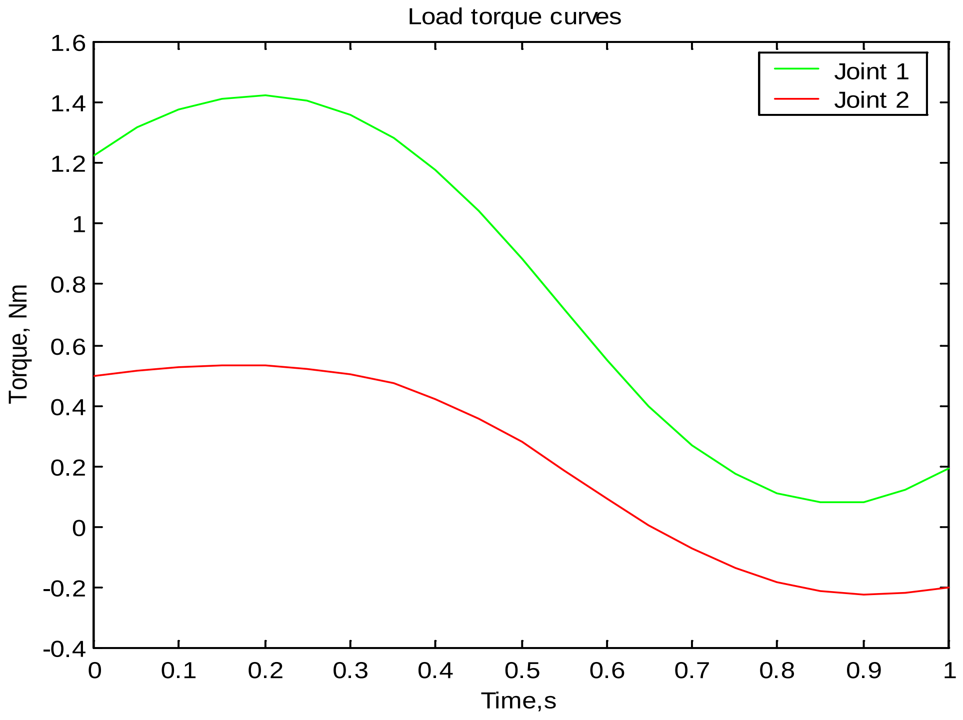

Figure 3-27 Total Load Torques 10:1

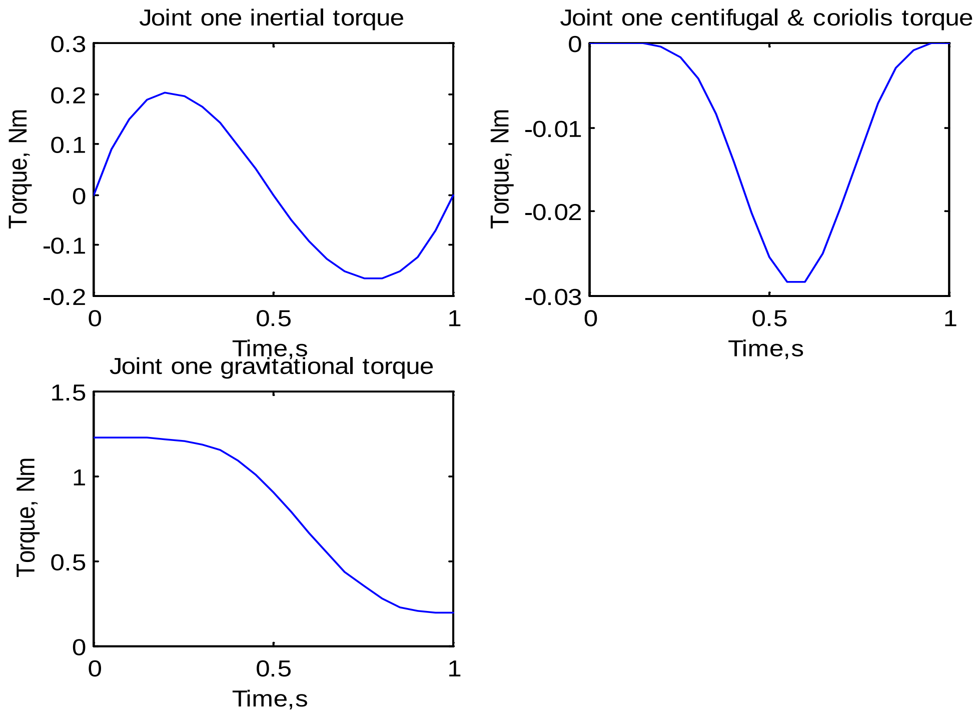

Figure 3-28 Separate Load Torques 10:1

From these results it is clear the reduction ratio gearbox has a significant bearing on the maximum load torque seen by the motor. There is a reduction from a maximum load torque of 32.3116 Nm to 1.4227 Nm. The program provides design torque loadings of a standard two axis robot manipulator.

The investigation into dynamic modelling of robot manipulators has led to the conclusion that anthropomorphic articulated thermal spraying robot manipulators can be modelled as a linear decoupled system with a non linear coupled disturbance therefore standard control system solutions can be applied. There is however a significant area of research in this area when high speed direct drive robotics is required. This is an area for further research. One such paper of interest is by (Dianqi. L, 2007).

CHAPTER 4

ROBOT KINEMATICS

4.1 Robot Arm with Continuous Rotation Kinematics

This chapter deals with the forward and inverse kinematics of an anthropomorphic articulated robot manipulator with continuous rotation waist, shoulder and elbow joints and limited rotation yaw and pitch wrist joints. Forward and inverse kinematics of standard robot manipulators is well documented in Schilling (Schilling, 1990), Sciavicco and Siciliano (Sciavicco, 2004) and Niku (Niku, 2001) and is the main source of reference material for this chapter. This chapter also deals with a solution for delivering power and control signals through the continuous rotation joints.

4.2 Robot Workspace

The workspace envelope of a robot manipulator is important from a systems design point of view. The work space envelope defines the three dimensional working volume of a particular robot manipulator. It is necessary to consider the various robot manipulator structures and choose a structure which best satisfies the needs of thermal spraying. Table 4-1 details the main set of three axis robot manipulators, each of which will place a tool in a particular location in three dimensional space (Shelton, 2008). Revolute joints cause rotary motion about an axis and prismatic (linear) joints cause linear motion along an axis.

Robot	**Axis 1**	**Axis 2**	**Axis 3**	**Application**
Cartesian	Prismatic	Prismatic	Prismatic	Pick and Place/Assembly
Cylinderical	Revolute	Prismatic	Prismatic	Spot Welding/Machine tools
Spherical	Revolute	Revolute	Prismatic	Gas and Arc Welding
SCARA	Revolute	Revolute	Prismatic	Assembly
Articulated	Revolute	Revolute	Revolute	Welding/Spray Painting
SCARA:- Selective Compliance Assembly Robot Arm				

Table 4-1 Robot classification

This research aims are to produce an autonomous version of a human arm and human sensory system, for the thermal spraying process. The articulated robot is the most anthropomorphic i.e. it closely resembles the anatomy of the human arm. In addition Table 4-1 indicates the articulated robot is used in the spray-painting and welding industry, which would be closely related to thermal spraying. Therefore the three-axis articulated robot manipulator structure was chosen as the preferred structure to develop an autonomous robot for the thermal spraying process. In addition to these three axes, a further two are required for pitch and yaw so as to point the torch tip in arbitrary approach orientations. Roll is not required, therefore saving costs.

A standard six-axis robot manipulator with limited joint movements the standard commercial structure could be specified for this research however workspace envelope research indicates that the maximum workspace envelope can be obtained from the three main joints, waist, shoulder and elbow, having no limits. This conclusion is drawn based on the main structure for a three axis articulated robot manipulator shown in Figure 4-1 a two axis planer arm with joint angles θ_1 and θ_2 and link lengths a_1 and a_2.

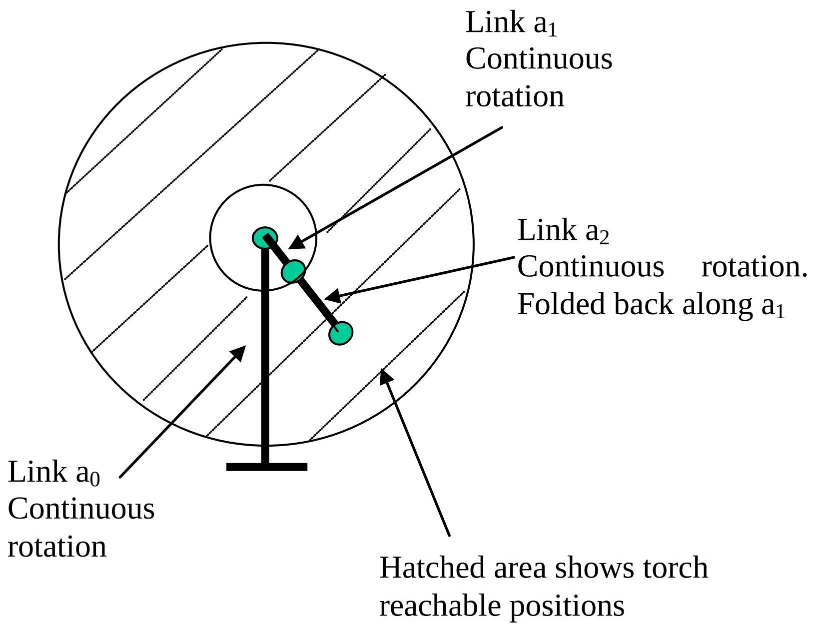

Figure 4-1 Work space envelope

Based on this concept it was decided to design the robot manipulator to have continuous rotation of the waist, shoulder and elbow joints. This will maximise workspace volume for given link lengths. It will also improve speed as there are no joint limits, i.e. full reversal will be unnecessary. The thermal spraying of the inside of a large cylindrical structure could be done by moving the robot arm axially inside the cylinder and spraying the internal surface while continuously rotating the shoulder joint. More complex shapes could also be sprayed by adjusting elbow, pitch and yaw joints assuming spray surface remained in the robots workspace envelope.

This type of design would have applications in other areas such as space exploration where compact size when not in use would be important or applications where continuous rotation efficiency is required.

4.3 Robot Tool Orientation

Tool frame with respect to a fixed reference frame is an important specification as it defines three degrees of freedom Yaw, Pitch and Roll (YPR). Consider two coincident 3 dimensional frames, a fixed frame F and a mobile frame M such that $F = \{ f^1, f^2, f^3 \}$ and $M = \{m^1, m^2, m^3 \}$. Aligning the mobile frame M to the fixed frame F with Yaw, Pitch and Roll defined as shown in Figure 4-2 provides a mechanism for managing the Yaw, Pitch and Roll of robot manipulators tool such as a thermal spraying torch.

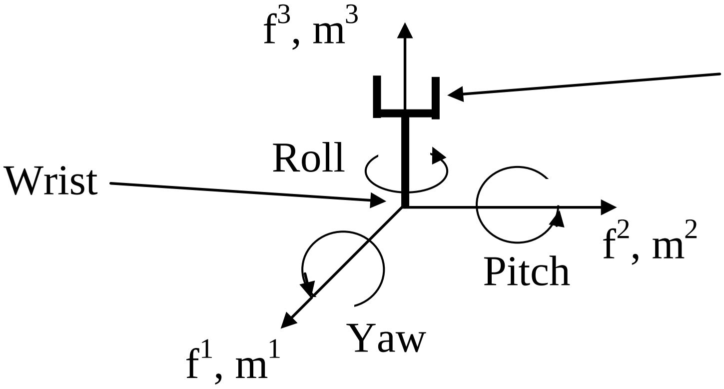

Figure 4-2 Tool Orientation

Using 3 dimensional coordinate coincident orthonormal frames and rotating the mobile frame by an angle θ_1 around the fixed frame axis f^1 as shown in Figure 4-3 coordinates of a point in the mobile frame are transformed into coordinates in the fixed frame by the equation given in Equation (4-1).

$$[p]^F = R_1(\theta_1)[p]^M \tag{4-1}$$

where:

$R_1(\theta_1)$ is given in equation (4-2)

$R_2(\theta_2)$ is given in equation (4-3) and

$R_3(\theta_3)$ is given in equation (4-4).

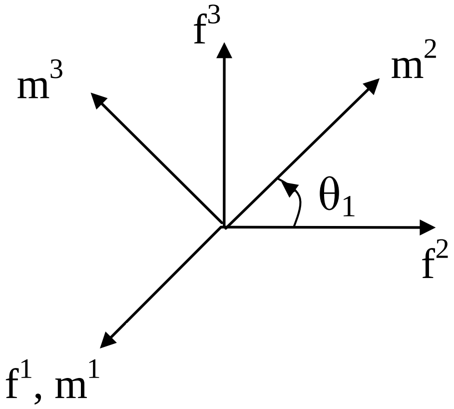

Figure 4-3 Orthonormal Frames

$$R_1(\theta_1) = \begin{bmatrix} 1 & 0 & 0 \\ 0 & \cos\theta_1 & -\sin\theta_1 \\ 0 & \sin\theta_1 & \cos\theta_1 \end{bmatrix} \tag{4-2}$$

$$R_2(\theta_2) = \begin{bmatrix} \cos\theta_2 & 0 & \sin\theta_2 \\ 0 & 1 & 0 \\ -\sin\theta_2 & 0 & \cos\theta_2 \end{bmatrix} \tag{4-3}$$

$$R_3(\theta_3) = \begin{bmatrix} \cos\theta_3 & -\sin\theta_3 & 0 \\ \sin\theta_3 & \cos\theta_3 & 0 \\ 0 & 0 & 1 \end{bmatrix} \tag{4-4}$$

Composite rotations are a combination of fundamental rotations. However it is important to carry out the rotations in an agreed sequence. For Yaw, Pitch and Roll sequence around the fixed frame vectors f^1, f^2 and f^3 , the transformation matrix for a point in the mobile frame to a point in the fixed frame is given in Equation (4-5).

$$YPR(\theta) = R_3(\theta_3)R_2(\theta_2)R_1(\theta_1) \tag{4-5}$$

Pure rotations are insufficient to characterize the position of a tool relative to a coordinate frame attached to the base of the robot as the two frames are not normally coincident. A 4 dimensional space of homogeneous coordinates are required. The 4 x 4 homogeneous transformation matrix is defined in equation (4-6).

$$Homogeneous\,transformation = \begin{bmatrix} R & p \\ \eta^T & \sigma \end{bmatrix} \tag{ 4-6}$$

where:

R is the rotation matrix,

p is the position vector,

η^T is a perspective vector for use with camera monitoring otherwise it is set to zero,

σ scaling factor typically set to one

For pure rotations the distance vector p is set to zero and for pure translations the rotation matrix R is set to its identity matrix. If a translation λ along the k^{th} unit vector is followed by a rotation along the same unit vector a screw transformation occurs given in Equation (4-7).

$$Screw(\lambda,\theta, k) \Rightarrow R(\theta, k)T(\lambda i^k) \tag{4-7}$$

In this research thermal spraying does not require the roll axis thus reducing manipulator costs. Robot manipulators are normally supplied with three degrees of freedom for waist, shoulder and elbow with the tool orientation units being supplied by third party suppliers. This research focuses on the three significant axis of waist, shoulder and elbow as these require continuous rotation functionality.

4.4 Robot Kinematics

4.4.1 Kinematic Parameters

To design a control strategy for the thermal spraying robot research of the mathematics associated with robot kinematics was conducted. Robot kinematics deals with the motion and structure of robot manipulators. There are two particular problems associated with kinematics of robot manipulators and they are:

- determining the solution of the direct kinematic problem
- determining the solution of the inverse kinematic problem.

The direct kinematic problem requires the determination of the tool position and orientation vectors (tool configuration space) with respect to a coordinate frame attached to the base of the robot arm, given the robot arm kinematic parameters (joint space).

The inverse kinematic problem requires the determination of the robot arm variable kinematic parameters given a desired set of position and orientation vectors of the robot arm tool tip. Figure 4-4 shows a graphical representation of both problems. $\boldsymbol{\theta}$ represents joint variables and in the case of a five axis articulated robot arm these are five angles. $\mathbf{p}$ and $\mathbf{R}$ represent tool position and orientation vectors.

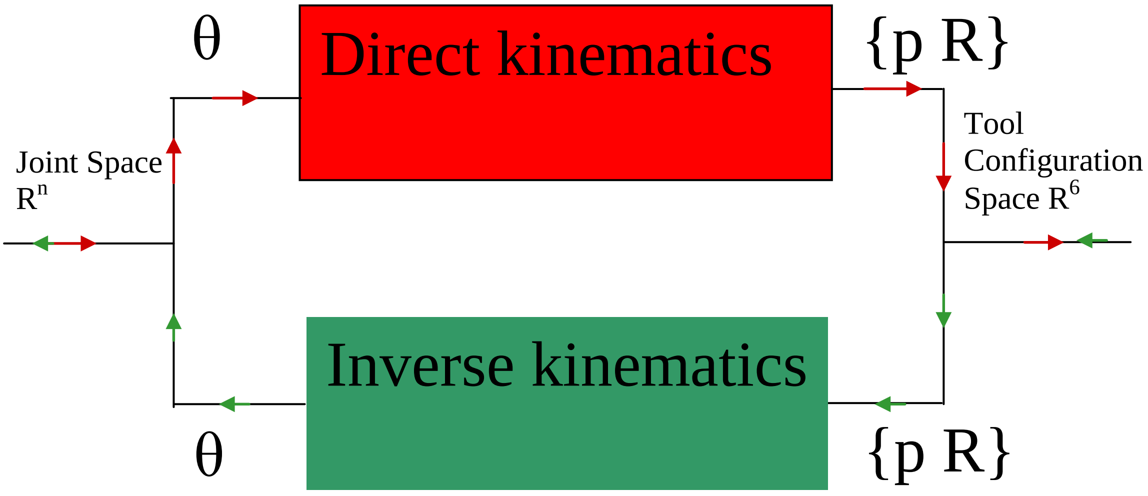

Figure 4-4 Forward and Inverse Kinematics

Kinematic parameters are the angles and lengths associated with a particular robot arm. Some of these parameters are variable and depend on the particular geometry of the robot arm. These parameters are different for each and every robot arm. However there are only four. Table 4-2 details the parameter type associated with revolute or prismatic joints.

Arm Parameter	**Symbol**	**Revolute Joint**	**Prismatic Joint**
Joint angle	θ	Variable	Fixed
Joint distance	d	Fixed	Variable
Link length	a	Fixed	Fixed
Link twist angle	α	Fixed	Fixed

Table 4-2 Kinematic Parameters

To control and manipulate a robot arm quite specific information about the robot arm is required. Denavit and Hartenberg (DH) (Denavit, 1955) developed a standard way of representing robots and modelling their motions. Examples of various standard robot manipulators are detailed by Schilling (Schilling, 1990), Niku (Niku, 2001) and

Sciavicco and Siciliano (Sciavicco, 2004). The DH algorithm provides two specific processes, which must be applied to a specific robot arm. The first process determines a set of right-handed orthonormal coordinate frames that can be applied to the robot arm links. The second process determines the robotic arm kinematic parameters.

Many sources including Schilling use standard robot manipulator structures with the links aligned in a single plane. An example of a five axis articulated robot arm is shown in Figure 4-5 to explain the D-H process. The pitch and roll axis is a common tool positioning joint as it is easily implemented using a pitch-roll spherical wrist using bevel gears.

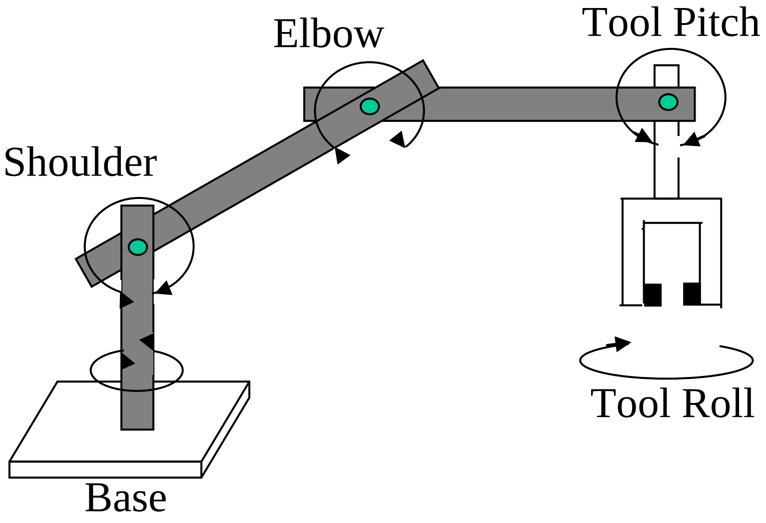

Figure 4-5 Standard 5 Axis Arm

Application of the D-H algorithm requires link coordinate frames to be assigned and if the robot arm kinematic parameters are known transformation from coordinate frame k to coordinate frame k-1 can be achieved using a homogeneous coordinate transformation matrix shown in Equation (4-8).

$A^{k}_{k-1}(\theta_k, d_k, a_k, \alpha_k) = \text{Screw}(d_k, \theta_k, 3)\text{Screw}(a_k, \alpha_k, 1)$ **(4-8)**

The overall transformation from tool to base can then be determined via equation;

${}^{R}T_H(q) = {}^{1}A_0\,(q_1){}^{2}A_1\,(q_2){}^{3}A_2\,(q_3){}^{4}A_3\,(q_4){}^{5}A_4\,(q_5)$ **(4-9)**

With a robot arm in a given position and orientation an example of which is shown in Figure 4-6 and knowing the kinematic parameters, it is feasible to determine the position and orientation of the robot tool in terms of base coordinates. This then is the solution to the direct kinematic problem; direct kinematic equations can be used to determine inverse kinematics using geometric, matrix inversion and Jacobian methods. (Sciavicco, 2004), (Niku, 2001).

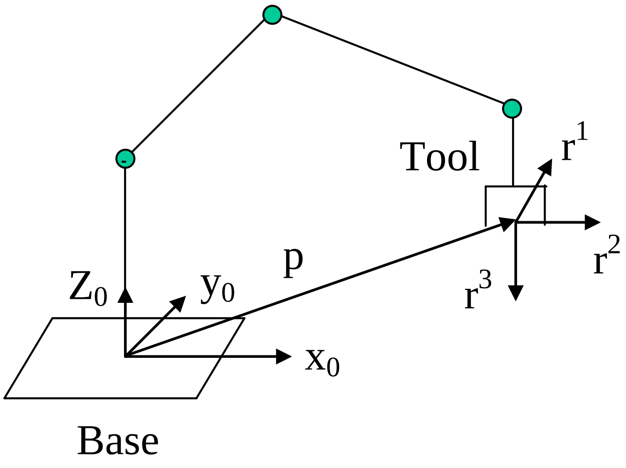

Figure 4-6 Five Axis Arm Position

Inverse Kinematics is a process of identifying joint space parameters from tool configuration parameters. This research describes the process of obtaining the forward kinematic equations using the Denavit and Hartenberg algorithm (Denavit, 1955) of a five axis robot manipulator with continuous rotation base, shoulder and elbow joints and limited angle pitch and yaw a non standard robot arm configuration. The inverse kinematics are obtained using the forward kinematic equations and a mix of geometric and inverse matrix mathematics.

4.5 Forward and Inverse Kinematics Continuous Rotation

To limit cost, a roll axis for spraying is unnecessary. Therefore the forward and inverse kinematics were developed for a five axis articulated robot manipulator with continuous rotation waist (θ_1), shoulder (θ_2) and elbow joints (θ_3) and limited rotation pitch and yaw as shown in Figure 4-7.

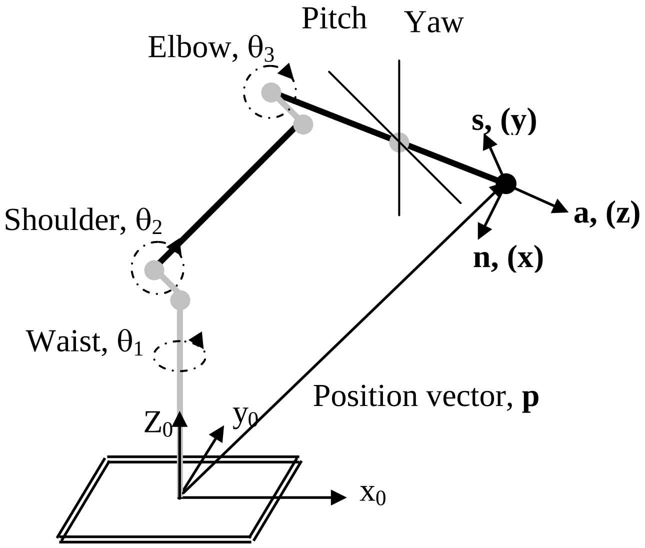

Figure 4-7 Continuous Rotation Robot Manipulator

The model in Figure 4-7 shows the location of the base frame, x_0, y_0 z_0 and the position and orientation manipulator matrix components i.e. vector p and orientation unit vectors, normal (n), sliding (s) and approach (a). Plan and elevation views of the manipulator model home position are shown in Figure 4-8 and Figure 4-9 with associated kinematic manipulator parameters.

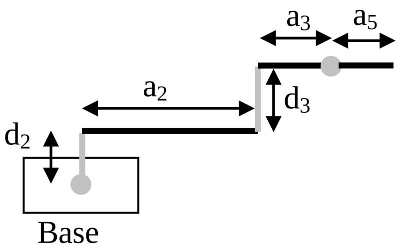

Figure 4-8 Arm Plan View

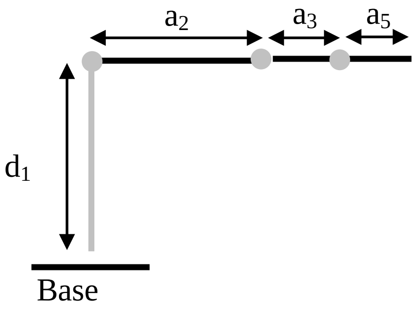

Figure 4-9 Arm Elevation View

4.6 Forward Kinematic Arm Matrix

Using the Denavit and Hartenberg method for developing the robots forward kinematics arm matrix, $^{R}T_{H}$ produces a set of highly coupled, non linear equations in θ_1 , θ_2 , θ_3 , θ_4 , θ_5 for this particular robot design. These equations can be applied to this type of robot arm with any set of kinematic parameters. Figure 4-10 shows the complete stick kinematic parameter model for the continuous rotation robot manipulator.

.

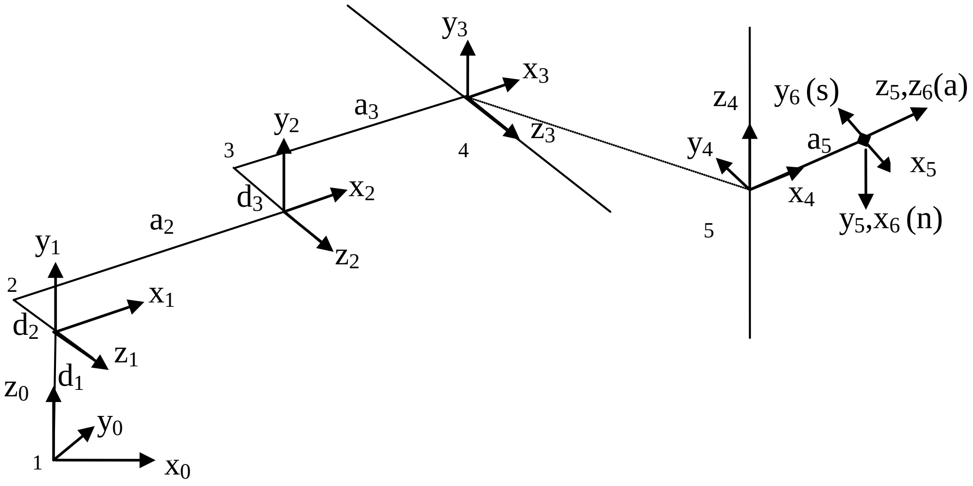

Figure 4-10 Continuous Rotation Kinematics

Application of the D-H algorithm for the 5 axis robot manipulator with continuous rotation waist, shoulder and elbow joints and limited angle pan and yaw produces the homogeneous transformation matrix equations (4-10). Multiplying these matrices together produces the robot arm matrix $^{R}T_{H}$ given in Equation (4-11) i.e. the relationship between the position and orientation of the tool and the robot base frame matrix shown in Equation (4-12).

(4-10)

$$ {}^{R}T_{H} = {}^{1}A_{0}\,{}^{2}A_{1}\,{}^{3}A_{2}\,{}^{4}A_{3}\,{}^{5}A_{4}\,{}^{6}A_{5} \quad \textbf{(4-11)} $$

$$ {}^{R}T_{H} = \begin{bmatrix} n_x & s_x & a_x & p_x \\ n_y & s_y & a_y & p_y \\ n_z & s_z & a_z & p_z \\ 0 & 0 & 0 & 1 \end{bmatrix} \quad \textbf{(4-12)} $$

where p_x, p_y, and p_z, provides the position vector of the torch tip in base co-ordinates and the unit vectors **n, s** and **a** provide the orientation of the torch tip frame in base frame co-ordinates.

The equations were developed using the Matlab^{TM} symbolic toolbox. A Matlab^{TM} algorithm to generate the forward kinematic equations and calculate the robot arm tool position and orientation in terms of joint angles is shown in Figure 4-11.

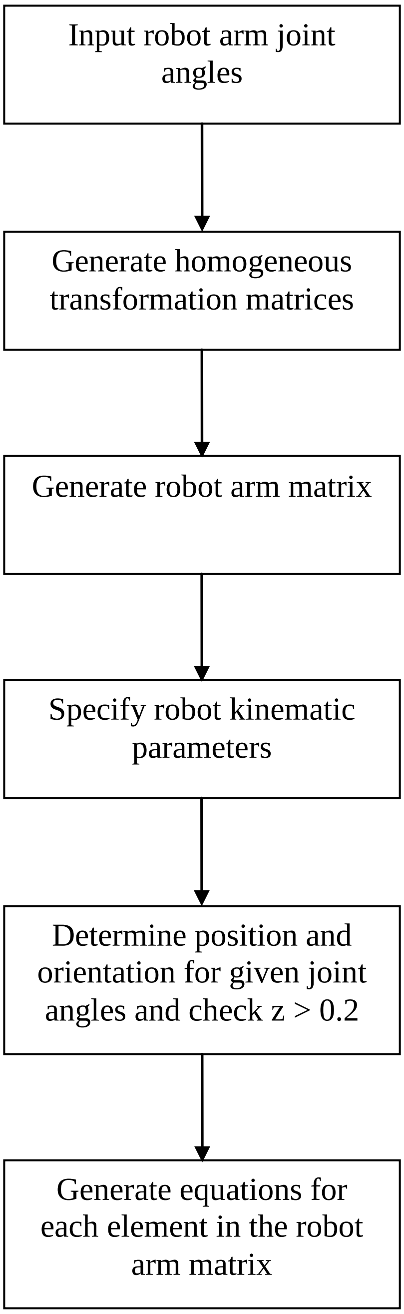

Figure 4-11 Forward Kinematic Equations Algorithm

The Matlab^{TM} program listing `forwadKinematics.m` is shown in Appendix C and the individual forward kinematic equations relating the position and orientation of the robot arm to joint angles is shown in Appendix D.

As an example of the highly non linear and coupled equations the x component of the position vector **p**, p_x is calculated from the five joint angles and the kinematic parameters using equation (4-13). The x components of the approach vector a_x is shown in equation (4-14).

p_x = 1/4*a5*cos(-theta5-theta4-theta3+theta1-theta2)+1/4*a5*cos(theta5-theta4-theta3+theta1-theta2)+1/4*a5*cos(-theta5+theta4+theta3+theta1+theta2) +1/4*a5*cos(theta5+theta4+theta3+theta1+theta2)-1/2*a5*cos(theta1-theta5)+1/2*a5*cos(theta1+theta5)+1/2*d5*sin(-theta4-theta3+theta1-theta2)-1/2*d5*sin(theta4+theta3+theta1+theta2)+1/2*a3*cos(-theta3+theta1-theta2)+1/2*a3*cos(theta3+theta1+theta2)+sin(theta1)*d3+1/2*a2*cos(theta1-theta2)+1/2*a2*cos(theta1+theta2)+sin(theta1)*d2

(4-13)

a_x = 1/4*cos(-theta5-theta4-theta3+theta1-theta2)+1/4*cos(theta5-theta4-theta3+theta1-theta2)+1/4*cos(-theta5+theta4+theta3+theta1+theta2) +1/4*cos(theta5+theta4+theta3+theta1+theta2)-1/2*cos(theta1-theta5) +1/2*cos(theta1+theta5)

(4-14)

To test these equations a physical scaled robot arm was made using Lego^{TM} and sample solutions were tested successfully against the physical model. The scaled robot arm is shown in Figure 4-12.

Figure 4-12 Physical Arm Model

The Kinematic parameters of the scaled robot arm are shown in Table 4-3.

Axis	**θ / rad.**	**d / cm**	**a /cm**	**α /rad.**	**Home/ rad**
1, waist	θ_1	15	0	π/2	0
2, shoulder	θ_2	-3	10	0	0
3, elbow	θ_3	-4	5	0	0
4, pitch	θ_4	0	0	- π/2	0
5, yaw	θ_5	0	4	π/2	0

Table 4-3 Kinematics Parameters

The home position of the robot arm is given by the vector of angles in degrees [0 0 0 0 0]. This produces the home position and orientation matrix shown in Table 4-4.

Table 4-4 Home Position Orientation Matrix for [0 0 0 0 0]

Measurement of the physical model confirms this to be the correct position and orientation matrix. Additional test results which position the robot tool tip in each of the four quadrants are shown in Table 4-5.

Input angles (degrees)	Position/Orientation (mm)	Model position
[45 90 – 90 0 0]		Correct
[90 -45 -90 0 0]		Correct
[135 -45 180 0 0]		Correct
[270 -45 135 0 0]		Correct

Table 4-5 Forward Kinematic Results

4.7 Inverse Kinematics

The inverse kinematics of the five-axis robot manipulator with continuous rotation joints is a process that will identify the five axis angles which are necessary to produce a given robot manipulator tool tip position and approach orientation vectors such as shown in Table 4-6. Because of the 5 axis limitation only columns 3 and 4 can be used to determine the inverse kinematic parameters.

-0.4200	-0.3000	-0.8600	13.4600
-0.0700	-0.9300	0.3600	-7.4500
-0.9100	0.2100	0.3700	24.5600
0	0	0	1.0000

Table 4-6 Position Orientation Matrix

There are a number of techniques for determining the inverse kinematics of robot manipulators such as, geometric, inverse matrices and Jacobean. To determine a closed form solution for the inverse kinematics for this robot arm with continuous rotation joints the techniques detailed by Schilling (Schilling, 1990), Sciavicco and Siciliano (Sciavicco, 2004) and Niku (Niku, 2001) have been combined and modified as necessary. Both geometric and inverse matrices are used.

The following are the steps in the inverse kinematic solution for the 5 axis articulated robot manipulator with continuous rotation waist (θ_1), shoulder (θ_2) and elbow (θ_3) joints and limited rotation pan (θ_4) and tilt (θ_5). It should be noted that the forward kinematic equations produce a homogeneous transformation matrix which includes the normal and sliding unit vectors n_x and s_x. However because this research has specified that roll is unnecessary, the search space for an inverse kinematic solution for the five axis robot manipulator angles is limited to the position vector **p** and the approach unit vector **a** in the homogeneous transformation matrix an example of which is given in table Table 4-7.

0	0	0.4	-10
0	0	0.3	-6
0	0	0.866	20
0	0	0	1

Table 4-7 Position Orientation Matrix with only p and a vectors

Step 1: From Figure 4-13 the wrist position vector is given by $\mathbf{p}_w = \mathbf{p} - a_5\mathbf{a}$.

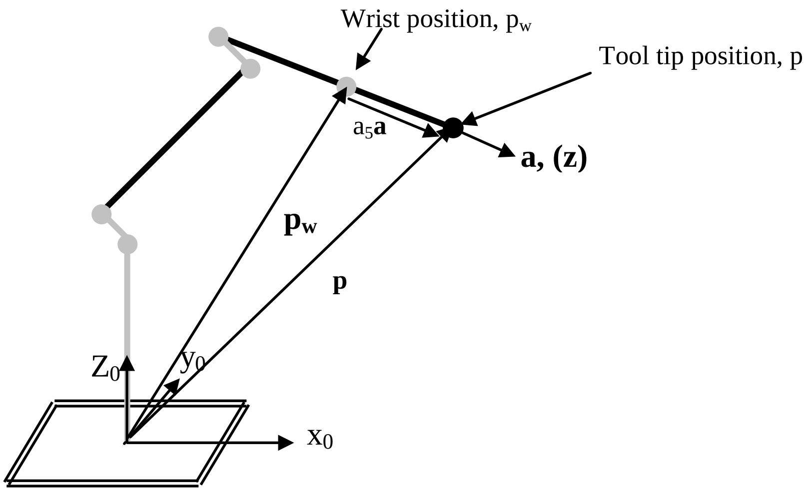

Figure 4-13 Wrist Position Vector $\mathbf{p}_w$

Step 2: The second step is to determine the waist angle θ_1. This can be obtained by considering the plan view of a general position angle θ_1 shown in

Figure 4-14.

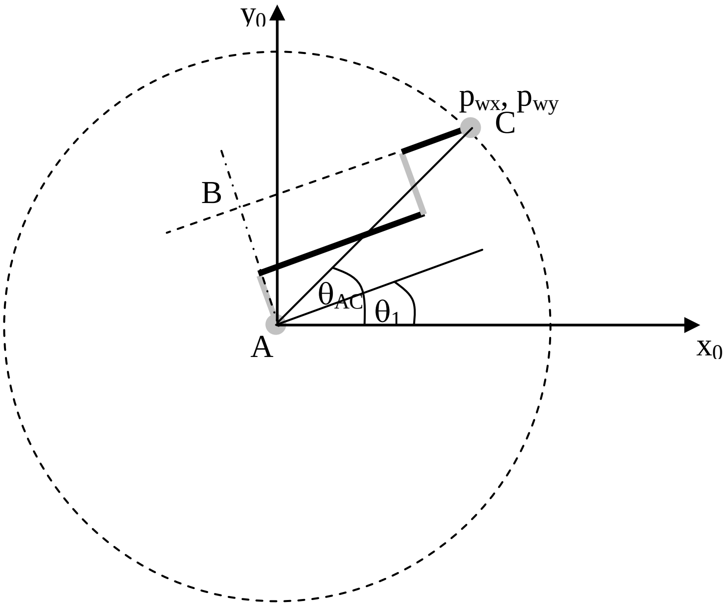

Figure 4-14 Plan View at Angle θ_1

The angle |AC| makes with the x axis can be determined from θ_{AC} = atan2(p_{wy},p_{wx}). The length |AB| = $d_2 + d_3$ (fixed quantities) therefore ∠BAC can be determined from basic trigonometry. The angle that AB makes with the x axis is ∠BAC + θ_{AC} therefore θ_1 = ∠BAC + θ_{AC} – 90 degrees. The angle θ_1 for any point on the circle shown in Figure 4-14 can be obtained with this technique as can the angle on any plan view circle within the robot arms reach.

Step 3: Once θ_1 is determined, the solution for angles θ_2 and θ_3 become solutions for a simple two axis robot arm in two dimensions as long as the p_{wx} component is the length |BC| and p_{wz} is measured from the shoulder joint as shown in Figure 4-9 (notation c_3 represents cosθ_3). The modified equations are shown in Equations (4-15) and (4-16).

$$c_3 = \frac{|BC|^2 + p_{wz}^2 - a_2^2 - a_3^2}{2a_2a_3} \tag{4-15}$$

$$s_3 = \pm\sqrt{1-c_3^2} \quad \text{angle up angle down solutions}$$

$$\theta_3 = \text{Atan2}(s_2, c_2)$$

$$s_2 = \frac{(a_2 + a_3c_3)p_{wz} - a_3s_3|BC|}{|BC|^2 + p_{wz}^2} \tag{4-16}$$

$$c_2 = \frac{(a_2 + a_3c_3)|BC| - a_3s_3p_{wz}}{|BC|^2 + p_{wz}^2}$$

$$\theta_2 = \text{Atan2}(s_2, c_2)$$

Step 4: Now that the waist, shoulder and elbow joint angles have been identified a change of approach will allow determination of the pitch and tilt angles. The forward arm matrix is made up of the multiplication of six translation and rotation matrices designated ${}^1A_0{}^2A_1$ etc. The overall matrix is given in Equation **(**4-11**)**.

The product ${}^1A_0{}^2A_1{}^3A_2$ and its inverse can now be calculated, therefore multiplying the given position and orientation matrix by the inverse of ${}^1A_0{}^2A_1{}^3A_2$ will provide a matrix, which is equal to ${}^4A_3{}^5A_4{}^6A_5$. ${}^6A_5$ is a constant known rotation. Using the Matlab^{TM} symbolic toolbox the Matrix ${}^4A_3{}^5A_4{}^6A_5$ was generated using the Matlab^{TM} program listing `wristMatrix.m` program which is provided in Appendix E. The equations generated are shown in Table 4-8

Row one [sin(theta4), -cos(theta4)*sin(theta5), cos(theta4)*cos(theta5), cos(theta4)*a5*cos(theta5)-sin(theta4)*d5]
Row two [-cos(theta4), -sin(theta4)*sin(theta5), sin(theta4)*cos(theta5), sin(theta4)*a5*cos(theta5)+cos(theta4)*d5]
Row three [0, -cos(theta5), -sin(theta5), -a5*sin(theta5)]
Row four [0, 0, 0, 1]

Table 4-8 Wrist Matrix Equations

Inspection of the coefficients of the homogeneous matrix $A_4A_5A_6$ provide a solution equation for θ_4 shown in (4-17).

$$\theta_4 = \operatorname{atan2}(a_4a_5a_6(2,3),\ a_4a_5a_6(1,3)) \tag{4-17}$$

Generating matrix A_5A_6 and inspecting the coefficients produces a solution equation θ_5.

$$\theta_5 = \operatorname{atan2}(a_5a_6(2,3),\ a_5a_6(1,3)) \tag{4-18}$$

An algorithm and Matlab™ function `inverseKinematics.m` was written which implements each of the steps outlined. To simplify the program listing the notation ${}^1A_0 = A_1$ etc. The algorithm is shown in Figure 4-15.

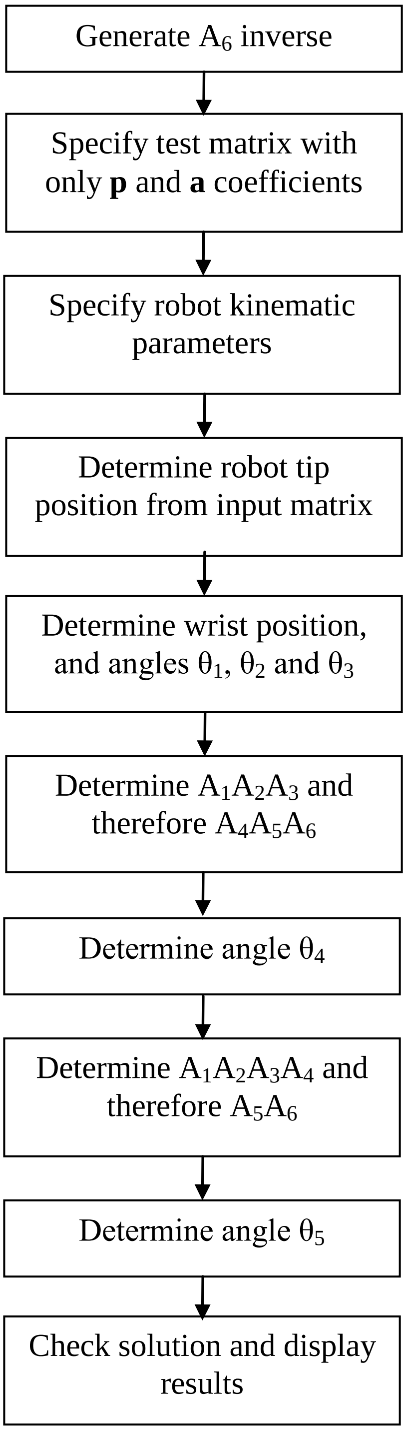

Figure 4-15 Inverse Kinematics Algorithm

The program listing is provided in Appendix F. The program has a self test in that the solution angles produced are used to generate a homogeneous transformation matrix. The position vector **p** and approach vector **a** of this matrix are compared with the input matrix. Using the example homogeneous transformation matrix given in Table 4-7 produces the calculated angles in degrees shown in Table 4-9.

θ_1 = -179.017,

θ_2 = -17.2625,

θ_3 = 81.5125,

θ_4 = 50.8186,

θ_5 = -17.0438

Table 4-9 Inverse Kinematic Angle Results

The forward kinematic equations self test confirm these results. A significant advantage of the continuous rotation joints is the travel distance/time required. As an example if the robot arm is in the home position and a call is made for the shoulder joint to rotate 260^0 the robot can move in the opposite direction by -100^0 in a shorter time. If the same time is acceptable the robot can move slower with less vibration. Safety is a key issue and must be taken into consideration with continuous rotation calls are made as the torch may hit the vertical joint. Joint position may be measured using position transducers thus assisting movement decisions.

This type of robot arm is not only suitable for thermal spraying but may have advantages for other applications such as high speed packing and product manipulation. There is also the key advantage where cabling is run through the centre of the arm thus reducing overall link cross section and risk to cable damage. The robot arm also has a longer reach for given link lengths, and will fold up to a smaller profile.

4.8 PTFE Electroless Nickel Slip Rings and Brushes

A significant problem with a robot manipulator that has continuous joint rotation is the cabling of power and signals to and from motors and transducers along the robot arm. There are many solutions to the delivery of electrical energy across rotating joints the most common being slip ring and brushes shown in Figure 4-16.

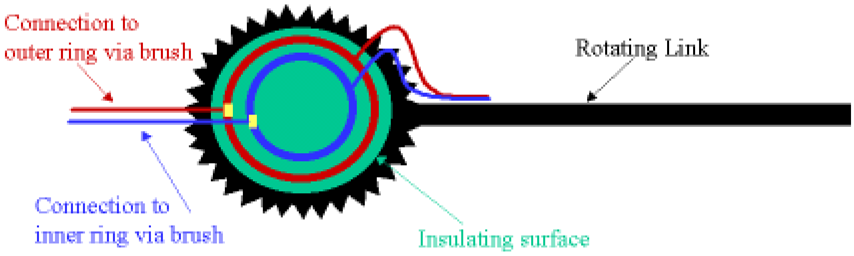

Figure 4-16 Slip Rings and Brushes

Slip rings and brushes is not a new concept, Forste and Teuschler patented a commutators and slip rings for electric machines in 1972 recommending contact material of copper, nickel or silver (Forste, et al., 1972).

Bacchi and Flipski developed a continuously rotatable multiple link robot arm mechanism (Bacchi, et al., 1997). This system relies on a mechanical mechanism to produce continuous rotation of a Selective Compliance Assembly Robot Arm (SCARA) type robot. This paper suggests using rotary fluid slip rings which may have relevance in passing the oxy-fuel through the continuous rotation joint in this research.

Gesellschaft für Antriebstechnik (Antriebstechnik, 2009) and Rotary Systems Inc. (Rotary_Systems, 2009) supply such products. They also supply electrical slip rings and brushes. Other solutions for slip rings are the use of electrical conducting fluids such as the products provided by Mercotec (Mercotac, 2009). This is a different technology to using contact based slip rings and brushes. This research has considered a solution to the weaknesses of slip rings and brushes namely wear and maintenance. Finally an interesting development is the flex gears (Peritt, et al., 1994) developed by Peritt, Tsai and Vranish. However the structure of their gear is considerably more complex than slip rings and brushes and the contact material is not Polytetrafloraethylene electroless nickel (PTFE).

Research of the thermal spraying surface coating industry highlighted the use of advanced coating materials as a solution to engineering problems. Copper slip rings and carbon brushes is a tried and tested technique for making electrical connections to rotating devices. However there are wear and maintenance issues. The design requires a material that has a low coefficient of friction thus reducing energy loss, high wear resistance and is an electrical conductor. With such a material slip rings and brushes could be made which are robust and efficient. One such material investigated for this research is Polytetrafloraethylene (PTFE) Electroless Nickel.

Table 4-10 is a mix of relevant characteristics of PTFE electroless nickel (TWR, 2009) (Surface_Technology, 2009), copper and carbon (Engineers_Handbook, 2006), (School_Science, 2009) (Winter, 2009). Gordan England provides a useful conversion calculator which converts Vickers Hardness number to the SI unit MN/m^2 (England, 2009). From this research it is clear PTFE electoless nickel has excellent conductivity, coefficient of friction and in particular hardness characteristics.

Material	**Electrical resistivity μΩcm**	**Coefficient of static friction**	**Hardness**
Carbon	35-5000	0.16 hard carbon	1-2 (Mohs)
Copper	1.7	1	37.6 (Vickers converted from MN/m^2) (3 Mohs)
PTFE electroless nickel	130-200	0.1	300 (Vickers VHN100) 550 (Vickers VHN 100)* * heat treated 250 – 300 (HK_{100}) 400 - 450 (HK_{100})* * heat treated

Table 4-10 Material characteristics

From the literature review it is clear there are many solutions to delivering electrical energy across continuously rotating joints however using PTFE electroless nickel is novel. This material is not readily available in Ireland however a surface engineering company, Hightech Plating Ltd (Hightech_Plating, 2009) does provide a standard electoless nickel plating service. This company has provided a number of electroless nickel coated copper and brass samples for test purposes.

A small electroless nickel slip ring and brushes test rig was build. The test rig demonstrated power being delivered to a rotating LED via the electroless nickel slip rings and brushes. The test rig is shown in Figure 4-17. Two electroless nickel rings were mounted on a wooden dowel. The dowel was connected to an electric motor. A light emitting diode and resistor was connected between the two slip rings. Two electroless nickel brushes were mounted against the slip rings and connected to a battery. The motor was powered up rotating the slip rings. The LED continued to work proving the fundamental concept of using PTFE electroless nickel slip rings.

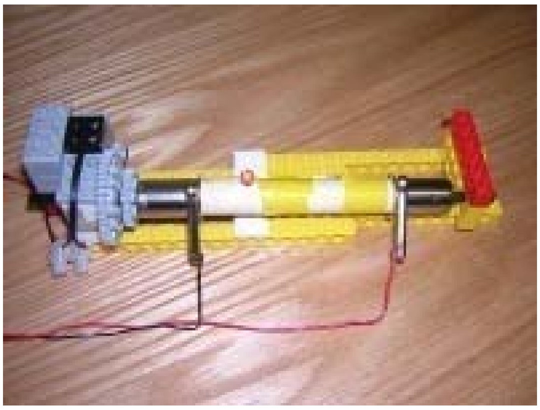

Figure 4-17 Electroless nickel slip rings

A second test was conducted where a video of the rotating slip rings was produced with the high frequency (4.433 MHz.) composite video signal being passed through the slip rings qualitatively demonstrating the slip rings ability to pass high frequency signals.

A digital Ohmmeter set at the 200 Ω setting with one decimal place accuracy registers zero ohms resistance for the electroless nickel coated copper samples.

Using the principle of the inclined plane (Halling, 1976) a simple test with the samples available was conducted to determine the coefficient of static friction. The test results are shown in Table 4-11. The results show that the coefficient of friction of copper on copper was 30% higher than electroless nickel on electroless nickel. PTFE elecroless nickel has even lower coefficient of friction than electroless nickel.

Copper on Copper Degrees	Electroless Nickel on Electroless Nickel Degrees
20	12
20	12
15	12
17	15
20	16
18	13
18	12
19	16
19	12
20	12
Average angle $\theta = 18.6^0$ Coefficient of friction $\mu = \tan\theta = .3365$	Average angle $\theta = 13.2^0$ Coefficient of friction $\mu = \tan\theta = .2345$

Table 4-11 Inclined Plane Friction Test Results

CHAPTER 5

SUBSTRATE ORIENTATION AND MEASUREMENT

5.1 Depth Measurement Techniques

Depth measurement can be achieved with a number of technologies such as infra red (Sharp), ultra sonic (MaxBotix, 2009), and laser (Hokuyo, 2009). Stereoscopic vision systems can also be used to determine depth (Marshall, et al., 1992), (Point Grey Research Inc., 2009). Early research by Higashimoto uses ultrasonic sensors to measure depth for the orientation robot control of a plasma thermal spraying torch (Higashimoto, et al., 1993) and nine years later his colleague uses two 600 nm lasers (Watanabe, et al., 2004). However none of these systems have the advantage vision systems provide such as information on object location, orientation and shape.

5.2 Image Processing and Analysis

The approach in this research is to develop a low cost vision system where depth can be measured and additional image processing and analysis can be conducted with the one low cost camera system. There are a number of image processing and analysis programming languages such as Java, C/C++ and Matlab^{TM}. Following a review of these languages it was decided to use a proprietary java based image processing and analysis package called Neatvison (Whelan, et al., 2001) for the initial investigations because of familiarity with the package. This developed into using the Matlab^{TM} Image Processing and Analysis toolbox (MathWorks, 2010).

5.3 Substrate Orientation and Measurement

In a manual thermal spraying process the operator would move the torch and vary the control distance and perpendicularity via eye hand coordination. An automatic robotic system would require detailed information on substrate shape, position and orientation before time consuming and costly preprogramming (Zieris, et al., 2004). Much of the research associated with improving the efficiency of robotic systems in thermal spraying applications is directed towards improving preprogramming and simulation techniques (Moody, 2008), (Candel, et al., 2006), (Zieris, et al., 2004), (Hansbo, et al., 2000) and (Rastegar, et al., 1995).

The fitting of a low-cost transducer to the torch to enable measurement of substrate distance from the torch tip and substrate shape, position and orientation, would substantially reduce set-up times, as different substrates can be presented to the robotic system without the need to reprogram. A significant advantage would be achieved if different materials could also be presented such as steel, brass or aluminum without the need for manual reprogramming.

The substrate surface for coating is assumed to be in the robots workspace but has varying thickness, shape and material with different reflectivity. The objective is to identify the substrates three real world coordinates X ,Y, and Z in terms of the camera charged coupled device (CCD) coordinate frame which is attached to the robot and therefore can be referenced to the robots base frame via kinematic equations. Movement of the robot across the substrate can produce a vector of real world 3D coordinates.

5.4 Research Approach and Development

This research proposes fitting a standard composite video monochrome camera, ultraviolet (UV) laser source, ultraviolet filter and ultraviolet lighting to a thermal spraying robot arm for depth measurement and object analysis.

For test purposes depth measurement was conducted using a low cost monochrome camera and infrared laser pointer which were the facilities available. However similar results would be expected using a UV laser source. Figure 5-1 shows the layout of such a system.

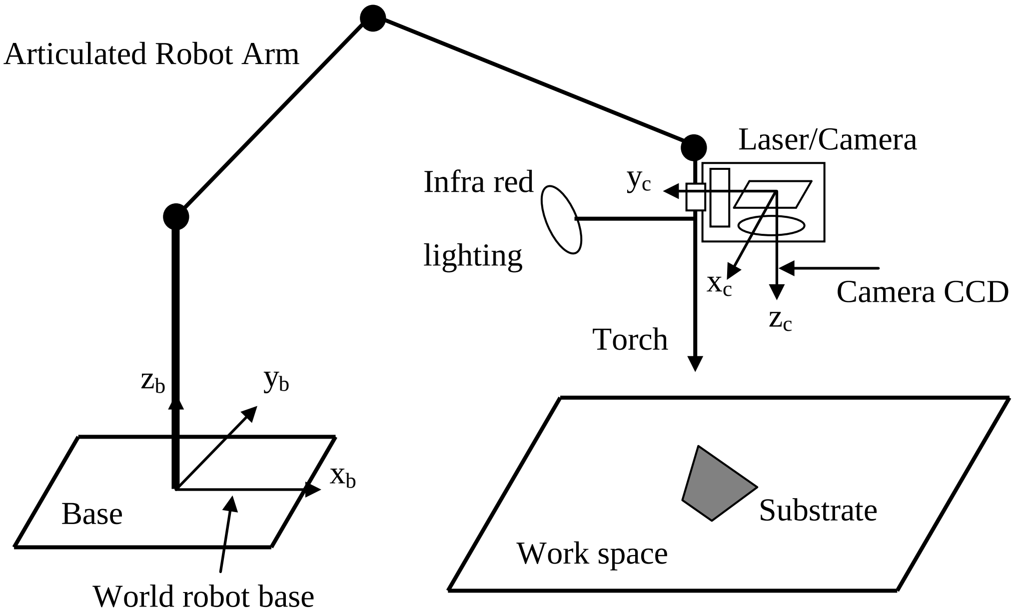

Figure 5-1 Thermal Spraying Robot Control Transducer

By physically attaching the camera CCD coordinate frame to the robot arm and hence moving with the robot arm, coordinates in this frame can be converted to coordinates in the robot's base frame using standard techniques such as Denavit-

Hartenberg (Denavit, 1955) for any robot arm position. Identifying substrate X, Y, and Z coordinates in terms of the camera CCD frame is now addressed. Once the X, Y, and Z points on the object are measured the robots inverse kinematic equations can be used to servo the robot actuators to the desired locations for spraying. This measurement can be made during the pre heating phase of the thermal praying process significantly increasing productivity. Moving the robot arm over a small horizontal section and making a grid of depth measurements as shown in Figure 5-2 produces a 3D image of that area and therefore providing the perpendicular approach vector.

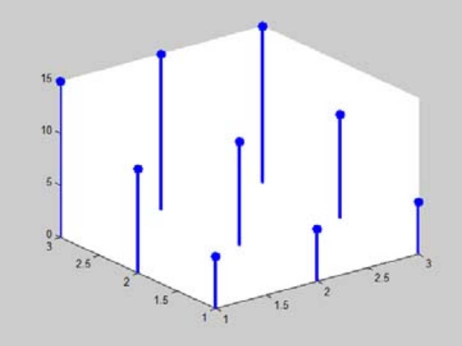

Figure 5-2 3D Depth Measurement

The thermal spraying process is considerably harsh from an optical environment perspective; therefore this research has concentrated on developing techniques in a single wavelength lighting environment. The technique is based on lighting in a single wavelength and using band-pass optical filters. From research on the spectrum of the thermal spraying process, the recommended lighting environment will be in the ultra violet spectrum. However depth measurement tests have been carried out with an infrared pointer due to availability of equipment.

Figure 5-3 shows the relationship between a charged coupled device (CCD) monochrome camera and a point on an object perpendicular to the camera view created by a laser beam parallel to the camera's optical axis. If the substrate is curved the distance will be to a tangent to the surface at the point.

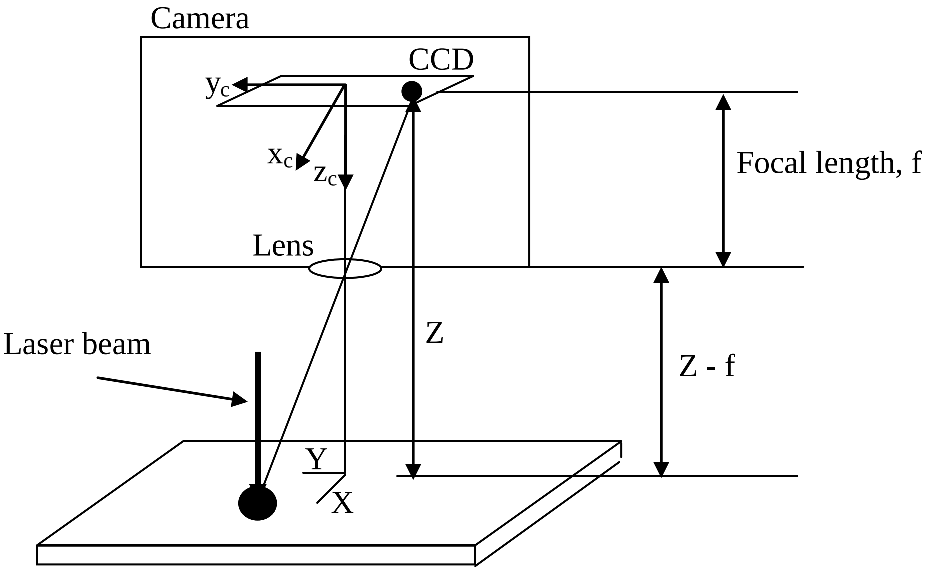

Figure 5-3 Camera Laser Point on Object

The relationship between image coordinates x, y and z and object coordinates X, Y and Z with respect to the camera frame is given by the inverse perspective transformation (Schilling, 1990) shown in Equation (**5-1**). Multiplying by the image matrix p^{image} produces the object coordinates $[p_1^{object}, p_2^{object}, p_3^{object}, 1]$.

$$p^{object} = T^{image}_{object}(Z)\,p^{image} = \begin{bmatrix} 1 & 0 & 0 & 0 \\ 0 & 1 & 0 & 0 \\ 0 & 0 & f & \dfrac{fZ}{f-Z} \\ 0 & 0 & 1 & \dfrac{f}{f-Z} \end{bmatrix} \begin{bmatrix} p_1^{image} \\ p_2^{image} \\ 0 \\ 1 \end{bmatrix} \quad \textbf{(5-1)}$$

The outcome here is to determine three-dimensional information from two-dimensional information in the inverse perspective transformation, depth coordinate Z must be known to determine object point X and Y coordinates from its image coordinates. There are several distance measuring technologies that could be used to determine the Z coordinate, such as ultrasonic, laser/infrared, or stereoscopic vision.

The technique described here uses the actual inverse perspective equations for measuring the Z coordinate. A rig was set up with the CCD camera and a 650 nm-680 nm IR laser pointer located side by side. The optical axis and laser beam were manually adjusted until both were parallel, thus the X coordinate of the laser point on an object was fixed for all Z distances. It is assumed that the surfaces being measured produce diffuse reflections. The laser point distance and thus object distance can be determined from its image coordinates using Equation (**5-2**) which is derived from similar triangles, as shown in Figure 5-4.

$$\frac{|n\Delta x|}{f} = \frac{|X|}{Z-f} \qquad \textbf{(5-2)}$$

where: n is the number of x direction pixels,

Δx is the height of the CCD pixel in m,

f is the camera focal length in m,

X is the distance between the parallel laser beam and the cameras optical axis in m and

Z is the distance to laser beam point in m, i.e. the distance to the substrate.

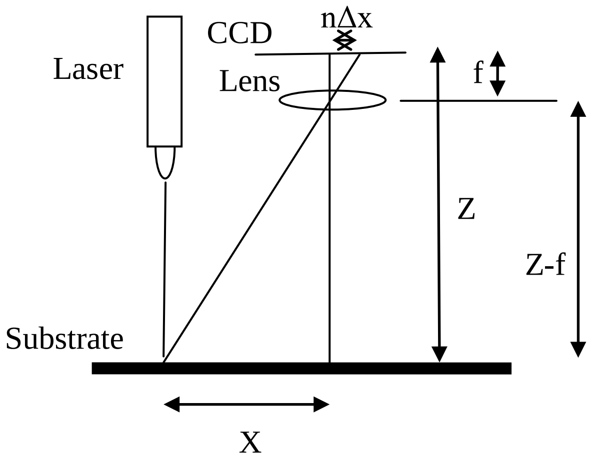

Figure 5-4 Depth Measurement Triangles

Measurements are made in the vertical direction for the following reasons. Pixels in an interline transfer chip are side by side in the vertical direction, whereas pixels in the horizontal direction are separated by charge transfer lines and are therefore further apart. Spatial frequency response of the CCD pixel is a function of the pixel capture profile (Corke, 1994). Corke in his PhD research suggests that in an interline transfer CCD, the vertical charge transfer lines reduces pixel width in the horizontal direction with corresponding improved spatial frequency response. However the camera used in this research has a horizontal pixel width of 9.8 μm and a 6.3 μm pixel width in the vertical direction, therefore for this application higher spatial frequency response will be achieved in the vertical direction.

In this application the camera used is a Samsung 1/3” 5.5 mm pinhole lens board camera whose image sensor has the spectral response (Samsung, 2009) shown in Figure 5-5. It is clear the spectral response at 650 nm is poor. However this research shows that usable images can be obtained at these wavelengths.

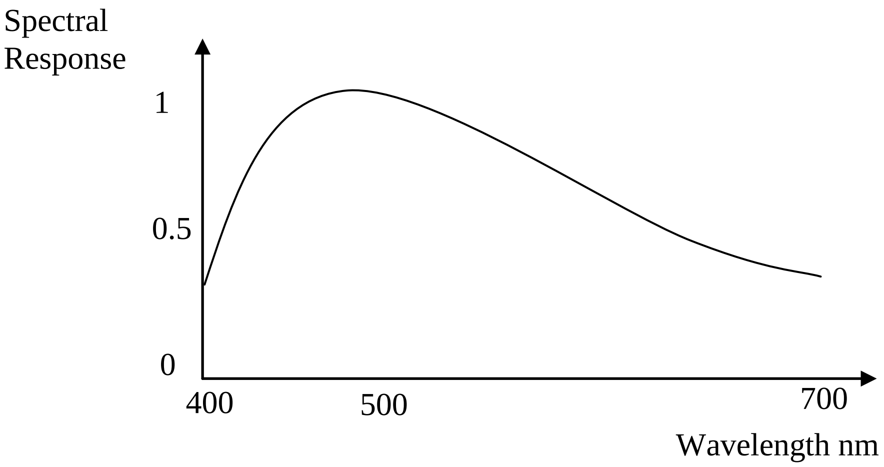

Figure 5-5 Camera Spectral Response

Accurate determination of the distance from the origin of the CCD chip frame and the centroid of the laser beam point image is a complex issue as the transfer of the actual laser point image to a digital image for analysis, shown in Figure 5-6, goes through many processing steps. The white spot in Figure 5-6 is 4 – 5 mm in diameter.

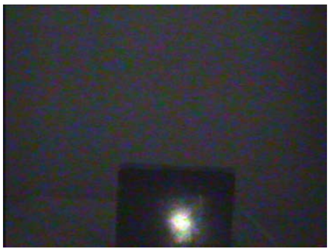

Figure 5-6 Laser / Matt Steel Image

The stages of transferring an image to its digital image representation for processing are shown in Figure 5-7.

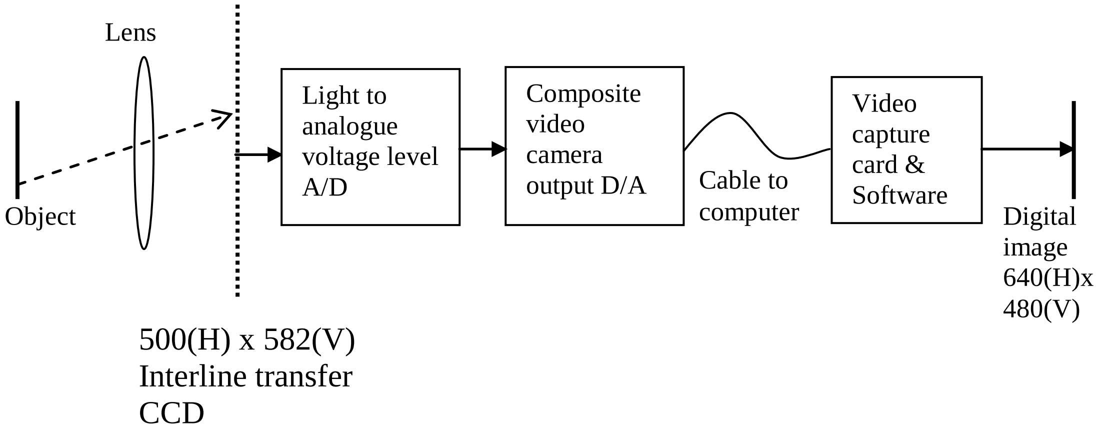

Figure 5-7 Image Transfer Stages

Detailed analysis of the effects at each stage will not be considered in this research but would provide opportunities for follow up research; therefore manufacturer's specifications and standards will be used in the calculations. Camera intrinsic and extrinsic parameters can be determined from camera calibration techniques, which attempt to correct errors in camera parameters such as lens quality, focal length and camera position, This area would provide follow up research/project activity especially considering the fact that modern CCD cameras with proper calibration are capable of sub pixel spatial accuracy. The measurement parameters are shown in Table 5-1.

X = 52 mm , Laser camera separation

f = 5.5 mm, Camera lens focal length

n = number of pixels from image center to centroid of laser beam spot

$\Delta x = 7.63875\ \mu m$, estimate of pixel size in the vertical, x, direction following conversion of CCD pixels 500 x 582 to digital image samples of 640 x 480.

Table 5-1 Depth Measurement Parameters

The algorithm developed to determine the number of pixels from the image center to the centroid of the laser beam uses a number of image processing techniques in combination. In particular opening, closing, thresholding and centroid calculation are used as shown in Figure 5-8 using Neatvison (Whelan, et al., 2001), a Java code based open source image processing and analysis suite of tools**.** GIMP (GIMP, 2009), an open source image processing software suite, was also used for preliminary image analysis and processing. The (p+q)th order moments of a digitized binary image is given by Equation (5-3) (Corke, 1994). m_{00} is the total mass of the region and (5-4) represents the centroid of the region.

$$m_{pq} = \sum \sum_{R} x^p y^q I(x,y) \tag{5-3}$$

$$x_c = \frac{m_{10}}{m_{00}}, \qquad y_c = \frac{m_{01}}{m_{00}} \tag{5-4}$$

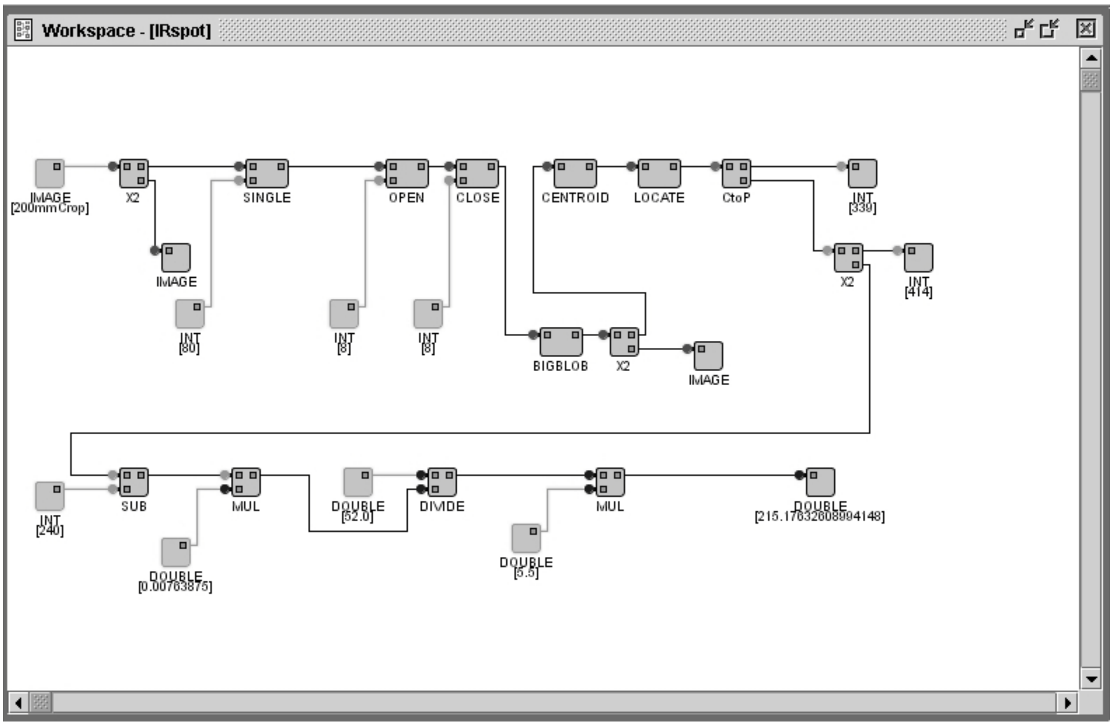

Figure 5-8 Neatvision Centroid Algorithm

5.4.1 Steel Substrate Test and Results

Table 5-2 lists results for seven measurements from 170 mm – 230 mm using a steel matt black square substrate and a fixed threshold value of 80 for all measurements.

Position	**Distance from lens mm**	**Measured distance Mm**	**Error / mm**	**% error**
1	170	187.20	17.20	10.12
2	180	195.00	15.00	8.33
3	190	205.72	15.75	8.27
4	200	215.17	15.17	7.59
5	210	225.55	15.55	7.4
6	220	236.96	16.96	7.7
7	230	247.95	17.95	7.8
Average Error			16.23	8.17

Table 5-2 Matt Black Steel Distance Measurement

The measured distance ranged from 187.2 mm – 247.95 mm. The error ranged from 15 mm – 17.95 mm or 8.33 % - 10.12 %. However the error is positive and the calculated average error of 8.17 % acts as a d.c. bias. Including the subtraction of this value from measurements will provide a more accurate measurement. To check consistency, Table 5-3 lists measurements made at a fixed distance of 200 mm. A calibration correction factor of 8.17 % has been included in the measurement algorithm. With this correction factor, measurements are made with the largest error being – 1.7 mm which is a ±0.6% accuracy, the positive error is not as much 0.03 % so further adjustment could be made. The substrate used was matt black steel finish.

Measurement / mm	Error / mm	% error
198.83	-1.17	-0.59
198.83	-1.17	-0.59
198.83	-1.17	-0.59
200.06	0.06	0.03
198.83	-1.17	-0.59
199.43	-0.57	-0.29

Table 5-3 Fixed 200mm Distance with 8.17% correction (black steel)

5.4.2 Brass Substrate Test and Results

The equipment and algorithm was tested at a fixed distance of 200 mm using a brass substrate, a material with a significantly higher reflectivity to the previous test substrate. The higher reflectivity can be seen from the laser / brass substrate image shown in Figure 5-9.

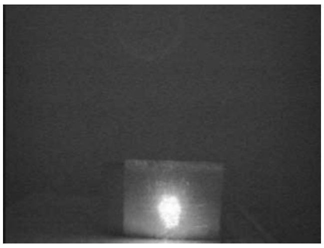

Figure 5-9 Laser Brass Substrate Image

Running the algorithm with a threshold of 80 produces a distance measurement of 228.29 mm and an error of 14.15% which is significantly higher than in previous tests. However adjusting the threshold to 190, produces the results shown in Table 5-4 which are equivalent to tests on the matt black steel. The table shows five tests at the same 200 mm range. The error ranged from 15.17 mm – 16.4 mm or 7.95 % - 8.2%. This positive error could be allowed for to improve accuracy.

Position	Distance from lens mm	Measured distance mm	Error / mm	% error
1	200	215.17	15.17	7.59
2	200	216.40	16.40	8.20
3	200	215.17	15.17	7.59
4	200	215.18	15.18	7.59
5	200	215.17	15.17	7.59

Table 5-4 Fixed 200mm Distance (brass)

5.4.3 Aluminium Substrate Test and Results

The equipment and algorithm was tested at a fixed distance of 200 mm using an aluminium substrate, a material which again has a significantly higher reflectivity to the matt black steel as can been seen from the laser / aluminium substrate image shown in Figure 5-10.

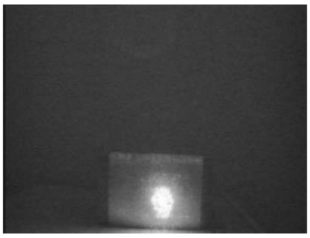

Figure 5-10 Laser Aluminium Substrate Image

Running the algorithm with a threshold of 80 produces a distance measurement of 232 mm and an error of 16% which is significantly higher than previous tests. However by adjusting the threshold to 190 it produces results shown in Table 5-5 which are equivalent to tests on the matt black steel. The table shows five tests at the same 200 mm range. The error ranged from 13.95 mm – 16.4 mm or 6.98 % - 8.2%. This positive error could be allowed for to improve accuracy.

Position	Distance from lens mm	Measured distance mm	Error / mm	% error
1	200	213.95	13.95	6.98
2	200	215.17	15.17	7.55
3	200	215.17	15.17	7.55
4	200	215.17	15.17	7.55
5	200	216.40	16.40	8.20

Table 5-5 Fixed 200mm Distance (aluminium)

5.5 Object Measurement Under 940 nm Infrared Lighting

The next phase of this research was to investigate the possibility of extracting object parameters such as area, perimeter, shape and centroid location using a standard monochrome camera and applying single wavelength light source. The light source used in this investigation comprised seven 940 nm infra red light emitting diodes. Figure 5-11 shows the image of a matt black square steel plate under 940 nm infrared lighting at a distance of 230 mm from the camera lens. Using the measured distance of 247.95 provides pixel world sizes of 0.336 mm(V) x 0.337 mm (H).

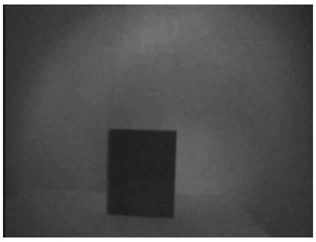

Figure 5-11 Mat Black Steel under 940 nm IR Lighting

An algorithm has been developed in Neatvision, shown in Figure 5-12 to extract useful information from the image such as object shape, area, perimeter and centroid.

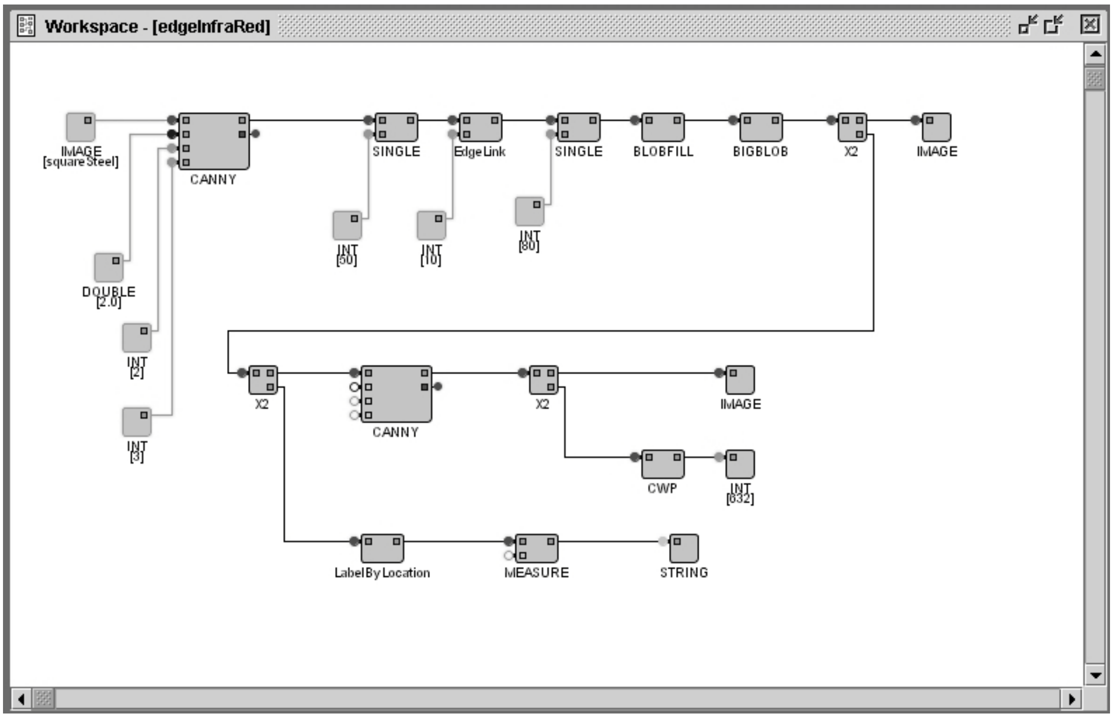

Figure 5-12 Neatvision Algorithm to Extract Object Parameters

The most significant element of this algorithm is the canny edge detection block. Although computationally expensive (Marshall, et al., 1992) it is designed to optimize the tradeoff between the two performance criteria of good edge detection and localization. Figure 5-13 shows output image extracted for parameter analysis.

Figure 5-13 Object Extracted for Parameter Analysis

The area measurement of 25268 pixels equates to an area of 2861.14 mm^2 against an actual area of 3087 mm^2, a –7.32 % error. The centroid in image pixels is located at 285 x 346. Figure 5-14 is an image of the matt black object perimeter for length measurement. This is an inverse image for printing purposes; it is normally a white line on a black background.

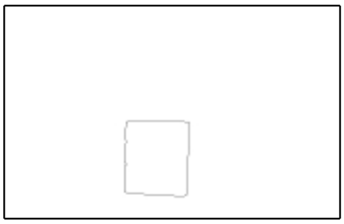

Figure 5-14 Matt Black Object Perimeter

The perimeter measurement of 632 pixels equates to a perimeter length of 212.35 mm against an actual perimeter length of 224 mm a – 5.2 % error. These results confirm the effectiveness of image processing and analysis under single wavelength lighting with low cost camera equipment.

As the contrast between the object and the background decreases, as shown in Figure 5-15, more complex algorithms will be required, although the canny edge detection algorithm does impact well in extracting the object edges as shown in Figure 5-16.

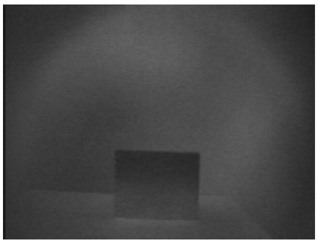

Figure 5-15 Low Contrast Image

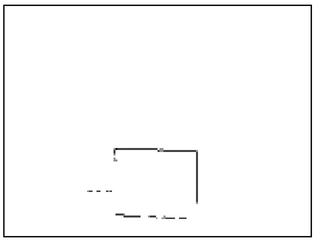

Figure 5-16 Canny Edge Detection on Low Contrast Image

The research shows that the servoing of a thermal spraying robot manipulator is feasible under single wavelength lighting. The results show that without expensive equipment or complex calibration the system investigated so far can achieve depth measurements to within ±0.6 % and that information on object parameters such as area and perimeter can be determined to within ±8% in a single wavelength lighting environment.

Research change over to the investigation of the use of Ultra Violet Lighting and image processing and analysis. The reason is that the main thrust of this research is to determine if the harsh environment of thermal spraying can be removed from the imaging system where standard and advanced image processing and analysis techniques can be used to provide control signaling for the thermal spraying manipulator.

Research on object recognition and localization in low contrast images is an area for further research.

CHAPTER 6

THERMAL SPRAYING VISION SYSTEM

6.1 Ultra Violet Spectrum Analysis

6.1.1 Camera Spectral Response

During the investigation of measuring the distance to objects with a low cost infra red laser and monochrome camera the problem of the thermal flame became a key issue. It was decided to investigate the use of a monochromatic light source and band pass filter to remove the thermal spraying flame. It was decided to use the UV-A spectrum (350 nm - 400 nm) for this research because it is reasonable to assume there is the full visible normal lighting (400 nm – 750 nm) and infra red (750 nm – 1 mm) in the thermal spraying scene and environment. The light source used was a black light fluorescent lamp which produces small amounts of 387 nm wavelength light which matches the UV band pass filter available.

A key aspect of the research was to use standard low cost equipment. The first objective was to ensure that the low cost monochrome camera has a response under ultra violet lighting, as the data sheet did not even provide data below 400 nm (Samsung). A 387 nm narrow band pass filter was used. Figure 6-1 shows the camera and filters relative spectral responses.

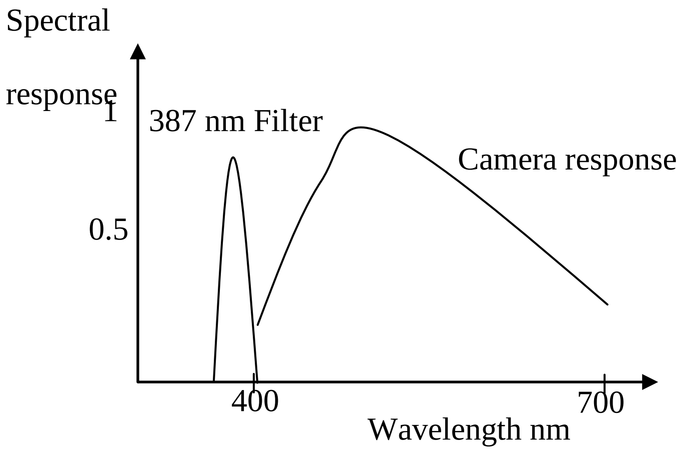

Figure 6-1 Filter and Camera Response

Aluminium metal 50 mm x 60 mm with the letters D I T of height 15 mm written on it was used as a test piece. The test piece under internal daylight is shown in Figure 6-2. The test piece of aluminium with DIT and the background are clear and distinct.

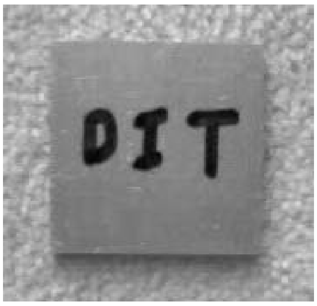

Figure 6-2 Test Piece of Aluminium

A 387 nm filter was placed in front of the camera under internal daylight and the result is shown in Figure 6-3. The result shows a complete lack of response from the camera.

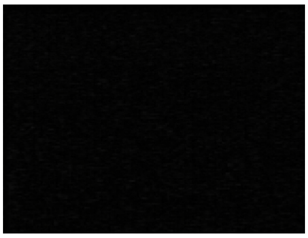

Figure 6-3 Camera Response 387 nm filter

A black light fluorescent lamp containing 387 nm wavelength light, was then switched on and the cameras response is shown in Figure 6-4.

Figure 6-4 Camera Response Filter and Light 387 nm

Due to the low intensity of 387 nm lighting, the camera was moved closer to the test piece. The background to the test piece is shown as dark stripes to the left and right of the image. The response of the camera clearly shows the letters D I T.

The monochrome image pixels have dynamic range values between 0 and 255. The response of the camera in this experiment provides a low dynamic range image. Using Matlab^{TM} this low dynamic range is shown quantitatively by its histogram in Figure 6-5. There are no intensity values between 185 and 255, however there is good separation between the letters DIT and the background shown by the dip in the histogram at an intensity value of 133.

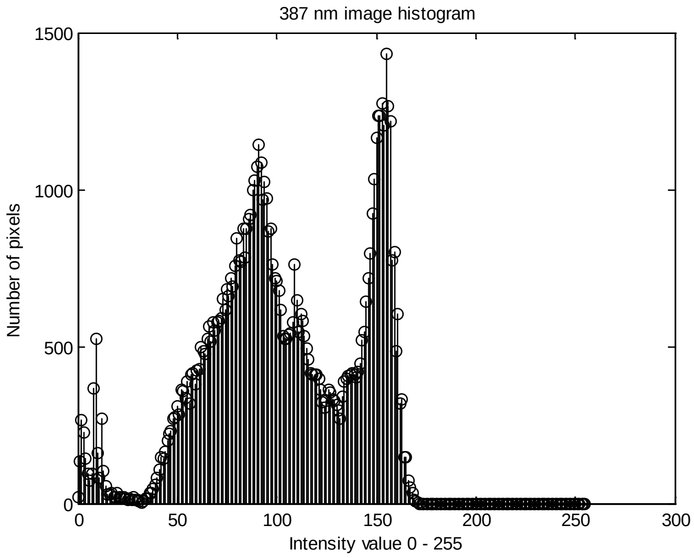

Figure 6-5 387 nm Image Histogram

The low dynamic range response is due not only to the response of the camera but from the lack of 387 nm intensity in the black light and the 387 nm filters attenuation effect.

6.1.2 Flame Removal Test Results

Using a small butane lighter flame in front of the test piece under daylight lighting produces the image shown in Figure 6-6.

Figure 6-6 Daylight with Flame

Clearly image information behind the flame is completely obliterated because of the saturation effects of the flame on the cameras photo sensors, which is shown quantitatively in the images histogram in Figure 6-7.

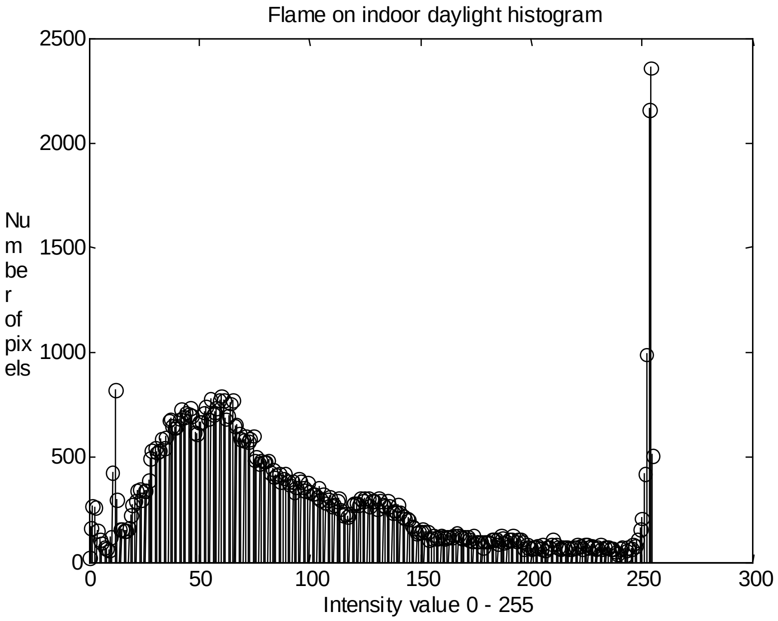

Figure 6-7 Flame On Daylight Histogram

The histogram shows 8.2% of the pixels in the image have what we would consider saturated values between 250 and 255, which are caused by the butane flame. It would be extremely difficult to obtain information from behind the flame such as the area or centroid in pixels of the letter I in this image.

The main development in this research was the development of a process that obtained this and other information about the letter I which was obscured by a butane flame. Further work is required to expand this novel concept to oxy-acetylene power flame spraying which requires ultra violet filtering and lighting at the appropriate wavelength.

Placing the 387 nm filter in front of the camera and turning on the black light with the butane flame on produces the image shown in Figure 6-8.

Figure 6-8 387 nm Lighting Flame On

This result confirms the technique proposed, as the letters D I T are clearly visible. There is a slight transmission of flame intensity just above the letter I. Letters on the torch are also visible. Figure 6-9 is a histogram of the flame on in the 387 nm image.

The histogram for the image shown in Figure 6-9 suggests this is a low contrast image and there is considerable room for improving image information above pixel value 185. This could be achieved by increasing the intensity of the 387 nm lighting source.

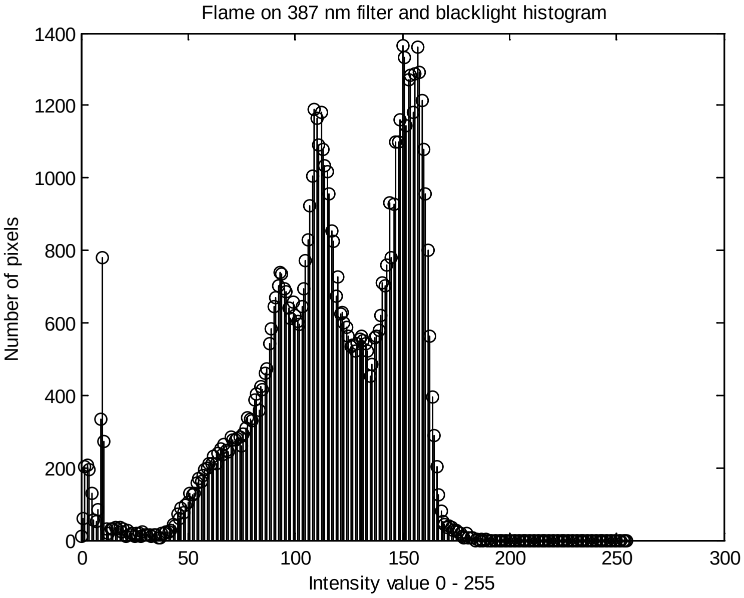

Figure 6-9 Flame on 387 nm histogram

6.1.3 Object Parameter Measurement

Using the Matlab^{TM} image processing toolbox the image in Figure 6-8 was processed using the canny edge detector with a Gaussian filter standard deviation value of 1.5 and high-low threshold values of 0.16 and 0.064 respectively which produced an edges image shown in Figure 6-10.

Figure 6-10 Edges image

The edges image in Figure 6-10 was image processed further to remove the perimeter objects using the Matlab function `imclearborder` leaving only the letters D I T. Using the Matlab^{TM} functions for labelling, selecting and infilling the letter I, `bwlabel`, `bwselect` and `imfill` the letter I was extracted as shown in Figure 6-11. For contrast the flame image is shown beside the extracted letter I

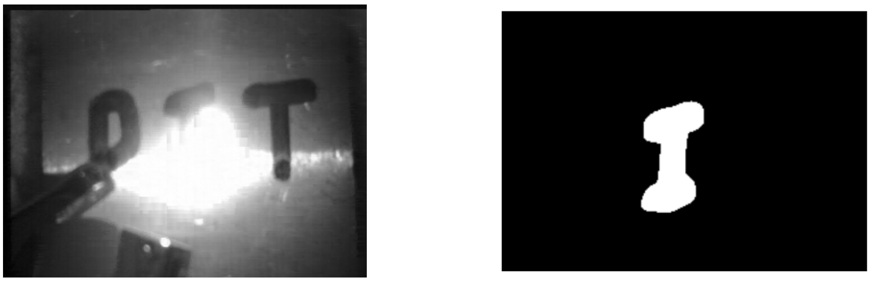

Figure 6-11 Flame on and letter I extracted

Using the Matlab^{TM} image processing toolbox and the Matlab^{TM} function `regionprops` a number of characteristics for the letter I were obtained. Some of these features are shown in Table 6-1.

Area	2561 pixels
Centroid	31, 112 measured from top left corner
Eccentricity	0.9148
Orientation	83^0
Perimeter	264 pixels

Table 6-1 Letter I Parameters

The algorithm for the image processing and analysis of the ultra violet filtered image is shown in Figure 6-12.

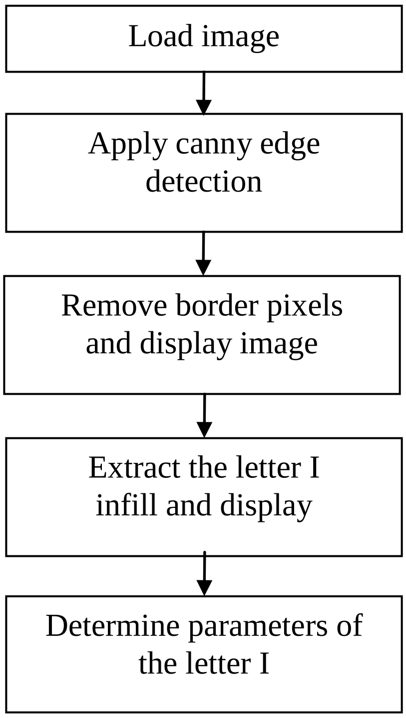

Figure 6-12 Flame Removed Image Processing Algorithm

The full Matlab^{TM} program for the image processing and analysis described named `UVFlame.m` is included in appendix G. From analysis of the above and in combination with the depth measurement technique described if an appropriate UV laser was used with the UV filtering it is a straightforward process to obtain accurate real world values from image pixel values for actuating a robot manipulator using perspective transformations, inverse kinematics and camera calibration techniques.

6.1.4 Thermal Spraying Combustion Spectra

To determine the band pass filter and lighting wavelength for the removal of the thermal spraying flame and combustion material spectrum in the thermal spraying process would require extensive testing and the purchase of a range of filters and UV lighting. The reason for this is that there are a number of thermal spraying processes such as powder, arc, plasma and a vast range of surface coating materials all producing their own combustion spectra. A list of some of the more common surface coating materials are shown in Table 6-2 (England, 2009).

- Tungsten carbide/cobalt
- Chromium carbide/nickel chromium
- Aluminium bronze
- Copper nickel indium
- Hard alloys of iron

Table 6-2 Surface Coating Materials

To apply the technique of using monochromatic ultra violet lighting and narrow band pass filter to remove the combustion process research has been conducted in identifying the spectrum produced by various materials used in powder thermal spraying. The emission spectra of flames is sensitive to a range of phenomena shown in Table 6-3 (Zizak, 2000).

- temperature
- gas/air or gas/oxygen mixture ratio
- gas purity
- burner type
- gas flow (laminar or turbulent)
- coating materials
- height of observation in the flame

Table 6-3 Flame Sensitivity Phenomena

Research provided reasonable indicators of a location for the band pass filter and where spectral problems arose. The thermal spraying process used for this research was powder thermal spraying using an Oxy-Acetylene torch.

The Oxy-Acetylene flame is a chemical reaction resulting from the combination of acetylene C_2H_2 with oxygen O_2. Figure 6-13 shows the two stages of the chemical reactions (Materials Engineering (UK) Ltd., 1997)**.**

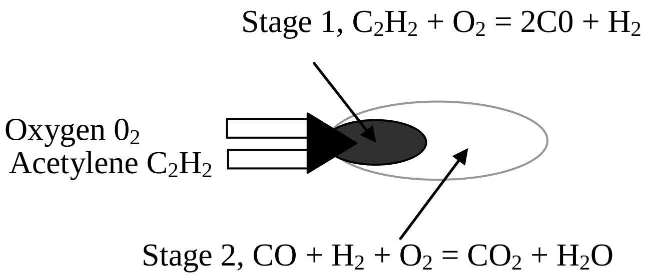

Figure 6-13 Oxy-acetylene flame

A neutral flame with products of combustion carbon dioxide (CO_2) and water (H_2O) is produced with maximum heat output when equal quantities of oxygen and acetylene are used (Materials Engineering (UK) Ltd., 1997). Controlling this mixture would form part of the overall thermal spraying robot control system.

This is an idealised view and many other ordinary molecules and unstable radicals are produced in an Oxy-Acetylene flame in air.

The visible spectrum runs from 400 nm to 750 nm and the infra red spectrum runs from 750 nm to 1 mm (Nave, 2005). This suggests a portion of the ultra violet spectrum between 350 – 400 nm commonly known as the UV-A spectrum for the research as it excludes the visible and infra red spectrum.

Research concentrated on identifying weak spectra between 350 nm and 400 nm from the powder flame spraying Oxy-Acetylene in air flame with a range of molten surface coating materials, which is widely used in the powder spraying industry.

The ordinary molecules which are the stable products of combustion, H_20, $C0_2$, C0, 0_2 or N_2 in hydrogen flames do not provide spectra of any appreciable strength in the visible or ultra violet spectrum (Zizak, 2000).

The only product of combustion that may have an appreciable spectrum in the UV band is the hydroxyl radical OH which give band peaks at 281 nm, 306 nm, and 343 nm. Oxyacetylene flames not only produce spectra of hydrogen flames but also emit radiation of hydrocarbon radicals. Between the 350 nm and 400 nm wavelengths a weak CH band occurs at 387/9 nm and a strong band at 432 nm are found in air acetylene flames. This suggests many wavelengths between 350 and 400 nm may be suitable for removing the Oxy-Acetylene flame in air but we must add the spectrum from the surface coating material to ensure there is no appreciable interference from the molten material in our chosen UV band. A review of published work by DeSaro and Weisberg (DeSaro, et al., 2001) relating to emission spectra of molten elements provides information on spectra of interest listed in Table 6-4.

Aluminium	390 – 400 nm
Iron	356 – 365 nm
Magnesium	380 - 385 nm
Copper	320 – 330 nm

Table 6-4 Material Emission Spectra

This research suggests using a narrow band pass filter and lighting between 330 and 355 nm In addition to the interference from the emission spectra, an added complication is the molten material itself. This will act as a dust cloud and have the effect of reducing contrast in the image.

This research detailed a system of combining optical filtering and image processing which can be used to obtain information about low contrast objects behind or within a test butane flame.

The research also suggests a region within the UV-A spectrum, which shows promise for implementing ultra violet vision system control of a thermal-spraying robot.

The ability to see through a flame could have benefits in other industries such as the fire fighting service and welding. The system detailed could be fitted as a single eye head up display or fitted to a small mobile robot where there are low smoke flame environments.

CHAPTER 7

CONCLUSIONS & FUTURE WORK

7.1 Aims and Objectives

The aim of this research was to review the broad range of robot subsystems and identify novel areas for development which are specifically related to thermal spraying robotics. The objectives of this research resulted in mathematic modelling, software simulation and testing novel ideas in the area of robot kinematics, distance measurement and a flame removal vision system. The following sections detail the research conclusions and further work in each of the key areas associated with thermal spraying robotics.

7.2 Robot Actuators, Trajectory Planning, and Dynamics

The review of robot actuators, trajectory planning, and dynamics resulted in the conclusion that for the development of thermal spraying robotic systems, trajectory planning can be achieved using a standard 5th order polynomial to ensure smooth velocity and accelerations of robot arm joints.

The review of actuators suggests that standard brushless motors of the trapezoidal type with a high ratio reduction gear box is the actuator of choice because of their significant advantages over permanent magnet d.c. motors such as low maintenance, low rotor inertial and reducing costs. With modern digital signal controllers and power electronics the control of brushless motors particularly the trapezoidal type is relatively straight forward.

The review of dynamic modelling resulted in the conclusion that a significantly reduced dynamic model can be used due to the fact that the thermal spraying process is relatively slow and a high reduction ratio gearbox fitted to the electric actuator is required for this speed reduction and torque increase. The dynamic model reduces to a straightforward linear model with a disturbance input. Standard control system algorithms can therefore be applied.

There is however significant opportunity for further research in this area particularly sensor-less control of brushless motors and control strategies for direct drive high speed robot applications where the full dynamic model must be taken into account.

7.3 Robot Kinematics

The review of robot kinematics led to the development of the forward and inverse kinematics of a non standard robot manipulator which maximises the robots workspace envelope. This is achieved by offsetting the robot arm links to allow continuous rotation waist, shoulder and elbow joints. To minimise cost the rotation axis was excluded so only pitch and yaw axis were included. This reduced the search space for finding the inverse kinematic parameters however both software and hardware tests have shown that the solutions found are correct.

An importance and novel solution to the delivery of power and data through the continuous rotation joints is proposed in this research i.e the development of slip rings and brushes using PTFE electroless nickel. The advantages of this surface coating material are its low friction, low wear and is a conductor. Tests on electroless nickel samples confirm low friction and conductivity features of this material. There is a possibility of commercialising this solution if funding is obtained to develop a prototype using PTFE electroless nickel and conducting more extensive testing.

7.4 Substrate Orientation and Measurement

The tests conducted using a low cost monochrome camera and presentation laser has shown that depth measurement can be conducted without significant setup or calibration. Tests using a matt black surface measured a fixed distance of 200 mm with an accuracy of ±0.6% error when a calibration factor is included. Similar results are expected if an ultra violet laser was used. Image processing and analysis tests were carried out under a single wavelength infra red lighting to prove the concept however follow on research suggests the ultra violet spectrum is a better choice for single wavelength image processing and analysis in the thermal spraying environment. This is a novel approach to distance measurement in the harsh environment of thermal spraying and further work in this area would be required involving the use of ultra violet lasers, ultra violet optical filters and lighting for the specific thermal spraying process, however this research has successfully demonstrated the concept of distance measurement using single wavelength light and low cost monochrome cameras.

7.5 Thermal Spraying Vision System

Tests using a single wavelength ultra violet filter, ultra violet lighting, low cost monochrome camera, image processing and analysis and a butane flame have proved the concept of flame removal using optical filtering. A review of the spectra expected from thermal spraying using an Oxy-Acetylene torch and a range of core surface coating elements suggest a band in the ultra violet spectrum between 330 nm – 355 nm where there are low intensities from the combustion process. This flame removal research could have benefits in other industries such as the fire fighting service and welding.

Further research in this area would be required involving the use of ultra violet optical filters, lighting and image processing and analysis techniques for object identification and measurement specific to the thermal spraying process.

However this research has successfully demonstrated the concept of flame removal from an image using ultra violet optical filtering, lighting, low cost monochrome cameras and image processing and analysis techniques.

There is also further work in the area of image processing and analysis of low contrast images. An area of interest is the application of Type 2 Fuzzy Logic (Type2FuzzyLogic, 2009) to image processing and analysis.

References

1. **ABB. 2009.** ABB, Robotics. [Online] 2009. [Cited: 20 February 2009.] http://www.abb.com/robotics.
2. **AirProducts. 2009 et. al..** Technical Paper Thermal Spraying. *Air Products.* [Online] Air Products and Chemicals Inc., 2009 et. al. http://www.airproducts.com/Products/CylinderGases/MAXX/ThermalSpraying/thermalspraying_techpaper.htm.
3. **Antriebstechnik, Gesellschaft für. 2009.** Rotating Unions. *GAT.* [Online] 2009. [Cited: 14 April 2009.] http://www.gat-mbh.de/index.php?page=rotating_unions-en&group=produkte-en:rotating_unions-en.
4. **Bacchi, Paul and Filipski, Paul S. 1997.** *Continuously Rotatable Multiple Link Robot Arm Mechanism. W09702932* 1997.
5. **Bonfe, M. and Bergo, M. 2008.** A Brushless Motor Drive with Sensorless Control for Commercial Vehicle Hydraulic Pumps. *IEEE International Symposium on Industrial Electronics.* s.l. : Institute of Electrical and Electronics Engineers Inc., 2008.
6. **Candel, A. and Gadow, R. 2006.** *Optimized multiaxis robot kinematic for HVOF spray coatings on complex shaped substrates.* s.l. : The 2nd International Meeting on Thermal Spraying 2nd RIPT, Elsevier, 2006.
7. **Castolin, Eutectic.** *Superjet Flame Configuration, General Procedure Guideines.* s.l. : http://www.castolin.com.

8. **Committee, Surface Engineering. 2000.** *Foresignt in Surface Engineeing.* s.l. : The Institute of Materials, 2000.
9. **Corke, P. I. 1994.** *High Performance Visual ClosedLoop RobotControl Phd.* Melbourne : University of Melbourne, 1994. pp. 111-118,151.
10. **Davis, J. R. 2005.** *Hanbook of Thermal Spay Technology.* s.l. : Thermal Spray Society and ASM International, 2005. pp. 7-8.
11. **Denavit, J. Hartenberg, R. S. 1955.** A kinematic notation for lower-pair mechanisms based on matrices. 1955, 23, pp. 215-221.
12. **DeSaro, Robert and Weisberg, Arel. 2001.** *In Situ Real Time Measurement of Melt Constituents.* s.l. : Energy Research Company, 2001.
13. **Dianqi. L, Dingyu, X. , Tao, L.Jianguo, C. Xinhe, X. 2007.** Dynamic Model of a 3 DOF Direct Drive Robot and its Control Mode. China : IEEE International Conference on Control and Automation, 2007.
14. **Engineers_Handbook. 2006.** Coefficient of Friction. *Engineers Handbook.* [Online] 2006. [Cited: 15 April 2009.] http://www.engineershandbook.com/Tables/frictioncoefficients.htm.
15. **England, Gordan. 2009.** Conversion from Vickers Hardness Number to SI Units. *Godan England.* [Online] 2009. [Cited: 15 Apil 2009.] http://www.gordonengland.co.uk/hardness/hvconv.htm.
16. **England, Gordon. 2009.** Wear Resistance. *gordonengland.* [Online] Gordon England, 2009. [Cited: 15 May 2009.] http://www.gordonengland.co.uk/wear.htm.
17. **FANUC. 2008.** FANUC Robotics. [Online] 2008. [Cited: 20 February 2009.] http://www.fanucrobotics.com/.

18. **Forste, Walter and Teuschler, Hans-Joachim. 1972.** *Commutators and Sliprings for Electric Machines. GB 1281827* 1972.
19. **GIMP. 2009.** GIMP. *GIMP.* [Online] 2009. [Cited: 6 May 2009.] http://www.gimp.org/.
20. **Halling, J. 1976.** *Introduction to Tribology.* London : Wykeham PublicationsLtd., 1976. p. 57.
21. **Hansbo, A. and Nylen, P.E. 2000.** *Modeling ofspray deposition and robot motion optimizaton for a gas turbine application.* Montreal : Prodeedings of the International Thermal Spray Conference, ASM Thermal Spray Society, 2000.
22. **Harmonic-Drive. 2009.** Harmonic Drive. [Online] 2009. [Cited: 20 February 2009.] http://www.harmonicdrive.net/.
23. **Hermanek, F. J. 2005.** *What is Thermal Spray.* s.l. : International Thermal Spray Association, 2005.
24. **Higashimoto, A., et al. 1993.** *Study of plasma gun orientation control with ultrasonic sensors for thermal spaing robot.* s.l. : Transactions of the IMACS/SCIE International Syposium on Robotics, Mechatronics and Manufacturing Systems, Elsevier Science, 1993. p. 605.
25. **Hightech_Plating. 2009.** Hightech Plating Ltd. *Hightech Plating Ltd.* [Online] 2009. [Cited: 14 April 2009.] http://www.hitechplating.ie/index.html.
26. **Hokuyo. 2009.** Scanning range finder. *Hokuyo.* [Online] Hokuyo, 2009. [Cited: 5 January 2010.] http://www.hokuyo-aut.jp/02sensor/07scanner/ubg_05ln.html.
27. **Hughes, Austin. 1990.** *Electric Motors and Drives.* Oxford : Newnes, 1990. pp. 257-288,318. ISBN 0 7506 1741 1.
28. **IFR. 2008.** *World Robots 2008.* s.l. : Internation Federation of Robotics, 2008.

29. **Jones, Douglas W. 2008.** Contol of Stepping Motors. [Online] 2008. [Cited: 20 February 2009.] http://www.cs.uiowa.edu/~jones/step/.
30. **Kennedy, David M.** *Surface Engineering Addressing Maintenance Applications.* Dublin : Dublin Insttute of Technology.
31. **Kutay, Aydan and Weiss, Lee.** *Assessment of the strategic benifits of robotic operations: A case study of a thermal spraying robot.* Pittsburg : IEEE.
32. **Marshall, A. D. and R.Martin, R. 1992.** *Computer Vision, Models and Inspection.* s.l. : World Scientific Publishing Co. Ltd., 1992. pp. 101, 36-42. ISBN 9810207727.
33. **Materials Engineering (UK) Ltd. 1997.** Oxy-Gas Weding. *Materials Engineering Group.* [Online] Materials Engineering, 1997. [Cited: 15 May 2009.] http://www.meg.co.uk/courses/4.php.
34. **MathWorks, The. 2010.** Image Processing Toolbox 6.4. *The MathWorks.* [Online] The MathWorks, 2010. [Cited: 4 January 2010.] http://www.mathworks.com/products/image/.
35. **MaxBotix. 2009.** MaxSonar high performance ultrasonic range finders. *MaxBotix.* [Online] MaxBotix, 2009. [Cited: 5 Janauary 2010.] http://www.maxbotix.com/?gclid=CKDtx9r8jJ8CFQdl4wodowcEJg.
36. **Mercotac. 2009.** Mercotac. *Mercotac.* [Online] Mercotac, 2009. [Cited: 14 April 2009.] http://www.mercotac.com/.
37. **Microchip Technology Inc. 2003.** *Brushless DC (BLDC) Motor Fundamentals.* s.l. : Microchip Technology Inc. , 2003. AN885.
38. **Microchp Technology Inc. 2009.** Digital Signal Controllers. *Microchip.* [Online] 2009. [Cited: 31 December 2009.]

http://www.microchip.com/stellent/idcplg?IdcService=SS_GET_PAGE&nodeId=2629&param=en533462.

39. **Mitsubshi. 2008.** Robotics. [Online] 2008. [Cited: 20 February 2009.] http://www.mitsubishirobot.com/.
40. **Moody, R. Dale. 2008.** *Off-line development of robot motion programs.* Miami : Welding Journal, American Welding Society, 2008.
41. **NationMaster. 2005.** NationMaster. *NationMaster.* [Online] 2005. [Cited: 22 November 2008.] http://www.nationmaster.com/encyclopedia/Ctesibius-of-Alexandria.
42. **Nave, C. R. 2005.** The Electromagnetic Spectrum. *Hyper Physics.* [Online] 2005. [Cited: 15 May 2009.] http://hyperphysics.phy-astr.gsu.edu/Hbase/ems1.html#c1.
43. **Newton, Braga C. 2002.** *Robotics, Mechatronics and Artifical Intelligence.* s.l. : Newnes, 2002. pp. 72-73.
44. **Niku, Saeed B. 2001.** *Introduction to Robotics Analysis, Systems, Applications.* New Jersey : Prentice Hall, 2001. pp. 2, 157,178. ISBN 0-13-061309-6.
45. **NKS. 2009.** NKS Megatorque motors. [Online] 2009. [Cited: 20 February 2009.] http://www.npa.nsk.com/public/enu/1001_1215.asp.
46. **P.I.Corke. 1994.** *Hight Performance Visual Closed Loop Robot Contol PhD.* s.l. : University of Melborne, 1994. pp. 111-118,151.
47. **Peritt, J., Tsai, L-W. and Vranish, J. 1994.** *The Development of Flex-gears for the Conduction of Electricity Across a Continuously Rotating Joint.* s.l. : Institute for Systems Research, 1994. T.R. 95-94.
48. **Philip, Blazdell and Kurodo, Seiji. 1999.** Thermal Spraying an Overview. 1999, Vol. 7, 4, pp. 205 - 207.

49. **Point Grey Research Inc. 2009.** Sterio vision products. *Point Grey.* [Online] Point Grey Research Inc., 2009. [Cited: 5 Jauary 2010.] http://www.ptgrey.com/products/stereo.asp?gclid=CIKtyKz-jJ8CFUgA4wodXRNkIw.
50. **Rastegar, J., Qin, Y. and Tu, Q. 1995.** *On the optimal robot manipulator motion planning for solid freeform fabrication by thermal spraying* . Boston : Proceedings of the 1995 ASME Design Engineering Technical Conference , 1995.
51. **Rizzoni, Giorgo. 2000.** *Principles and Applications of Electrical Engineerng.* s.l. : McGrawHill, 2000. pp. 854-855, 897-905, 890- 894. ISBN 0-07-117727-2.
52. **Robinson, Sam. 2006.** *Drive and Control Electronics Enhance the Brushless Motors Advantages.* s.l. : Penton Publishing, 2006.
53. **Rotary_Systems. 2009.** Rotary Systems Inc. *Rotary Systems Inc.* [Online] Rotary Systems Inc., 2009. [Cited: 14 April 2009.] http://www.rotarysystems.com/index.htm.
54. **Samsung. 2009.** Samsung 1/3 CCD image sensor for CCIR cameras datasheet. *datasheetcatalog.com.* [Online] 2009. [Cited: 8 May 2009`.] http://www.datasheetcatalog.com/datasheets_pdf/K/C/7/3/KC73129MP.shtml.
55. **Schilling, Robert J. 1990.** *Fundamentals of Robotics Analysis and Control.* s.l. : Prentice Hall, 1990. pp. 11,83,206,208-212, 337-340.
56. **School_Science. 2009.** Resistance and Resistivity. *School Science.* [Online] 2009. [Cited: 15 April 2009.] http://resources.schoolscience.co.uk/CDA/16plus/copelech2pg1.html.
57. **Sciavicco, L. Siciliano, B. 2004.** *Modelling and Control of Robot Manipulators.* London : Springer-Verlag, 2004. pp. 1,215, 217. ISBN 1-85233-221-2.

58. **Sharp.** *General pupose type distance measuring sensors.* s.l. : Sharp.
59. **Shelton, B. 2008.** Types of Robot. *Rover Ranch.* [Online] National Aeronautics and Space Administration, 2008. [Cited: 7 April 2009.] http://prime.jsc.nasa.gov/ROV/types.html.
60. **Shelton, Bob. 2003.** A Short History of Robots. *Rover Ranch NASA.* [Online] NASA, 4 April 2003. [Cited: 22 November 2008.] http://prime.jsc.nasa.gov/ROV/history.html.
61. **Stanford. 2007.** Robots and their arms. *Computer History Exhibits.* [Online] Stanford University, 2 5 2007. [Cited: 22 November 2008.] http://infolab.stanford.edu/pub/voy/museum/pictures/display/1-Robot.htm.
62. **STMicroelectronics. 2001.** *L297 Stepper Motor Controllers.* s.l. : STMicroelectronics, 2001.
63. **Stokes, Joseph. 2008.** *The Theory and Application of HVOF Thermal Spray Process.* Dublin : Dublin City University, 2008. p. X. ISBN 1-87232-753-2.
64. **Surface_Technology. 2009.** Composite PTFE Electroless Nickel . *Surface Technology Inc.* [Online] 2009. [Cited: 15 April 2009.] http://www.surfacetechnology.com/specs-500.html.
65. **TWR. 2009.** Electless Nickel / Teflon Specifications. *TWR Service Coporations.* [Online] TWR Service Corporations, 2009. [Cited: 15 April 2009.] http://www.twrservice.com/id27.html.
66. **Type2FuzzyLogic. 2009.** Type 2 Fuzzy Logc. *Type 2 Fuzzy Logic.* [Online] 2009. [Cited: 6 May 2009.] http://www.type2fuzzylogic.org/.
67. **USArmyCorpofEngineers. 1999.** *Engineering and Design - Thermal Spraying New Constrction and Maintenance EM 1110-2-3401.* 1999. pp. 7-3.

68. **Watanabe, T. and Higashimoto, A. 2004.** *A study of plasma gun orientation contol accuracy for the thermal spay robot.* Osaka : Proceedings of the International Thermal Spray Conference, ASM International, 2004.

69. **Whelan, Paul F. and Molloy, Derek. 2001.** *Machine Vision Algorithms in Java.* s.l. : Springer, 2001. pp. 233-259. ISBN 1852332182.

70. **Winter, Mark. 2009.** Hardness Vickers. *Web Elements.* [Online] 2009. [Cited: 15 April 2009.] http://www.webelements.com/periodicity/hardness_vickers/.

71. **Zieris, R. and Schmidt, A. 2004.** *Off-line programming for spraying and laser cladding of three-dimentional surfaces.* Osaka : Prodeedings of the International Thermal Spray Conference, ASM Inernational, 2004.

72. **Zizak, Giorgo. 2000.** *Flame Emission Spectroscopy: Fundamentals and Applicaitons.* Milano : Instituto pre la Tecnologia dei Materiali , 2000.

Publications

D. Breen, E.Coyle, D Kennedy, *Thermal Robotic Arm Controlled Spraying (TRACS),* Control 04, University of Bath, U.K. 6-9 September 2004.

D. Breen, E.Coyle, D. Kennedy, *Thermal Spraying Robot Kinematics and Laser Pattern Control*, International Conference on Informatics in Control, Automation and Robotics, Barcelona Spain 14-17 September 2005.

D.Breen, E.Coyle, D.M.Kennedy, *Infra Red Servoing of a Thermal Spraying Robot* , Materials, Energy and Design (MED06), Dublin Institute of Technology, Ireland 14th-17th March 2006

D. Breen, E.Coyle, D. Kennedy, *Ultra Violet Imaging Transducer Control of A Thermal Spraying Robot* , International Conference on Informatics in Control, Automation and Robotics, Angers, France 9th-12th May 2007.

Appendices

Matlab^{TM} Program Listings

A Trajectory Planning

B Trajectory function and dynamics

C Forward Kinematics

D Forward Kinematics Robot Arm Matrix Equations

E Wrist Matrix Equations

F Inverse Kinematics

G Flame Removal

Appendix A

Trajectory planning

```
% Author: Dermot Breen
% Date: 24 October 2008
% Program: 5th order polynonial trajectory planning


clear all;
clf;


% Initial and Final times(seconds)

tI = input(' \n Enter initial time in seconds  ');
tF = input(' \n Enter final time in seconds   ');


%Initial and final position (radians), velocity radians/second
%and acceleration radians/second/second

iP = input(' \n Enter initial position in radians   ');
fP = input(' \n Enter final position in radians   ');

iV = input(' \n Enter initial velocity in radians/second   ');
fV = input(' \n Enter final velocity in radians/second   ');

iA = input(' \n Enter initial acceleration in radians/second/second
');
fA = input(' \n Enter final acceleration in radians/second/second
');


% Solution of fifth order polynomial coefficients

%Matrix construction from initial and final
%time boundary conditions provided

a0 = 1;
a1 = tI;
a2 = tI.*tI;
a3 = tI.*tI.*tI;
a4 = tI.*tI.*tI.*tI;
a5 = tI.*tI.*tI.*tI.*tI;


b0 = 1;
b1 = tF;
b2 = tF.*tF;
b3 = tF.*tF.*tF;
b4 = tF.*tF.*tF.*tF;
b5 = tF.*tF.*tF.*tF.*tF;
```

```
c0 = 0;
c1 = 1;
c2 = 2*tI;
c3 = 3*tI.*tI;
c4 = 4*tI.*tI.*tI;
c5 = 5*tI.*tI.*tI.*tI;

d0 = 0;
d1 = 1;
d2 = 2*tF;
d3 = 3*tF.*tF;
d4 = 4*tF.*tF.*tF;
d5 = 5*tF.*tF.*tF.*tF;

e0 = 0;
e1 = 0;
e2 = 2;
e3 = 6*tI;
e4 = 12*tI.*tI;
e5 = 20*tI.*tI.*tI;


f0 = 0;
f1 = 0;
f2 = 2;
f3 = 6*tF;
f4 = 12*tF.*tF;
f5 = 20*tF.*tF.*tF;


timeMatrix = [a0 a1 a2 a3 a4 a5; b0 b1 b2 b3 b4 b5 ; ...
      c0 c1 c2 c3 c4 c5 ; d0 d1 d2 d3 d4 d5 ; e0 e1 e2 e3 e4 e5 ; ...
      f0 f1 f2 f3 f4 f5];



% Initial conditions vector

initialConditions = [ iP fP iV fV iA fA ];



%Calculation of fifth order polynomial coefficients using
%inverse matrix mathematics

invTimeMatrix = inv(timeMatrix);

fprintf('\n\n5th order polynomial\n')

coefficients = invTimeMatrix*initialConditions'



% Calculation of position, velocity and acceleration trajectories

t = tI :(tF - tI)/20 : tF
```

```
% time line from initial and final velocities


tOne = t;
tTwo = t.*t;
tThree = t.*t.*t;
tFour = t.*t.*t.*t;
tFive = t.*t.*t.*t.*t;


position = coefficients(1)+ coefficients(2).*tOne + ...
   coefficients(3).*tTwo + coefficients(4)*tThree + ...
   coefficients(5).*tFour + coefficients(6).*tFive;

velocity = coefficients(2) + 2*coefficients(3).*tOne + ...
   3*coefficients(4)*tTwo + 4*coefficients(5).*tThree + ...
   5*coefficients(6).*tFour;

acceleration = 2*coefficients(3) + 6*coefficients(4)*tOne + ...
   12*coefficients(5).*tTwo + 20*coefficients(6).*tThree;


% Plots of position, velocity and acceleration trajectories

plot(t,position);
hold on
plot(t,velocity,'r');
hold on
plot(t,acceleration,'g');

title('Position (blue), velocity (red) and acceleration (green)
trajectories');
xlabel(' Time  - seconds ');
ylabel(' position - rad (blue), velocity - r/s (red), acceleration -
r/s/s (green)');
```

Appendix B

Trajectory function

```
function [ t, position, velocity, acceleration ] = trajectory


% Author: Dermot Breen
% Date: 24 October 2008
% Program: 5th order polynonial trajectory planning
% This function returns the time line, position, velocity and
% acceleration for a given trajectroy
% Example of syntax [ t, position, velocity, acceleraton] =
trajectroy;

clear all  % clear workspace variables

% Initial and Final times(seconds)

tI = input(' \n Enter initial time in seconds  ');
tF = input(' \n Enter final time in seconds   ');


%Initial and final position (radians), velocity radians/second
%and acceleration radians/second/second

iP = input(' \n Enter initial position in radians   ');
fP = input(' \n Enter final position in radians   ');

iV = input(' \n Enter initial velocity in radians/second   ');
fV = input(' \n Enter final velocity in radians/second   ');

iA = input(' \n Enter initial acceleration in radians/second/second
');
fA = input(' \n Enter final acceleration in radians/second/second
');
```

```
% Solution of fifth order polynomial coefficients

%Matrix construction from initial and final
%time boundary conditions provided

a0 = 1;
a1 = tI;
a2 = tI.*tI;
a3 = tI.*tI.*tI;
a4 = tI.*tI.*tI.*tI;
a5 = tI.*tI.*tI.*tI.*tI;


b0 = 1;
b1 = tF;
b2 = tF.*tF;
b3 = tF.*tF.*tF;
b4 = tF.*tF.*tF.*tF;
b5 = tF.*tF.*tF.*tF.*tF;


c0 = 0;
c1 = 1;
c2 = 2*tI;
c3 = 3*tI.*tI;
c4 = 4*tI.*tI.*tI;
c5 = 5*tI.*tI.*tI.*tI;

d0 = 0;
d1 = 1;
d2 = 2*tF;
d3 = 3*tF.*tF;
d4 = 4*tF.*tF.*tF;
d5 = 5*tF.*tF.*tF.*tF;

e0 = 0;
e1 = 0;
e2 = 2;
e3 = 6*tI;
e4 = 12*tI.*tI;
e5 = 20*tI.*tI.*tI;


f0 = 0;
f1 = 0;
f2 = 2;
f3 = 6*tF;
f4 = 12*tF.*tF;
f5 = 20*tF.*tF.*tF;


timeMatrix = [a0 a1 a2 a3 a4 a5; b0 b1 b2 b3 b4 b5 ; ...
      c0 c1 c2 c3 c4 c5 ; d0 d1 d2 d3 d4 d5 ; e0 e1 e2 e3 e4 e5 ; ...
      f0 f1 f2 f3 f4 f5];
```

```
% Initial conditions vector

initialConditions = [ iP fP iV fV iA fA ];



%Calculation of fifth order polynomial coefficients using
%inverse matrix mathematics

invTimeMatrix = inv(timeMatrix);

coefficients = invTimeMatrix*initialConditions';



% Calculation of position, velocity and acceleration trajectories

t = tI :(tF - tI)/20 : tF ; % time line from initial and final
velocities

tOne = t;
tTwo = t.*t;
tThree = t.*t.*t;
tFour = t.*t.*t.*t;
tFive = t.*t.*t.*t.*t;


position = coefficients(1)+ coefficients(2).*tOne + ...
   coefficients(3).*tTwo + coefficients(4)*tThree + ...
   coefficients(5).*tFour + coefficients(6).*tFive;

velocity = coefficients(2) + 2*coefficients(3).*tOne + ...
   3*coefficients(4)*tTwo + 4*coefficients(5).*tThree + ...
   5*coefficients(6).*tFour;

acceleration = 2*coefficients(3) + 6*coefficients(4)*tOne + ...
   12*coefficients(5).*tTwo + 20*coefficients(6).*tThree;
```

```
% Plots of position, velocity and acceleration trajectories


figure('Name', ' Position, Velocity and Acceleration trajectory plots
')

subplot(2,2,1),plot(t,position);

title('Position trajectory');
xlabel('Time  - seconds ');
ylabel('Position - radians');


subplot(2,2,2),plot(t,velocity);

title('Velocity trajectory');
xlabel('Time  - seconds ');
ylabel('Velocity - rad/s');

subplot(2,2,3),plot(t,acceleration);

title('Acceleration trajectory');
xlabel('Time  - seconds ');
ylabel('Acceleration - rad/s/s ');
```

```
function dynamics

% Author:   Dermot Breen
%
% Date:     24 October 2008
%
% Program:  Dynamic equations of motion
%           two link planer arm
%
% This function determines the load torques for a
% two axis planer arm based on a user defined trajectory
% and link parameters

clear all % clear workspace variables

% Two link planer arm parameters

fprintf(' \n\n ***** Two link planar arm parameters ***** \n');

% Link Lengthin meters
a1 = input(' \n Enter link one length in meters  '  );
a2 = input(' \n Enter link two lenght in meters  ');

% Link masses in kg
m1 = input(' \n Enter link one mass in kg  ');
m2 = input(' \n Enter link two mass in kg   ');
N = input(' \n Enter gear reduction ratio   ');


% Determination of joint one load torque

% Define trajectory for joint one

fprintf(' \n\n ***** Joint one trajectory data *****\n ')

[ t, thetaP1, thetaV1, thetaA1 ] = trajectory;


% Define trajectory for joint two

fprintf(' \n\n ***** Joint two trajectory data *****\n')

[ t, thetaP2, thetaV2, thetaA2 ] = trajectory;
```

```
% Determination of joint one laod torque

% Joint one torque equations

% Inertial torques

tq1_part1 = ((((m1/3)+ m2)*a1*a1 + m2*a1*a2*cos(thetaP2) +
(m2*a2*a2)/3).*thetaA1)/(N*N);

tq1_part2 = (((m2*a1*a2*cos(thetaP2))/2 +
(m2*a2*a2)/3).*thetaA2)/(N*N);

inertialTotal = tq1_part1 + tq1_part2;

% Centrifugal and coriolis torques

tq1_part3 = (-
m2*a1*a2*sin(thetaP2).*(thetaV1.*thetaV2+.5.*thetaV2.*thetaV2))/(N*N);

% Gravittional torques

tq1_part4 = (  (m1/2 + m2)*a1*cos(thetaP1)  +   m2*a2*cos(thetaP1 +
thetaP2) ) /2;

tq1_part4 = (tq1_part4*9.81)/N;

% Total torque

tq1 = tq1_part1 + tq1_part2 + tq1_part3 + tq1_part4;


% Determination of joint two load torque

% Joint two torque equations

% Jont one inertial torque

% Inertial torque

tq2_part1 = ((m2*a1*a2*cos(thetaP2))/2 + (m2*a2*a2/3).*thetaA1)/(N*N);

tq2_part2 = ((m2*a2*a2/3).*thetaA2)/(N*N);

% Centrifugal torque

tq2_part3 = (m2*a1*a2*sin(thetaP2).*(thetaV1.*thetaV1))/(2*N*N);

% Gravitational torque

tq2_part4 = (m2*a2*cos(thetaP1+thetaP2))/2;

tq2_part4 = (tq1_part4*9.81)/N;

% Total torque

tq2 = tq2_part1+tq2_part2+tq2_part3+tq2_part4;
% Ploting of joint torques joint one and two
```

```
figure('Name' , ' Load Torque Curves ')

plot(t,tq1,'g',t,tq2,'r'),title ('Load torque curves
'),xlabel('Time,s'),ylabel(' Torque, Nm');
legend('Joint 1', 'Joint 2',0);


%Final posture of two axis planer arm


% Joint one coordinates fixed at x1 = 0, y1 = 0 ;

% Final joint two cordinates x2 , y2


x2=a1*cos(thetaP1);
y2=a1*sin(thetaP1);


% Final manipulator end point position x, y

x=a1*cos(thetaP1)+ a2*cos(thetaP1 + thetaP2);
y=a1*sin(thetaP1)+ a2*sin(thetaP1 + thetaP2);


%Plot manipulator final posture

figure('Name', ' Posture of two axis planar robot arm ')
plot(x,y,'g',x2,y2,'r'),title(' Posture of two axis planar robot
arm'),xlabel('X position'),ylabel('Y position')
legend('Joint 1 & 2','Joint 1',0)
axis( [-(a1+a2+1)(a1+a2+1) 0 (a1+a2+1)] )

% Links

% one

endpt=length(x2);
xl1=[0 x2(endpt)];
yl1=[0 y2(endpt)];
line(xl1,yl1);

%two

endpt2=length(x);
xl2=[x2(endpt), x(endpt2)];
yl2=[y2(endpt) y(endpt2)];
line(xl2,yl2);

figure('Name' , ' Torque curves ')
subplot(2,2,1), plot(t,inertialTotal),title ('Joint one inertial
torque'),xlabel('Time,s'),ylabel(' Torque, Nm');
subplot(2,2,2), plot(t,tq2_part3),title ('Joint one centifugal &
coriolis torque'),xlabel('Time,s'),ylabel(' Torque, Nm');
subplot(2,2,3), plot(t,tq2_part4),title ('Joint one gravitational
torque'),xlabel('Time,s'),ylabel(' Torque, Nm');
```

Appendix C

Forward Kinematics

```
function [dbsol] = forwardKinematics(angle)
% Dermot Breen
% April 2009

% Forward Kinematics of a five axis robot arm with 360 degree
% waist, shoulder and elbow joints and limited ovement pan and tilt.
% Enter angles in degrees axis_5([angle1 angle2 angle3 angle4 angle5])



% Homegeneous tansformation matrices

%Joint 1
syms theta1 d1 a1 alpha1;

A1R1 = [cos(theta1),  0       ,  sin(theta1) , 0 ] ;
A1R2 = [sin(theta1),  0       , -cos(theta1) , 0 ] ;
A1R3 = [0          ,  1       ,  0           , d1] ;
A1R4 = [0          ,  0       ,  0           , 1 ] ;

A1 =[ A1R1 ; A1R2 ; A1R3 ; A1R4 ] ;


%Joint 2
syms theta2 d2 a2 alpha2 ;

A2R1 = [cos(theta2), -sin(theta2),  0, a2*cos(theta2)] ;
A2R2 = [sin(theta2),  cos(theta2),  0, a2*sin(theta2)] ;
A2R3 = [0          ,  0          ,  1, d2            ] ;
A2R4 = [0          ,  0          ,  0, 1             ] ;

A2 =[ A2R1 ; A2R2 ; A2R3 ; A2R4 ] ;

%Joint 3
syms theta3 d3 a3 alpha3 ;

A3R1 = [cos(theta3), -sin(theta3),  0, a3*cos(theta3)] ;
A3R2 = [sin(theta3),  cos(theta3),  0, a3*sin(theta3)] ;
A3R3 = [0          ,  0          ,  1, d3            ] ;
A3R4 = [0          ,  0          ,  0, 1             ] ;

A3 =[ A3R1 ; A3R2 ; A3R3 ; A3R4 ] ;
```

```
%Joint 4
syms theta4 d4 a4 alpha4  ;

A4R1 = [cos(theta4),  0,  -sin(theta4), 0] ;
A4R2 = [sin(theta4),  0,   cos(theta4), 0] ;
A4R3 = [0          , -1,   0          , 0] ;
A4R4 = [0          ,  0,   0          , 1] ;

A4 =[ A4R1 ; A4R2 ; A4R3 ; A4R4 ] ;


%Joint 5
syms theta5 d5 a5 alpha5 ;

A5R1 = [cos(theta5),  -sin(theta5),    0, a5*cos(theta5) ] ;
A5R2 = [sin(theta5),   cos(theta5),    0, a5*sin(theta5) ] ;
A5R3 = [0          ,   0          ,    1, d5             ] ;
A5R4 = [0          ,   0          ,    0, 1              ] ;

A5 =[ A5R1 ; A5R2 ; A5R3 ; A5R4 ] ;


%Final rotation about the y axis


A6 = [0 0 1 0 ; 0 1 0 0 ; -1 0 0 0 ; 0 0 0 1 ] ;

% Robot arm matrix

RTH = A1*A2*A3*A4*A5*A6 ;

RTH = simple(RTH)


%D-H kinemtic parameters for robot - angles in radians and distances
in cm

ang1rad = (angle(1)*pi)/180
ang2rad = (angle(2)*pi)/180
ang3rad = (angle(3)*pi)/180
ang4rad = (angle(4)*pi)/180
ang5rad = (angle(5)*pi)/180

%Joint 1
theta1 = ang1rad;
d1 = 15    ;
a1 = 0     ;
alpha1 = pi/2  ;

%Joint 2
theta2 = ang2rad ;
d2 = -3 ;
a2 = 10 ;
alpha2 = 0 ;
```

```
%Joint 3
theta3 = ang3rad ;
d3 = -4  ;
a3 = 5  ;
alpha3 = 0  ;

%Joint 4 pitch
theta4 = ang4rad;
d4 = 0 ;
a4 = 0 ;
alpha4 = -pi/2 ;

%Joint 5 yaw
theta5 = ang5rad ;
d5 = 0 ;
a5 = 4 ;
alpha5 =  pi/2 ;


% Determine orientation and position matix

dbsol=(eval(RTH))


% Check if solution is OK.  Check z value if below 0.2 do not run
robot

test=dbsol(3,4) ;

if test < 0.2

   fprintf('Do not run')

else

   fprintf('OK to run')
end

% Individual elements in the robot arm matrix

% Column 1
nx = RTH(1,1)
ny = RTH(2,1)
nz = RTH(3,1)
RTH41 = RTH(4,1)

% Column 2
ox = RTH(1,2)
oy = RTH(2,2)
oz = RTH(3,2)
RTH42 = RTH(4,2)


% Column 3
ax = RTH(1,3)
ay = RTH(2,3)
az = RTH(3,3)
RTH43 = RTH(4,3)
```

```
% Column 4
px = RTH(1,4)
py = RTH(2,4)
pz = RTH(3,4)
RTH44 = RTH(4,4)
```

Appendix D

Forward Kinematics Robot Arm Matrix Equations

Inputs

Joint angles: theta1, theta2, theta3 theta4, and theta5

Outputs

Torch tip position and orientation with respect to base coordinates.

Orientation: n_x n_y n_z, o_x o_y o_z, a_x a_y a_z

Position: p_x, p_y and p_z.

Orientation:

==

n_x =

-1/2*sin(-theta4-theta3+theta1-theta2)+1/2*sin(theta4+theta3+theta1+theta2)

n_y =

-1/2*cos(theta4+theta3+theta1+theta2)+1/2*cos(-theta4-theta3+theta1-theta2)

n_z =

-cos(theta2+theta3+theta4)

$^{R}T_{H}(4,1) = 0$

==

o_x =

-1/4*sin(theta5-theta4-theta3+theta1-theta2)+1/4*sin(-theta5-theta4-theta3+theta1-theta2)-1/4*sin(theta5+theta4+theta3+theta1+theta2)+1/4*sin(-theta5+theta4+theta3+theta1+theta2) -1/2*sin(theta1+theta5)-1/2*sin(theta1-theta5)

o_y =

-1/4*cos(-theta5+theta4+theta3+theta1+theta2) +1/4*cos(theta5+theta4+theta3+theta1+theta2) -1/4*cos(-theta5-theta4-theta3+theta1-theta2)+1/4*cos(theta5-theta4-theta3+theta1-theta2)+1/2*cos(theta1-theta5)+1/2*cos(theta1+theta5)

o_z =

-1/2*cos(theta2+theta3+theta4-theta5)+1/2*cos(theta2+theta3+theta4+theta5)

$^{R}T_{H}(4,2)$ = 0

==

a_x =

1/4*cos(-theta5-theta4-theta3+theta1-theta2)+1/4*cos(theta5-theta4-theta3+theta1-theta2)+1/4*cos(-theta5+theta4+theta3+theta1+theta2) +1/4*cos(theta5+theta4+theta3+theta1+theta2)-1/2*cos(theta1-theta5) +1/2*cos(theta1+theta5)

a_y

1/4*sin(theta5+theta4+theta3+theta1+theta2)+1/4*sin(-theta5 +theta4 +theta3 +theta1+theta2)+1/4*sin(theta5-theta4-theta3+theta1-theta2)+1/4*sin(-theta5-theta4-theta3+theta1-theta2)+1/2*sin(theta1+theta5)-1/2*sin(theta1-theta5)

a_z =

1/2*sin(theta2+theta3+theta4+theta5)+1/2*sin(theta2+theta3+theta4-theta5)

$^{R}T_{H}(4,3)$ = 0

==

Position:

p_x =

1/4*a5*cos(-theta5-theta4-theta3+theta1-theta2)+1/4*a5*cos(theta5-theta4-theta3+theta1-theta2)+1/4*a5*cos(-theta5+theta4+theta3+theta1+theta2)+1/4*a5*cos(theta5+theta4+theta3+theta1+theta2)-1/2*a5*cos(theta1-theta5)+1/2*a5*cos(theta1+theta5)+1/2*d5*sin(-theta4-theta3+theta1-theta2)-1/2*d5*sin(theta4+theta3+theta1+theta2)+1/2*a3*cos(-theta3+theta1-theta2)+1/2*a3*cos(theta3+theta1+theta2)+sin(theta1)*d3+1/2*a2*cos(theta1-theta2)+1/2*a2*cos(theta1+theta2)+sin(theta1)*d2

p_y =

1/4*a5*sin(theta5+theta4+theta3+theta1+theta2)+1/4*a5*sin(-theta5+theta4+theta3+theta1+theta2)+1/4*a5*sin(theta5-theta4-theta3+theta1-theta2)+1/4*a5*sin(-theta5-theta4-theta3+theta1-theta2)+1/2*a5*sin(theta1+theta5)-1/2*a5*sin(theta1-theta5)+1/2*d5*cos(theta4+theta3+theta1+theta2)-1/2*d5*cos(-theta4-theta3+theta1-theta2)+1/2*a3*sin(theta3+theta1+theta2)+1/2*a3*sin(-theta3+theta1-theta2)-cos(theta1)*d3+1/2*a2*sin(theta1+theta2)+1/2*a2*sin(theta1-theta2)-cos(theta1)*d2

p_z =

1/2*a5*sin(theta2+theta3+theta4+theta5)+1/2*a5*sin(theta2+theta3+theta4-theta5)+cos(theta2+theta3+theta4)*d5+a3*sin(theta2+theta3)+a2*sin(theta2)+d1

$^{R}T_{H}(4,4) = 1$

Appendix E

Wrist Matrix Equations

```
% Dermot Breen
% April 2009

% Wrist Matrix

%Joint 4

syms theta4 d4 a4 alpha4  ;

A4R1 = [cos(theta4),  0,  -sin(theta4), 0] ;
A4R2 = [sin(theta4),  0,   cos(theta4), 0] ;
A4R3 = [0          , -1,   0          , 0] ;
A4R4 = [0          ,  0,   0          , 1] ;

A4 =[ A4R1 ; A4R2 ; A4R3 ; A4R4 ] ;


%Joint 5

syms theta5 d5 a5 alpha5 ;

A5R1 = [cos(theta5),  -sin(theta5),    0, a5*cos(theta5) ] ;
A5R2 = [sin(theta5),   cos(theta5),    0, a5*sin(theta5) ] ;
A5R3 = [0          ,   0          ,    1, d5             ] ;
A5R4 = [0          ,   0          ,    0, 1              ] ;

A5 =[ A5R1 ; A5R2 ; A5R3 ; A5R4 ] ;


%Final rotation about the y axis


A6 = [0 0 1 0 ; 0 1 0 0 ; -1 0 0 0 ; 0 0 0 1 ] ;
A6inv = inv(A6)

RTH = A4*A5*A6 ;


%Determination of matix for home position

RTH = simple(RTH)

a5 = 5;
d5 = 0;
theta4 = 0;
theta5 = 0;
toolPos = eval(RTH)
```

Appendix F

Inverse Kinematics

```
%Dermot Breen 5 axis inverse Kinematics solution December 2007

%Homogeneous transformation matrix vector p and a inputs



% Inverse A6

A6 = [0 0 1 0 ; 0 1 0 0 ; -1 0 0 0 ; 0 0 0 1 ] ;
A6inv = inv(A6);


%Position and approach vector inputs

[dbsol] = [0 0    .4          -10   ; ...
           0 0    .3          -6    ; ...
           0 0    .866        20    ; ...
           0 0    0           1     ]  ;%


% *************************Inverse solution
*******************************

%Kinematic parameters (Lego model) and torch tip end position

a2=10;
a3=5;
a5=4;
d1 = 15;

px = dbsol(1,4);
py = dbsol(2,4);
pz = dbsol(3,4);


% Determination of wrist position

pwx = px - a5*dbsol(1,3);
pwy = py - a5*dbsol(2,3);
pwz = pz - a5*dbsol(3,3) ;                     %   change
>>>>>>>>>>>>>>>>>>>>>-d1; %scale to origin
```

```
%waist angle (theta1)
*****************************************************

% there are two solutions these equations identifies one

theta1teststart = atan2(pwy,pwx)*180/pi;

hyp = sqrt(pwx^2 + pwy^2);
adj = 7;
opp = sqrt(hyp^2 - adj^2);

theta1test(1) = theta1teststart + atan(opp/adj)*180/pi;
theta1testsol(1) = theta1test(1) - 90;
test1_x = 7*cos(theta1test(1)*pi/180);
test1_y = 7*sin(theta1test(1)*pi/180);

theta1solang = theta1testsol(1);  % waist angle solution

%
**********************************************************************
***



%Elbow angle
(theta3)******************************************************

% There is an elbow up and elbow down solution, only one is idntified
%using these equations

lenpwx=opp;
pwzS= pwz-15  ; % measured from shoulder
c3 = (lenpwx^2 + pwzS^2 - a2^2 - a3^2)/(2*a2*a3);
s3 = sqrt(1-c3^2);

theta3solang = atan2(s3,c3)*(180/pi) ;% elbow angle solution

%*********************************************************************
*****



%Shoulder angle (theta2)
**************************************************


s2 = ((a2 + a3*c3)*pwzS - (a3*s3*lenpwx))/(lenpwx^2 + pwzS^2);
c2 = ((a2 + a3*c3)*abs(lenpwx) + (a3*s3*pwzS))/(lenpwx^2+ pwzS^2);

theta2solang = atan2(s2,c2)*(180/pi) ;%shoulder angle soultion

%*********************************************************************
*****
theta1solang
theta2solang
theta3solang
```

```
% Pan tilt angles (theta4 and theta5)
*************************************

%Multiply the inverse of the solution matrix for theta1,theta2 and
theta3
%by the input arm matrix and equate with A4*A5*A6 to give the
following
%solution equations

%Generate arm matrix for first three angles

syms theta1 d1 a1 alpha1;

%Joint 1
A1R1 = [cos(theta1),  0       ,  sin(theta1) , 0 ] ;
A1R2 = [sin(theta1),  0       , -cos(theta1) , 0 ] ;
A1R3 = [0          ,  1       ,  0           , d1] ;
A1R4 = [0          ,  0       ,  0           , 1 ] ;

A1 =[ A1R1 ; A1R2 ; A1R3 ; A1R4 ] ;


%Joint 2
syms theta2 d2 a2 alpha2 ;

A2R1 = [cos(theta2), -sin(theta2),  0, a2*cos(theta2)] ;
A2R2 = [sin(theta2),  cos(theta2),  0, a2*sin(theta2)] ;
A2R3 = [0          ,  0          ,  1, d2            ] ;
A2R4 = [0          ,  0          ,  0, 1             ] ;

A2 =[ A2R1 ; A2R2 ; A2R3 ; A2R4 ] ;

%Joint 3
syms theta3 d3 a3 alpha3 ;

A3R1 = [cos(theta3), -sin(theta3),  0, a3*cos(theta3)] ;
A3R2 = [sin(theta3),  cos(theta3),  0, a3*sin(theta3)] ;
A3R3 = [0          ,  0          ,  1, d3            ] ;
A3R4 = [0          ,  0          ,  0, 1             ] ;

A3 =[ A3R1 ; A3R2 ; A3R3 ; A3R4 ] ;

% Kinematic parameters

%Joint 1
theta1 = theta1solang*pi/180;
d1 = 15    ;
a1 = 0     ;
alpha1 = pi/2  ;

%Joint 2
theta2 = theta2solang*pi/180 ;
d2 = -3 ;
a2 = 10 ;
alpha2 = 0 ;
```

```
%Joint 3
theta3 = theta3solang*pi/180 ;
d3 = -4  ;
a3 = 5  ;
alpha3 = 0  ;

%Three axis arm matrix

a1a2a3 = eval(simple(A1*A2*A3))


%Pan Tilt matrix

a1a2a3a4a5a6 = dbsol

a4a5a6 = inv(a1a2a3)*a1a2a3a4a5a6


%theta4 and theta5 solution from pan_tilt matrix

theta4solang = atan2(a4a5a6(2,3),a4a5a6(1,3))*180/pi


syms theta4 d4 a4 alpha4  ;

A4R1 = [cos(theta4),  0,  -sin(theta4), 0] ;
A4R2 = [sin(theta4),  0,   cos(theta4), 0] ;
A4R3 = [0          , -1,   0          , 0] ;
A4R4 = [0          ,  0,   0          , 1] ;

A4 =[ A4R1 ; A4R2 ; A4R3 ; A4R4 ] ;

%Joint 4
theta4 = theta4solang*pi/180 ;
d4 = 0  ;
a4 = 0  ;
alpha4 = -pi/2  ;


a1a2a3a4 = eval(simple(A1*A2*A3*A4))


a5a6 = inv(a1a2a3a4)*dbsol


theta5solang = atan2(a5a6(2,3),a5a6(1,3))*180/pi

%
***********************************************************************
***

angle =
[theta1solang,theta2solang,theta3solang,theta4solang,theta5solang]
```

```
% Output results
**********************************************************

% Generate arm matrix with solution angles
% to test if solution correct

inputmatrix = round(dbsol*100)/100         % input matrix
%ang_sol=[theta1solang,theta2solang,theta3solang,theta4solang,theta5so
lang]
final_sol =round(forwardKinematics(angle)*100)/100;


inputdata = [ inputmatrix(1,3) inputmatrix(2,3) inputmatrix(3,3)
inputmatrix(1,4) inputmatrix(2,4) inputmatrix(3,4) ]
solutionTest = [ final_sol(1,3) final_sol(2,3) final_sol(3,3)
final_sol(1,4) final_sol(2,4) final_sol(3,4)]

% Display results

display('Input data')
display(inputdata)
display('Solution angles')
fprintf('\nCalculated angles in degrees are theta1 = %g theta2 = %g
theta3 = %g theta4 = %g theta5 = %g\n\n'
,theta1solang,theta2solang,theta3solang,theta4solang,theta5solang)
display('Solution data calculated from solution angles')
display(solutionTest)
display ('Test if input matrix and solution matrix are equal 1 = true,
0 = false')
test_sol = isequal(inputdata,solutionTest)
```

Appendix G

Flame Removal

```
% Author: Dermot Breen

% Date: December 2006

% Program: Flame removal using UV lighting
%          and UV filtering


% Load image
im1 = imread('filter387BlackLightFlameOn.jpg');
im1 = rgb2gray(im1);


% Canny Edge Detection
thresh = .16  % .16
sigma = 1.5   % 1.5
BW = edge(im1,'canny',thresh,sigma);
[height width] = size(BW);


% Remove bodrder pixels
BW2 = BW(20:height-20, 20:width-20);
BW2 = imclearborder(BW2);
BW2 = ~BW2


% Show Images
figure
imshow(im1);

figure
imshow(BW)

figure
imshow(BW2);

figure
imshow(im2);
```

```
% Determine Parameters of the Letter I

figure
L = bwlabel(~BW2);
imshow(L);
[r,c] = find(L==3);
rc = [r c];
I = bwselect(L,c,r)

figure
imshow(I);
I2 = imfill(I,'holes');

figure, imshow(I2),

L2 = bwlabel(I2)

STATS = regionprops(L2,'All')
```